INFORMATION TO USERS

This manuscript has been reproduced from the microfilm master. UMI films the text directly from the original or copy submitted. Thus, some thesis and dissertation copies are in typewriter face, while others may be from any type of computer printer.

The quality of this reproduction is dependent upon the quality of the copy submitted. Broken or indistinct print, colored or poor quality illustrations and photographs, print bleedthrough, substandard margins, and improper alignment can adversely affect reproduction.

In the unlikely event that the author did not send UMI a complete manuscript and there are missing pages, these will be noted. Also, if unauthorized copyright material had to be removed, a note will indicate the deletion.

Oversize materials (e.g., maps, drawings, charts) are reproduced by sectioning the original, beginning at the upper left-hand corner and continuing from left to right in equal sections with small overlaps. Each original is also photographed in one exposure and is included in reduced form at the back of the book.

Photographs included in the original manuscript have been reproduced xerographically in this copy. Higher quality 6" x 9" black and white photographic prints are available for any photographs or illustrations appearing in this copy for an additional charge. Contact UMI directly to order.

Nuclear Stopping and Energy Removal in Central Collisions between Heavy Ions of 8–115 AMeV

A Dissertation Presented

by

Rulin Sun

to

The Graduate School

in Partial Fulfillment of the Requirements

for the Degree of

Doctor of Philosophy

in

Chemistry
(Nuclear Chemistry)

State University of New York
at
Stony Brook
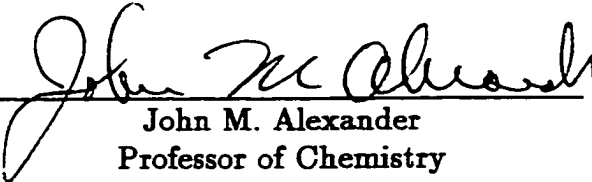
August 1999

UMI Number: 9942049

UMI

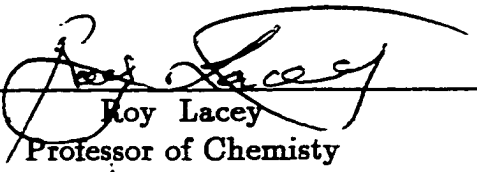300 North Zeeb Road
Ann Arbor, MI 48103

State University of New York
at Stony Brook

The Graduate School

Rulin Sun

We, the dissertation committee for the above candidate for the Doctor of
Philosophy degree, hereby recommend acceptance of the dissertation.

John M. Alexander
Professor of Chemistry

Roy Lacey
Professor of Chemisty

David Hanson
Professor of Chemisty

Thomas K. Hemmick
Professor of Physics

This dissertation is accepted by the Graduate School.

Graduate School

ii

Abstract of the Dissertation

Nuclear Stopping and Energy Removal in Central Collisions between Heavy Ions of 8–115 AMeV

by

Rulin Sun

Doctor of Philosophy

in

Chemistry

State University of New York at Stony Brook

1999

Central and mid-central collisions have been studied for ^{40}Ar + Cu, Ag and Au from 8 to 115 A MeV. Slow moving heavy residual nuclei were observed along with near 4π detection (including $\sim$0.5° to 165° in the lab.) of light charged particles and fragments. A continuous increase in the multiplicities from the most violent collisions is observed with increasing projectile energy. The heavy residual nuclei are found to accept a majority fraction of the projectile momentum only up to $\sim$ 44 A MeV, but then to yield this majority fraction to the ejectile spray for 65-115 A MeV. This con-

iii

firms a dominance of familiar incomplete fusion processes up to $\sim$ 44 A MeV, but then demonstrates a succession to splintering central collisions, a new reaction class for the Fermi energy domain.

For the central collisions, isotropic and forward-peaked components in the frame of the heaviest fragment are separated for each ejectile type. The nuclear stopping is characterized via average longitudinal momenta for the heaviest fragment and for each ejectile type. Comparison of measured values of longitudinal volecity for the heaviest fragment with predictions of the Boltzmann-Uehling-Uhlenbeck (BUU) model shows the over estimation of nuclear stopping by the model. Ejectiles emitted isotropically in the frame of the heaviest fragment define average deposition energies that reach 1-2 GeV, but there is no clear signature for a liquid-gas phase transition.

Collective tranverse flow is measured by azimuthal correlation functions between each ejectile and the reaction plane, determined by vector summation of projectile-like-fragments. The energy at which collective transverse flow in the reaction plane disappears, termed the balance energy, is found to decrease as the mass of the target increases.

The disassembly of the heaviest nuclei for these relatively high energy reactions is compared to calculations by multifragmentation models. Large divergences appear between the experimental data and calculated values. While the models predict the disappearance

iv

of heavy residual fragments, we find that the heavy residual nuclei remain for most central collisions even in reactions with 115 AMeV ^{40}Ar. The balance of the deposition energy between bond breaking and ejectile kinetic energy favors the former in the model but favors the latter for the isotropic emission ensemble.

Contents

vii

List of Figures

xi

xiii

List of Tables

Acknowledgements

Upon attaining this goal of my doctorate degree, there are so many thanks I should say to many people. I know I can't really express my gratitude, in English words, to all those who have given me their assistance. First and foremost, I would like to extend special thanks to my research advisor Professor John Alexander. To be his student is one of most fortunate events in my life. From my graduate career, I understand deeply Carl Gelderloos's words of "his unfailing sense of direction and uncanny sense of intuition in matters of research". As a foreign student, I feel more keenly about his concern for students in both academic and daily life. Also a warmest thank you from our family is extended to Betty Alexander, whose concern and hospitality could not be matched.

My most heartfelt thanks are extended toward my wife Zhihui Liu, who sacrificed a lot of her interests and time to support my research. Her assistance has been more than merely essential, and I am forever grateful.

My lovely thanks go to my daughters Penny and Dora for reminding me what really matters in life.

My sincere thanks are addressed to my fellows in the Nuclear Chemistry

research group for their professional support and friendship, specially to N.N. Ajitanand, for his endless effort and help in simulations and other calculations; to Eric Colin, for his assistance and a great contribution to the energy calibrations and in-depth discussions; to Jérôme Lauret, for his patient instruction in use of software and tools, and his friendly encouragement; to Professor Roy Lacey, for his invalueable advice and support in many ways; and Paul Chung and Christopher H. Pinkenburg for their many helps.

I wish to appreciate all those involved in the experimental runs necessary for my thesis: the collaborators at NSCL, Michigan State University and Holland College; specially to Skip Vander Molen and Professor Graham Peaslee for helpful discussions for the time calibrations, and Skip Vander Molen and Robert Pak for supplying some figures in the experimental part.

I would also like to express my deepest appreciation to my committee members Professor Roy Lacey, Professor John Alexander, Professor David Hanson and Professor Thomas Hemmick for serving on my committee and volunteering to read my thesis.

I would like to acknowledge my teaching assistantship, research assistantship and other financial support from Department of Chemistry, SUNY at Stony Brook and the U.S. Department of Energy, Division of Nuclear Physics.

I wish to acknowledge all my teachers from elementary school to Peking University who fed me nutrition of scientific knowledge, which mold me little by little as a scientist when I grew up. Although I can't remember all the names, I want to list those who played a crucial role in my education: Li Guizheng, Hu Shengman, Hou Dingbang, Zhang Tingzheng, Cheng Xianbing,

Ling Qiyi, and Chen Shufeng.

I gratefully acknowledge my colleagues at Institute of Modern Physics at Lanzhou, specially Professor Li, Wenxing who gave me great advice in both study of nuclear science and personnel life.

Lastly, I thank to all those who have given directly or indirectly help to this thesis.

Chapter 1

Introduction

Heavy ion nuclear collisions have opened a door for people to study properties of nuclear matter under extremes of temperature and pressure. Over the course of several decades of research on heavy ion nuclear reactions, many features of nuclear matter have been elucidated. Nevertheless, to obtain a fully detailed picture, great efforts are still needed. As a contribution to such a long term approach, this study uses the combination of 4π light-charged-particle measurements plus slow moving heavy fragment detection to probe the energy dissipation in central collisions of ^{40}Ar + Cu, Ag, Au with incident energies from 8 AMeV to 115 AMeV. Many aspects of these nuclear reactions are touched by this work. To help put this ever expanding field into perspective, a general classification of the reactions is given in the following section, and then a brief introduction of characteristics of reactions in the Fermi energy range is given in section two. The highlights of this work are illustrated in the last section.

1.1   Energy regimes of heavy ion reactions

Heavy ion nuclear reactions can be categorized into three energy regions each with distinctive reaction mechanisms. Reactions with incident energies less than 25 MeV/nucleon are classified as low-energy reactions, reactions with incident energies greater than 250 MeV/nucleon are classified as high-energy or relativistic reactions, and reactions with incident energies between 25 MeV/nucleon and 250 MeV/nucleon are normally designated as intermediate-energy reactions.

At lower energies, the reactions are essentially governed by the long range part of nuclear force, hence by the mean-field. The resulting phenomenology is fusion for most central collisions and binary dissipative reactions for more peripheral collisions. Little or no compression effects are expected and moderate excitation energies are reached. The dominant decay channels for central collisions proceed via the formation of a compound nuclear system. The timescale of these interactions allows for full damping of the projectile and target nucleons and the establishment of thermal equilibrium. The subsequent decay of these excited compound systems is largely independent of entrance channel [Bo94, Ba80], all memory of the incoming projectile and target motion having been lost. The emission of particles is well described by assuming a statistical process governed by the phase space available to the compound system. While deviations from a pure statistical model have been observed at low energies [La87, La88], general agreement exists between this theoretical framework and a large variety of observations.

In the high-energy range, the reactions are dominated by nucleon- nucleon interactions with a strong stopping power of nuclear matter. The reaction mechanisms are strongly influenced by geometrical overlap of the projectile and target, leading to the concepts of so-called participants and spectators. In this energy regime the hard-core potential of the strong interaction manifests itself in terms of such observables as flow, side-splash, etc. The most violent collisions produce high multiplicities of light charged particles and fragments. Hypothetically, it is possible to pump enough energy into these composite systems to create bulk instabilities [Mo92], or even to completely dissociate the nucleons from one another, vaporizing projectile and target nuclei [Ts93]. Many experimental claims have also been made for simultaneous multifragmentation [Mo92], although definitive characterization remains elusive. Microscopic models which include mean field effects have suggested significant compression and subsequent expansion of nuclear matter [Ba92, Ra93]. Experimental signatures for these phenomena, however, are elusive as well. Until many of these processes are conclusively demonstrated, the question will remain open as to what threshold excitation energies are required to achieve such exotic phenomena.

The intermediate-energy reactions are characterized by their transition properties from mean-field to nucleon-nucleon interactions and complex reaction mechanisms due to the competition bewteen these two interactions. This energy region is arguably the one in which the most can be learned about nuclear matter. The onset of such exotic modes of nuclear decay as are conjectured for the highest bombarding energies can reveal much about nuclear

matter and the parameters describing the nuclear equation of state. Thus, studies of this third regime of nuclear reactions can address a number of relevant questions. How are highly excited nuclei produced? How much energy can be pumped into the highly excited nuclei? How do they contain, distribute, and then get rid of energy? At what stage do statistical assumptions begin to break down? Is there any evidence for a liquid-gas phase transition?

1.2   General view of reactions in the Fermi energy range

In the last two decades, reactions in the intermediate-energy or Fermi energy range have been one of hottest areas of nuclear studies. Because a rich palette of phenomena are produced in these reactions, they can lead to a deep understanding of the properties of nuclear matter under extrame conditions of temperature and pressure. These phenomena can be briefly outlined as follows:

1) Reaction mechanism: breakup of projectile along with incomplete fusion. At lower energies the collision can be thought of as between projectile and target nuclei as a whole. At high energy, the projectile seems to be cut geometrically by the target nucleus. In the intermediate-energy range the projectile may be broken if the dissipated energy is higher than the binding energy of the projectile. The reaction mechanisms are strongly dependent on the impact parameter. In central collisions complete and incomplete fusion reactions are dominant. In more peripheral collisions, deep-inelastic reactions occur that form projectile-like fragments (PLF) and target-like fragements (TLF), which

retain a memory of the incoming channel[Sc84, To92].

The central collisions of reactions with incident energies of 25 MeV/nucleon to 250 MeV/nucleon can deposit substantial amounts of energy into a core nuclear system, with extremely high excitation energies close to or even larger than the total binding energy of the system [Ma96a].

2) The decay modes of hot nuclei from evaporation to vaporization: Hot nuclear species produced in the central collisions of Fermi energy reactions can experience various decay modes according to their intrinsic excitation energy E^*, angular momentum, density, deformation, etc..

At moderate excitation energy, the dominant decay modes are evaporation leading to residues or fission accompanied by pre- and post- fission light particle emission. When E^* is raised to a significant fraction of the binding energy, Intermediate Mass Fragment (IMF's) emission takes place indicating the onset of nuclear fragmentation. As E^* is increased even more, simultanous multifragmentation is expected to occur and then, with higher energy, to evolve toward vaporization.

3) Nuclear thermodynamics and phase transition. Nuclear thermodynamics is based on nuclear calorimetry (measurement of the excitation energy E^*) and nuclear thermometry (measurement of nuclear temperature T). There are many methods to estimate E^* [Ta96], including neutron multiplicity measurements, total kinetic energy loss evaluations, reconstruction of and energy balance for well-identified sources. Nuclear temperatures can be estimated by the following techniques: 1)measurement of the slopes of the kinetic energy distributions of evaporated light particles ('kinetic' temperatures). 2) ratio of

populations for discrete states of selected clusters ('excited states' temperature) [Be94]. 3)double-ratio of the populations of isotopic yields ('double ratio' temperature) [Al85]. The meansurement of the E^*-T correlation may provide a signal for a liquid-gas phase transition [Po87].

Most of the above studies are highly debated and are far from final conclusions. In this work, results are recorded for three different systems, ^{40}Ar + Cu, Ag and Au, with a broad incident energy range from 8 AMeV to 115 AMeV. These results provide much more evidence for people to use for a better understanding of hot nuclei.

1.3 Highlights of this Study

Results obtained from the 4π array at NSCL, MSU allow for a comprehensive characterization of reaction processes at incident energies of 8–115A MeV. On an event by event basis, the light-charged-particles were detected with the 4π detector array and identified by mass, charge, energy, flight direction and multiplicity. Slow moving heavy fragments were also recorded with 45 newly added Si wafers and characterized by their mass and energy. Some detailed features of the experiment are discussed in Chapter 2. A summary of how the raw data are calibrated and reduced to physics data is given in Chapter 3. An examination of mass, velocity and multiplicities of the overall products is given in chapter 4, and a new reaction mechanism is classified for the central collisions. The momentum and energy balance in the moving frame are given in chapter 5; these investigations lead to a better understanding of

nuclear stopping powers. In chapter 6, directed transverse flow is studied and balance energies for different reaction systems are sought from tranverse momentum analysis. In chapter 7, comparisons with multifragmentation models are given to show the divergence of experimental data and simulations for the disassembly of hot nuclei. An overall summary is given in chapter 8 along with the conclusions. The analyses described in this dissertation comprise part of an ongoing effort to understand reaction mechanisms at excitation energies approaching the binding energy. It is hoped that they will contribute to the elucidation of some of the nuclear reaction characteristics which have proved to be most intractable.

Chapter 2

Description of Experimental Setup

2.1 Overview

The Michigan State University (MSU) Cyclotron delivered ^{40}Ar beams from 8 to 115 A MeV, i.e. energies that range from the region typical of fusion to that identified with multifragmentation. The MSU 4π array provided both a multiplicity filter and an overview of angles, energies and identities of charged particles and fragments[We85]. In this experiment, a set of 45 Si detectors was mounted in front of each phoswich telescope in the high-rate array (HRA)[We85, Pa96]. The energy and time of flight (TOF) signals, recorded from each Si wafer, were analyzed to give masses for the slow moving heavy fragments.

2.2 Beams and Targets

The beams used in this experiment were provided by the K1200 cyclotron at the National Superconducting Cyclotron Laboratory (NSCL), MSU. ^{40}Ar

in the +9 charge state was tuned to yield beams with energies of 8, 17, 27, 44, 65, 90 and 115 MeV/nucleon. Targets of Cu (0.611 mg/cm^2), Ag (0.260 mg/cm^2) and Au (0.400 mg/cm^2) were bomdarded with those beams. In addition, beams of Kr with energy of 70 MeV/nucleon were applied to bombard three targets of Cu, Nb (0.800 mg/cm^2) and Au. The beam intensities were approximately 100 electrical pA.

All the targets were held with a carousel which can put a single target into the center of the ball and easily rotate to another target for the next run. With different projectile, target and energy combinations, about 140 runs in total, including some calibration runs, were recorded during three weeks.

2.3 Detectors

2.3.1 Main Ball

The main ball of the MSU 4π Array is a 32 faced truncated icosahedron, as shown in Figure 2.1, of which twenty faces are hexagons and twelve are pentagons. One of the pentagonal faces serves as the beam entrance, another connects to forward detector arrays; all the remaining sites are filled by detector modules. Each hexaganal (pentagonal) module contains a subarray of six (five) close-packed fast/slow plastic detectors resulting in a total of 170 phoswiches[Wi52]. Each phoswich consists of a thin wafer of $3mm$ fast (ΔE) plastic scintillator, followed by a $25cm$ thick block of slow (E) plastic scintillator. The rise time for fast and slow elements are $\sim 1ns$ and $20ns$, repectively, and the decay times are $\sim 3.3ns$ and $180ns$.
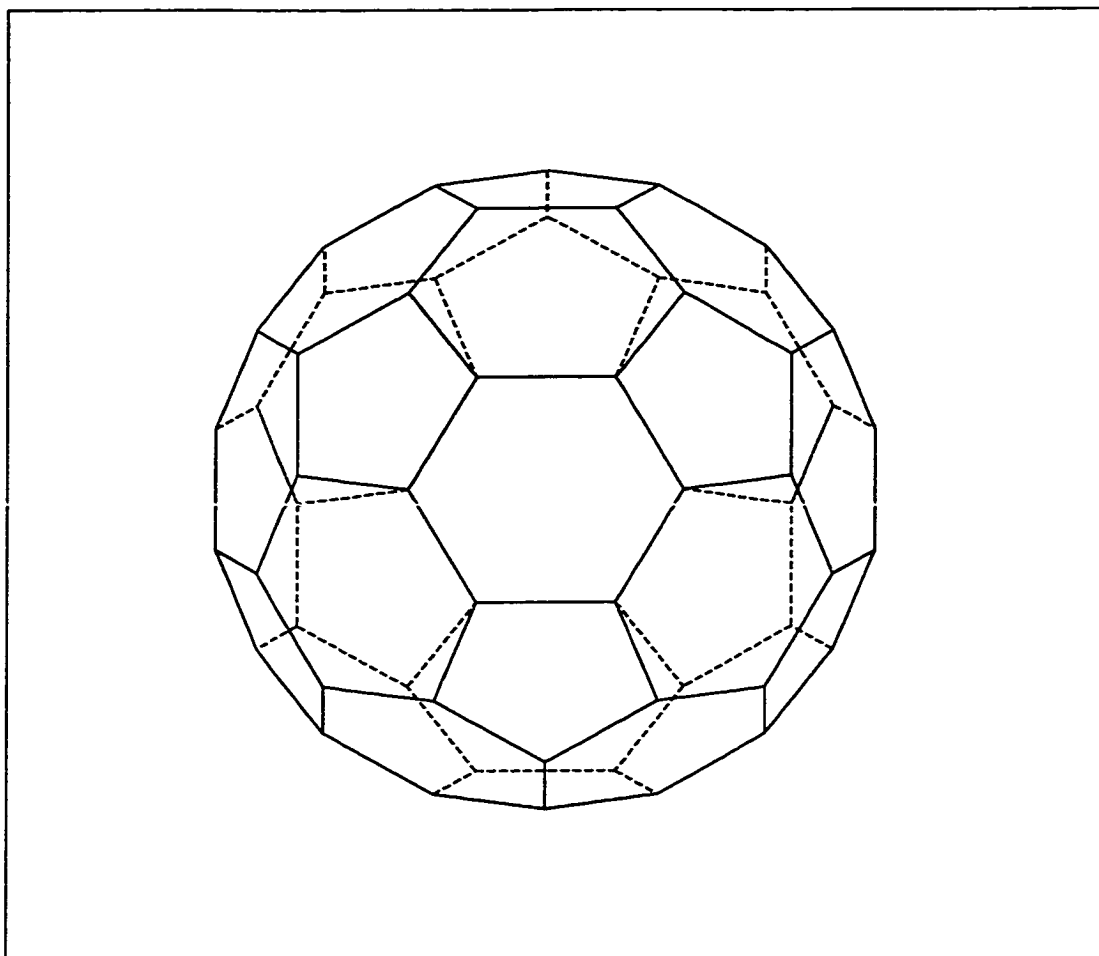
Figure 2.1: Basic geometry of the main ball of the MSU 4π Array

SUBARRAY OF MULTIPARTICLE ARRAY

FAST/SLOW PLASTIC SCINTILLATORS

LOW PRESSURE
MWPC

BRAGG CURVE
SPECTROMETER
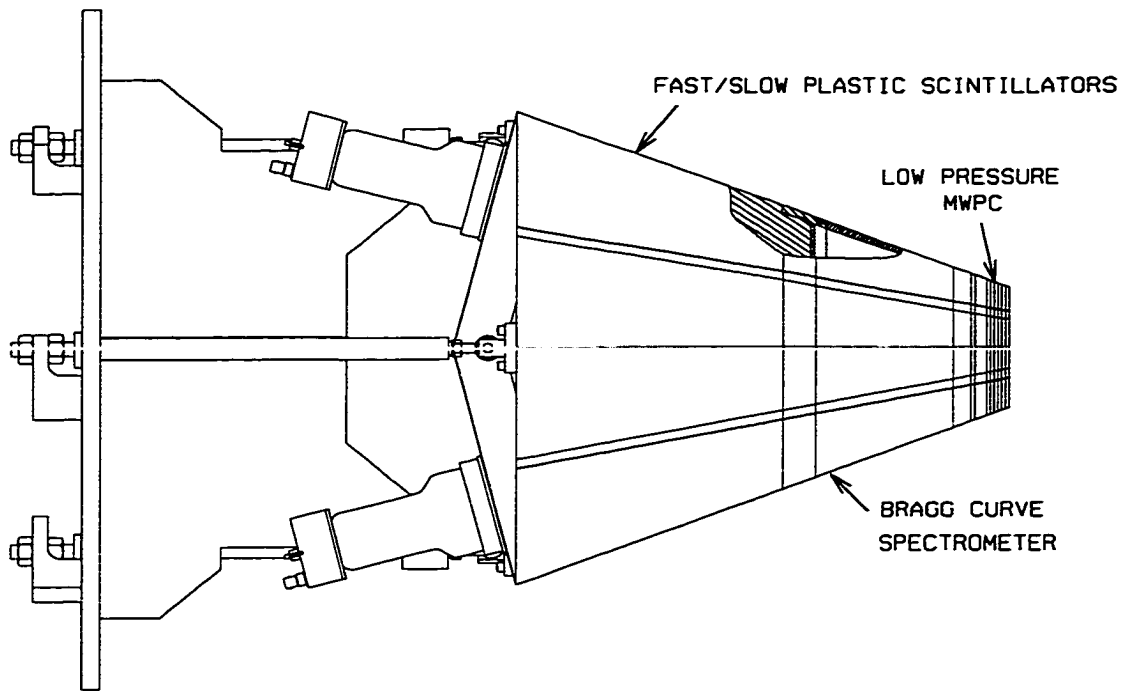
Figure 2.2: Schematic diagram of the components of an hexagonal MSU 4π module.

Mounted in front of each phoswich subarray is a gas ionization chamber known as a Bragg Curve Counter (BCC)[Gr82]. The hexagonal anodes of the five most forward BCCs are segmented, resulting in total of 55 separate detectors of this type. Figure 2.2 shows the components of an MSU hexgonal module. A schematic view of a 4π BCC module is shown in Figure 2.3. The overall length of such a counter is $15cm$ and the entrance window for a hexagon module is $10cm$ across from side to side. Because of the large dimensions, it is important to include radial field shaping strips on the inside surfaces of the walls. The walls are made from $6.4mm$ thick G10 fiberglassepoxy laminate. The pressure window is a $900\mu g/cm^2$ Kapton foil. The separation (or drift space) between cathode and Frisch grid is $14cm$. The Frisch grid is made from $12.5\mu m$ gold-plated tungsten wires with $0.5mm$ spacing. In this experiment, the BCC's were operated in the ion chamber mode with a pressure of 125 Torr of C_2F_6 gas. The BCC's were used to measure the energy loss of charged particles that stopped in the fast plastic scintillator of the main ball; their use gives significantly lower kinetic energy thresholds.

The detectors of the main ball cover laboratory polar angles of $18° < \theta_{lab} < 162°$. The mean angular position of each ball detector is listed in Table 2.1. The individual phoswich detectors in the main ball are truncated triangular pyramids which subdivide either hexagons ($60°, 60°, 60°$) or pentagons ($72°, 54°, 54°$). The solid angle subtended by each ball phoswich is listed in Table 2.2 The true solid angles are slightly smaller than those calculated from ideal geometry due to dead spaces bewteen the modules. The energy thresholds of various particle types to be identified are listed in Table 2.3. Since a BCC

Bragg Curve Counter

Exit Anode

Cathode

Frisch Grid
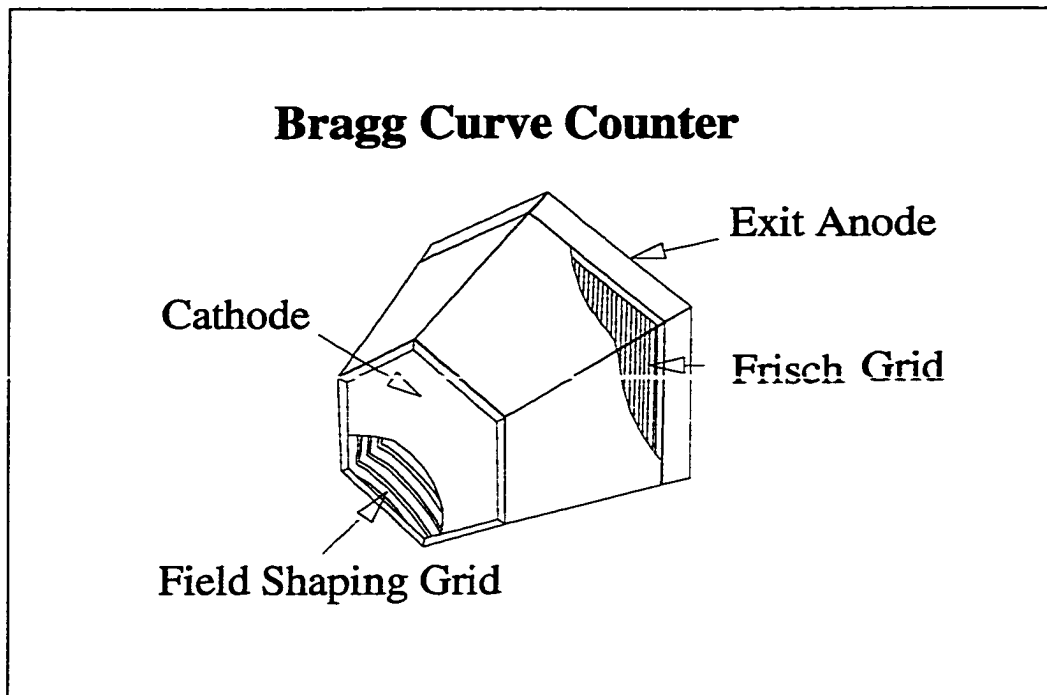
Field Shaping Grid

Figure 2.3: Schematic drawing of a Bragg Curve Counter. Cutaways show the Frisch grid and field shaping grid.

cannot give a significant signal for a particle of $Z = 1$, it must stop in the slow member of the phoswich to be identified. This leads to a rather high energy threshold for $Z = 1$ particles. For other particles, the energy thresholds are the punch-in energies for just entering the fast plastic of a phoswich in the main ball.

Module	A		B		C		D		E		F	
	θ	ϕ	θ	ϕ	θ	ϕ	θ	ϕ	θ	ϕ	θ	ϕ
1	23.1	342.0	32.3	5.6	46.0	359.3	51.7	342.0	46.0	324.7	32.3	318.4
2	23.1	270.0	32.3	293.6	46.0	287.3	51.7	270.0	46.0	252.7	32.3	246.4
3	23.1	198.0	32.3	221.6	46.0	215.3	51.7	198.0	46.0	180.7	32.3	174.4
4	23.1	126.0	32.3	149.6	46.0	143.3	51.7	126.0	46.0	108.7	32.3	102.4
5	23.1	54.0	32.3	77.6	46.0	71.3	51.7	54.0	46.0	36.7	32.3	30.4
6	54.7	298.0	54.7	314.0	67.3	317.5	74.6	306.0	67.3	294.5		
7	54.7	226.0	54.7	242.0	67.3	245.4	74.6	234.0	67.3	222.5		
8	54.7	154.0	54.7	170.0	67.3	173.5	74.6	162.0	67.3	150.5		
9	54.7	82.0	54.7	98.0	67.3	101.5	74.6	90.0	67.3	78.5		
10	54.7	10.0	54.7	26.0	67.3	29.5	74.6	18.0	67.3	6.5		
11	64.9	342.0	72.4	355.0	86.5	354.4	93.5	342.0	86.5	329.6	72.4	329.0
12	64.9	270.0	72.4	283.0	86.5	282.4	93.5	270.0	86.5	257.6	72.4	257.0
13	64.9	198.0	72.4	211.0	86.5	210.4	93.5	198.0	86.5	185.6	72.4	185.0
14	64.9	126.0	72.4	139.0	86.5	138.4	93.5	126.0	86.5	113.6	72.4	113.0
15	64.9	54.0	72.4	67.0	86.5	66.4	93.5	54.0	86.5	41.6	72.4	41.0
16	86.5	306.0	93.5	318.4	107.6	319.0	115.1	306.0	107.6	293.0	93.5	293.6
17	86.5	234.0	93.5	246.4	107.6	247.0	115.1	234.0	107.6	221.0	93.5	221.6
18	86.5	162.0	93.5	174.4	107.6	175.0	115.1	162.0	107.6	149.0	93.5	149.6
19	86.5	90.0	93.5	102.4	107.6	103.0	115.1	90.0	107.6	77.0	93.5	77.6
20	86.5	18.0	93.5	30.4	107.6	31.0	115.1	18.0	107.6	5.0	93.5	5.6
21	105.4	342.0	112.7	353.5	125.3	350.0	125.3	334.0	112.7	294.5		
22	105.4	270.0	112.7	281.5	125.3	278.0	125.3	262.0	112.7	222.5		
23	105.4	198.0	112.7	209.5	125.3	206.0	125.3	190.0	112.7	150.5		
24	105.4	126.0	112.7	137.5	125.3	134.0	125.3	118.0	112.7	78.5		
25	105.4	54.0	112.7	65.5	125.3	62.0	125.3	46.0	112.7	6.5		
26	128.3	306.0	134.0	323.3	147.7	329.6	156.9	306.0	147.7	282.4	134.0	288.7
27	128.3	234.0	134.0	251.3	147.7	257.6	156.9	234.0	147.7	210.4	134.0	216.7
28	128.3	162.0	134.0	179.3	147.7	185.6	156.9	162.0	147.7	138.4	134.0	144.7
29	128.3	90.0	134.0	107.3	147.7	113.6	156.9	90.0	147.7	66.4	134.0	72.7
30	128.3	18.0	134.0	35.3	147.7	41.6	156.9	18.0	147.7	354.4	134.0	0.7

Table 2.1: Mean angles for ball phoswiches.

MOdule Type	Ideal (msr)	True (msr)
Hexagon	(6×) 75.2	66.0
Pentagon	(5×) 59.0	49.9

Table 2.2: Solid angle subtended by the ball phoswiches.

Particle Type	Punch-in Energy (MeV)	Particle Type	Punch-in Energy (MeV)	Particle Type	Punch-in Energy (MeV)
p	17	B	46	Na	146
d	24	C	59	Mg	163
t	28	N	74	Al	184
He	12	O	91	Si	202
Li	23	F	108	P	224
Be	34	Ne	123	S	242

Table 2.3: Energy Thresholds for the Ball Phoswiches.

2.3.2 Forward Arrays

Three forward-angle detection devices were used for this experiment, their properties are described in the following subsections.

(a) The zero degree detector (ZDD) is a ring of 8 phoswich telescopes covering polar angles of $\sim 0.5^\circ$ to 1.5°[St96]. The ZDD consists of two layers of fast scintillating plastic, which was chosen for its fast decay time ($1.8ns$) and high light output (14% more light than that used for the ball phoswiches). The first (ΔE) layer of detector is $0.67mm$ thick, allowing transmission of particles with $Z \leq 18$ for $KE/A \geq 21$ MeV. The second (E) layer is $30cm$ thick, stopping all particles with $KE/A < 220$ MeV. The detector is divided into 8 azimuthally symmetric segments, which is necessary to avoid multiple hits. Figure 2.4 gives a schematic view of the ZDD.

(b) The Maryland forward array (MFA) is a second ring of 16 phoswich telescopes from $\sim 1.5^\circ$ to 3°[Ru98]. It is designed for the study of peripheral intermediate-energy heavy-ion collisions. Its low angle coverage provides for the detection of relatively heavy projectile-like fragments normally missed by the rest of the 4π array. MFA consists of a plastic phoswich array. The plastic phoswich is made of a $1mm$ thick fast plastic scintillator glued to a $10cm$ thick slow plastic scintillator. The 16 phoswich detectors are arranged in a cone-like geometry. A schematic view of MFA as it attaches to the frame of the High Rate Array is shown in Figure 2.5.

(c) A set of 45 Si detectors was mounted in front of the 45 phoswich telescopes ($\sim 3^\circ$ to 20°) of the High Rate Array (HRA)[We85, Pa96]. The
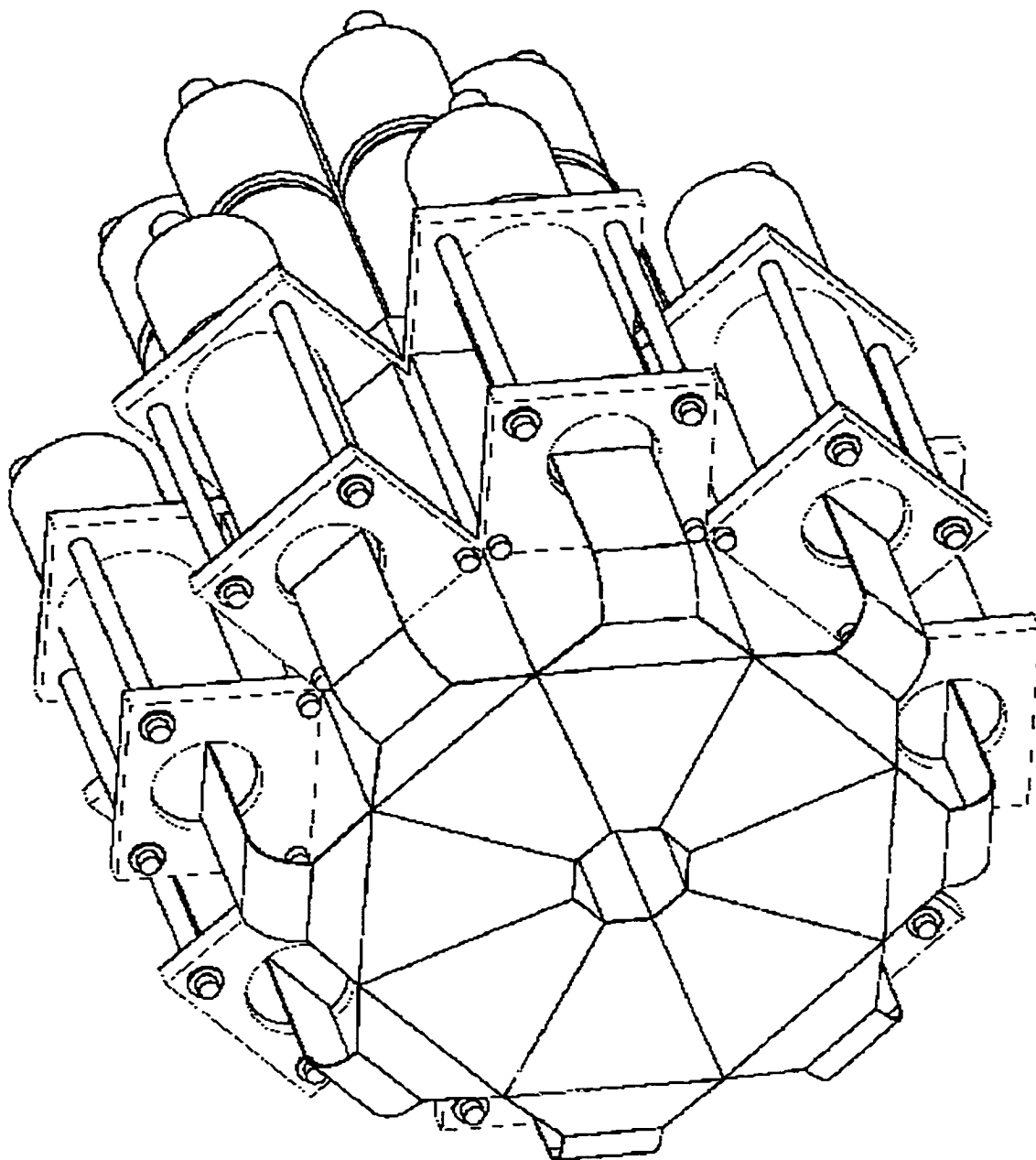
Figure 2.4: A picture of Zero Degree Detector (ZDD).
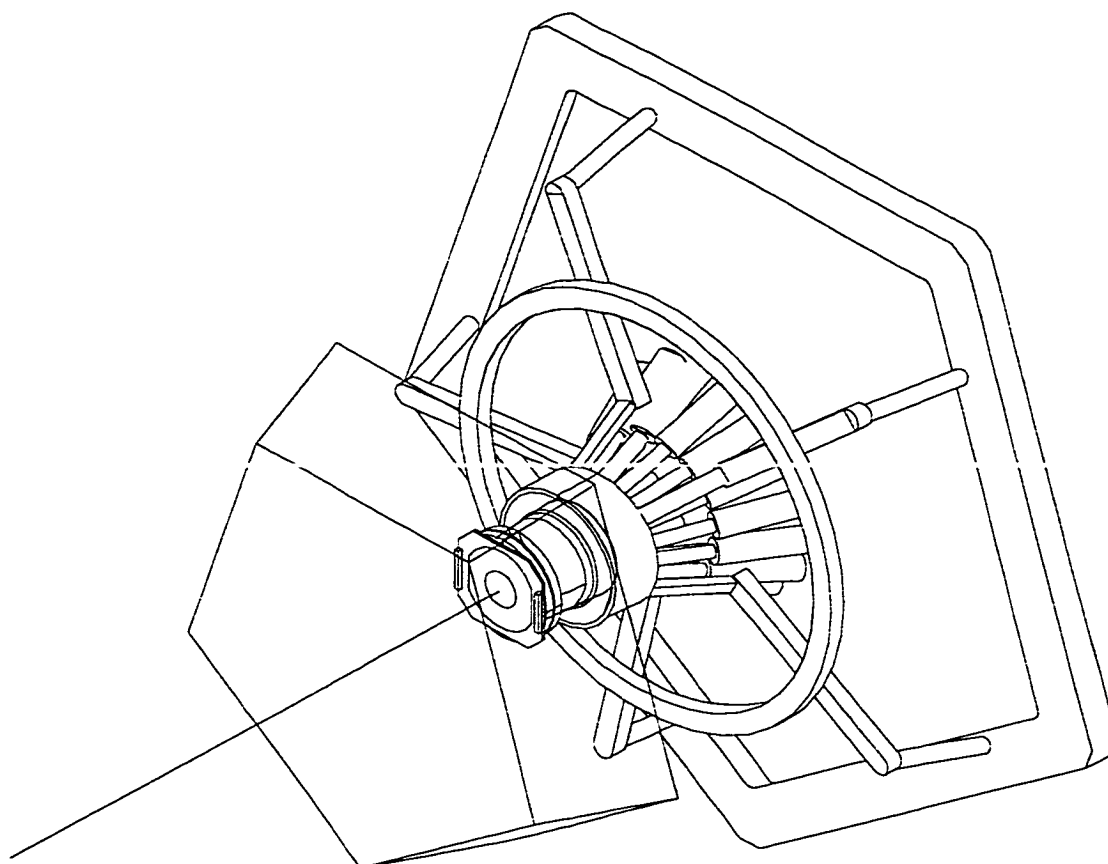
Figure 2.5: Schematic view of the Maryland Forward Array (MFA) as it attaches to the frame of the High Rate Array.

HRA is constructed of five wedges which are subdivided into nine phoswich detectors. A Schematic view of the NSCL HRA is shown in Figure 2.6. Similar to the other phoswiches, the HRA phoswiches consist of a fast (ΔE) and slow (E) plastic scintillator with thicknesses of 1.7mm and 19.4cm. Their decay times are 3.3ns and 320ns respectively.
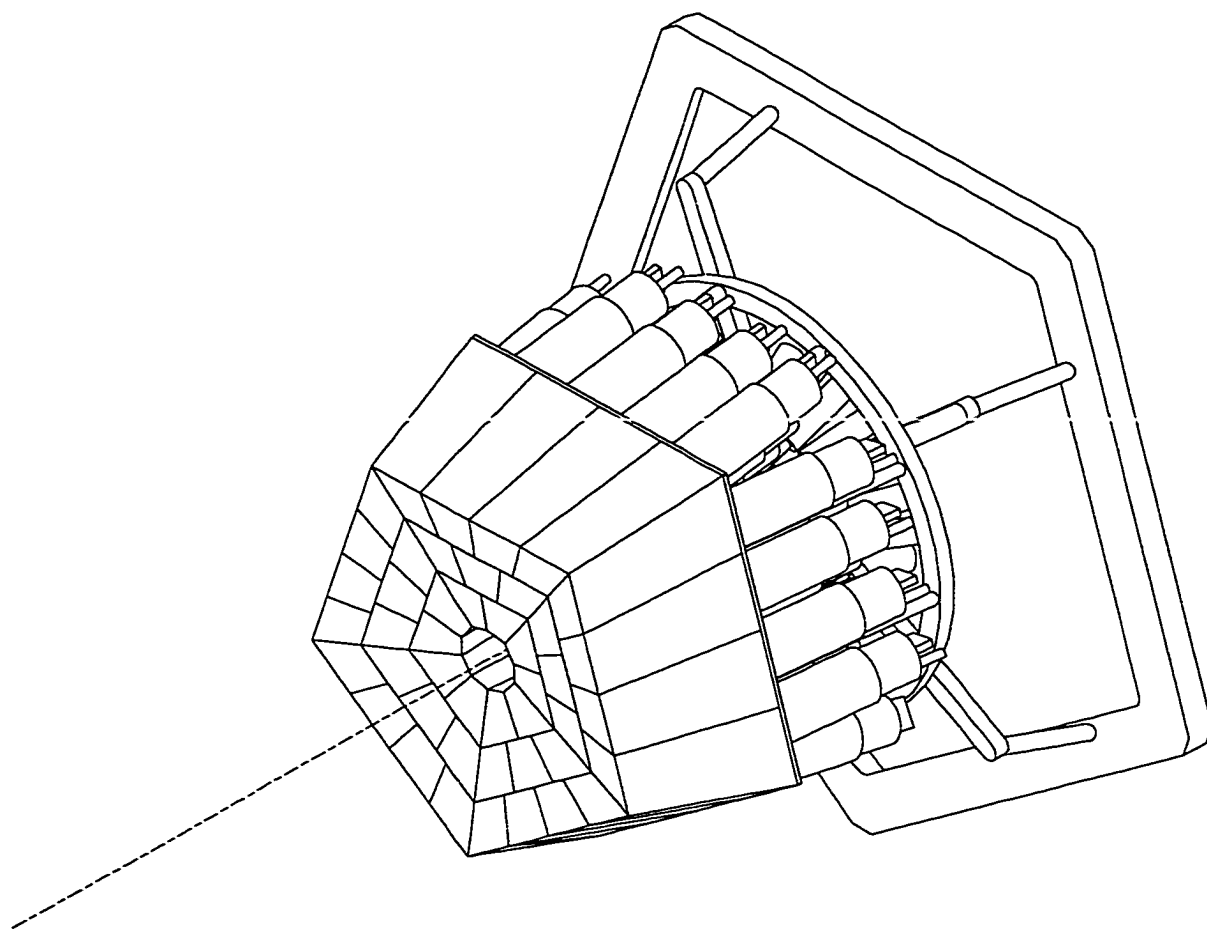
Figure 2.6: Schematic view of the NSCL High Rate Array (HRA).

The Si detectors, added by the Hope College-Stony Brook team, can be used to measure energies and velocities (hence masses) for a broad sample

of the slow moving heavy residual nuclei. The area of each Si detector is $\sim 3cm \times 3cm$ with a thickness of $\sim 140\mu m$. Figure 2.7 gives a front face view of how the Si detectors were mounted on the HRA. The support materials were $1mm$ thick aluminum foil which can block most of particles except high energy protons. Therefore the effective solid angle of the HRA was reduced to about one third. Nevertheless, the energy thresholds of the HRA detectors were decreased, since each Si detector can be used to measure the energy loss of a charged particle that stopped in the fast plastic scintillator of the HRA.
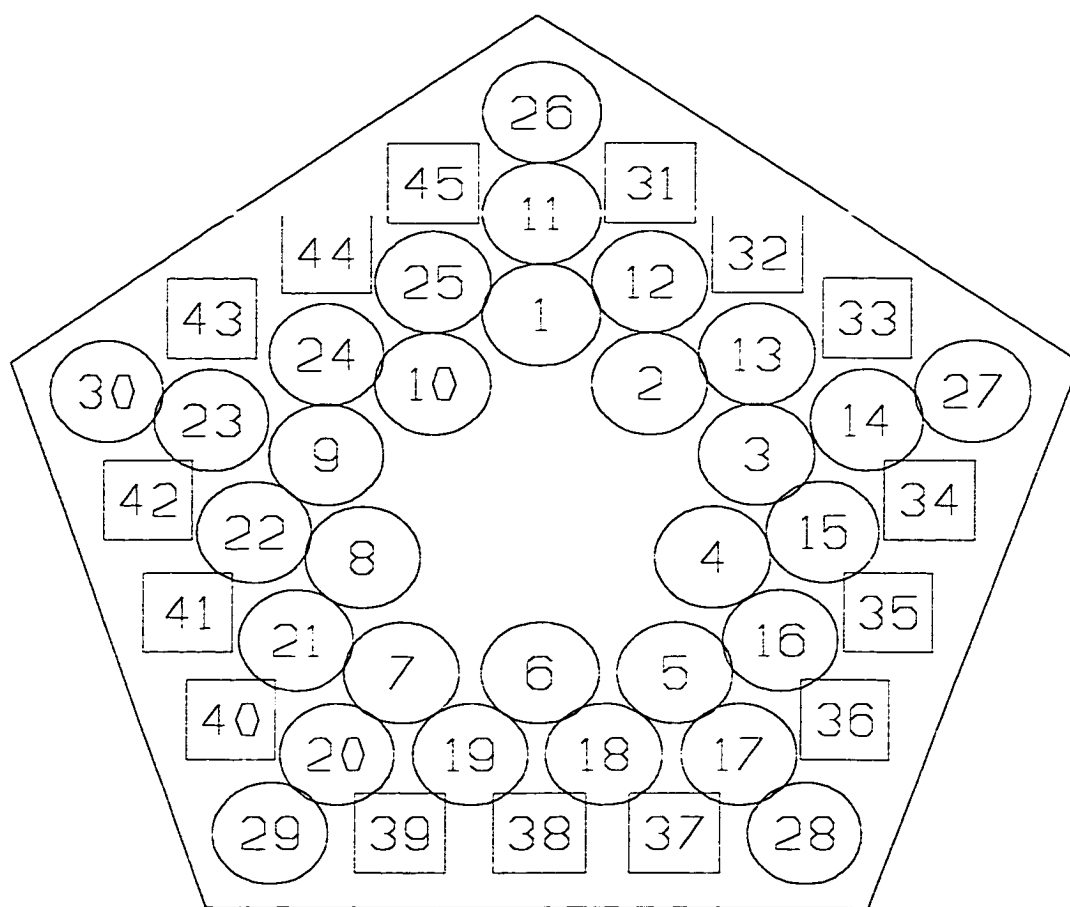
Figure 2.7: Schematic face view of Silicon detectors.

The mean angular positions and solid angles of these forward detectors are summarized in Table 2.4. Energy thresholds for different charged particles are listed in Table 2.5.

2.4 Electronics

Figure 2.8 gives an electronics diagram for one of the phoswich detectors. Each detector receives its high voltage and transmits its signal over a single SHV cable. 215 such cables run from their respective feed-throughs on the vacuum chamber, along the cable trays, and to the electronics racks. The cables plug into the back of the 15 splitter box modules where the phoswich signal is passively separated from high voltage into its fast, slow, and timing signals. There are twelve banks of signals for the main ball, three banks for the HRA, one bank for the MFA, and another for ZDD.

The ΔE and E signals from plastic scintillators are directly connected to the Fast Encoding Readout ADC (FERA). The time signals are sent to discriminators. One of the ECL output signals from discriminators is used for a TOF signal, i.e. input to the Time-to-FERA converter (FERETs) which supply time signals compatible with a FERA ADC. Additionally, the SUM output from discriminators is fed to a SUMMER and used for multiplicity discrimination. The detector position information is registered through the Virtual Station Number (8 bits) appearing in the data stream in the FERA header word.

The 45 newly added Si detectors are grouped into three banks that have

Detector	θ	ϕ	msr	Detector	θ	ϕ	msr
HRA1	5.43	0.00	3.610	HRA26	15.90	9.00	3.217
HRA2	5.43	324.00	3.672	HRA29	15.90	315.00	3.217
HRA3	5.43	288.00	3.610	HRA30	15.90	297.00	3.217
HRA4	5.43	252.00	3.672	HRA33	15.90	243.00	2.789
HRA5	5.43	216.00	3.610	HRA34	15.90	225.00	2.789
HRA6	5.43	180.00	3.672	HRA37	15.90	171.00	2.789
HRA7	5.43	144.00	3.610	HRA38	15.90	153.00	2.832
HRA8	5.43	108.00	3.672	HRA41	15.90	99.00	2.832
HRA9	5.43	72.00	3.610	HRA42	15.90	81.00	2.789
HRA10	5.43	36.00	3.672	HRA45	15.90	27.00	2.789
HRA12	9.59	342.00	3.550	MFA1	2.20	162.00	0.380
HRA15	9.59	270.00	3.550	MFA2	2.20	184.50	0.380
HRA18	9.59	198.00	3.550	MFA3	2.20	207.00	0.380
HRA21	9.59	126.00	3.550	MFA4	2.20	229.50	0.380
HRA24	9.59	54.00	3.550	MFA5	2.20	252.00	0.380
HRA11	10.64	6.00	3.434	MFA6	2.20	274.50	0.380
HRA13	10.64	318.00	3.550	MFA7	2.20	297.00	0.380
HRA14	10.64	294.00	3.434	MFA8	2.20	319.50	0.380
HRA16	10.64	246.00	3.550	MFA9	2.20	342.00	0.380
HRA17	10.64	222.00	3.434	MFA10	2.20	4.50	0.380
HRA19	10.64	174.00	3.550	MFA11	2.20	27.00	0.380
HRA20	10.64	150.00	3.434	MFA12	2.20	49.50	0.380
HRA22	10.64	102.00	3.550	MFA13	2.20	72.00	0.380
HRA23	10.64	78.00	3.434	MFA14	2.20	94.50	0.380
HRA25	10.64	30.00	3.550	MFA15	2.20	117.00	0.380
HRA27	14.26	351.00	3.217	MFA16	2.20	139.50	0.380
HRA28	14.26	333.00	3.217	ZDD1	1.10	338.30	0.240
HRA31	14.26	279.00	2.789	ZDD2	1.10	293.30	0.240
HRA32	14.26	261.00	2.832	ZDD3	1.10	248.30	0.240
HRA35	14.26	207.00	2.832	ZDD4	1.10	203.30	0.240
HRA36	14.26	189.00	2.789	ZDD5	1.10	158.30	0.240
HRA39	14.26	135.00	2.789	ZDD6	1.10	113.30	0.240
HRA40	14.26	117.00	2.789	ZDD7	1.10	68.30	0.240
HRA43	14.26	63.00	2.789	ZDD8	1.10	23.30	0.240
HRA44	14.26	45.00	2.832				

Table 2.4: Summay of the geometrical properties of forward arrays.

Particle Type	Punch-in Energy (MeV)			Particle Type	Punch-in Energy (MeV)		
	HRA	MFA	ZDD		HRA	MFA	ZDD
p	13	10	8	F	515	381	304
d	17	12	15	Ne	591	438	347
t	20	15	22	Na	687	505	396
He	50	37	30	Mg	767	563	440
Li	99	74	60	Al	877	642	504
Be	152	113	90	Si	962	704	555
B	212	157	119	P	1079	790	625
C	269	200	158	S	1170	859	685
N	341	253	201	Cl	1294	954	756
O	419	311	248	Ar	1455	1075	845

Table 2.5: Summay of energy thresholds for the Forward Arrays.

BALL(FA) Electronics
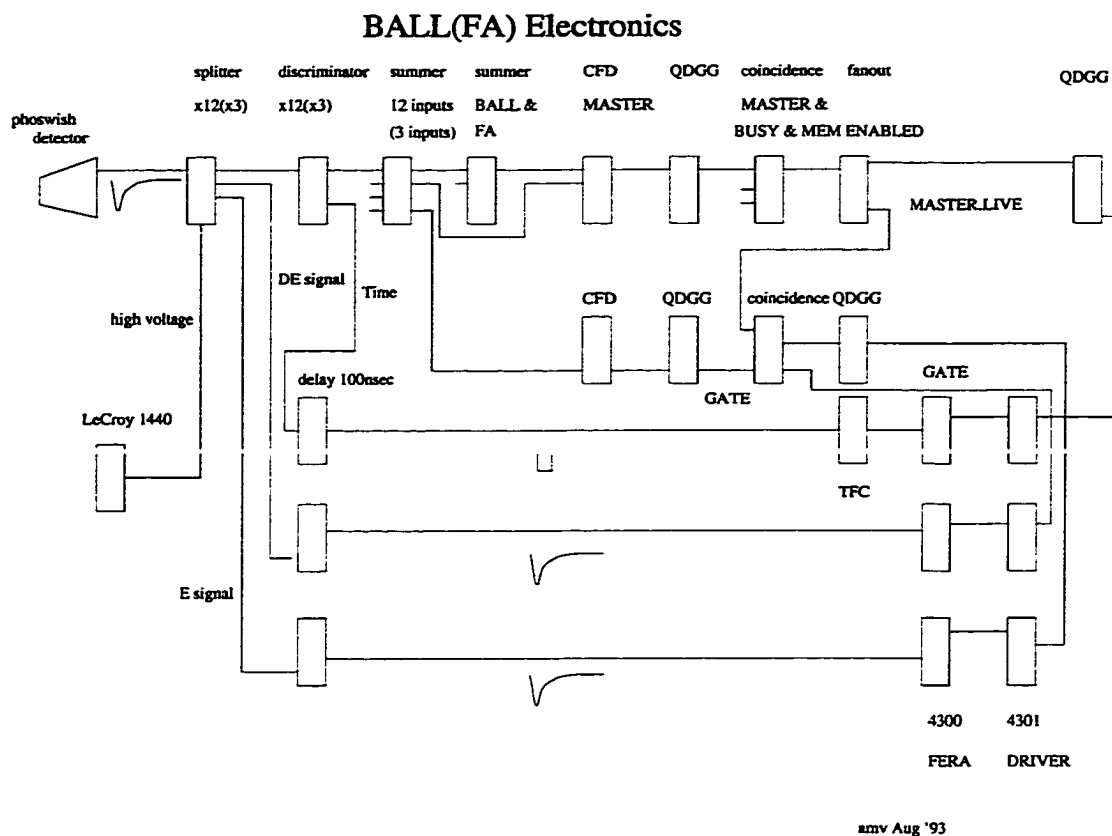
Figure 2.8: A schematic diagram of the electronics layout for the MSU 4π Array.
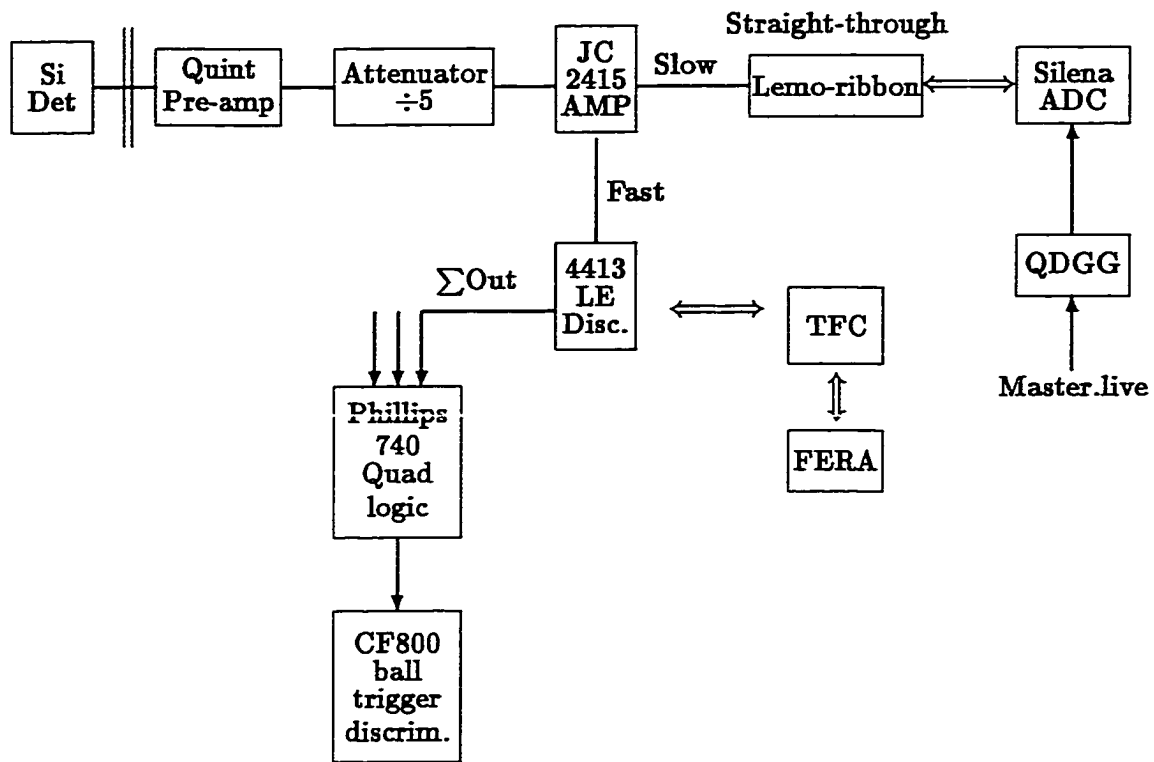
Figure 2.9: A schematic diagram of the electronics layout for the Si Detectors.

different electronics structure. Figure 2.9 shows an electronics diagram for a Si detector and how it is connected with the electronics system of the main ball. After Pre-amp, Attenuator and JC2415 Amplifier, the signal from a Si detector is divided into two components, slow and fast. The slow signals are fed directly to Silenas (commerical peak sensing ADC) to measure the energy. The fast signals are fed to discriminators. One of the output signals from a discriminator is for a TOF signal similiar to the ball TOF signals. The SUM output from these discriminators is connected to the ball discriminators.

An event is initiated by a Master.Live signal based on a specified trigger. The sum signals from discriminators of the main ball, HRA, and MFA are passed into a constant fraction discriminator (CFD) which can be programmed to select a given multiplicity for any of the four inputs (Ball, HRA, MFA or total system). The output of this octal CFD becomes the master trigger. An HRA or MFA mutiplicity trigger will enrich the data sample with peripheral events due to the forward focusing of particles in fixed target experiments, while a main ball trigger will select more central events in which particles are emitted at larger polar angles. In our experiments, we generally chose to select by the condition of two hits in the ball.

2.5 Data Acquisition

2.5.1 Hardware for Data Acquisition

The hardware for the data acquisition system consists of a host system; a UNIX based SUN clone linked to a VME transputer board. Figure 2.10

shows a diagram of the FrontEnd of the data acquisition system. The links
are transputer links to ethernet. The transputer code is downloaded from the
host and all communications are transacted over these links to/from the host
resident program called ISERVER. Data are transfered back to the host-based
memory. This data set is received by the program TRANSRC, then a routing
program (ROUTER) is started to send buffers to one or more consumers such
as TAPE. This system can handle data rates that excede 300 kilobytes/sec.
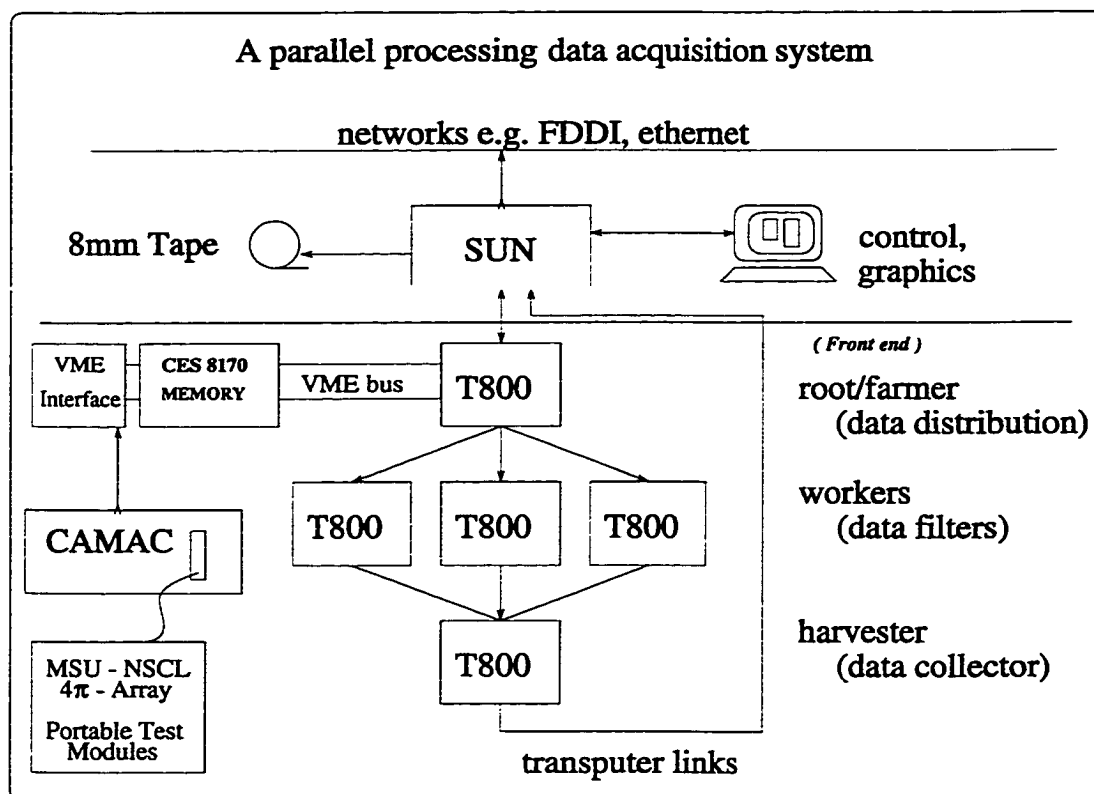
Figure 2.10: The FrontEnd of Data Acquisition system.

2.5.2 Data Buffer Structure

The structure of the data buffer can be described in the following levels.

Buffer Header

At the beginning of the buffer is a 16-word header in the following usage.

WORD   USAGE

1   Length of buffer

2   Buffer type (1 = Physics data)

4   Run

5   Buffer sequence number within a run

7   Number of events

Others   Not defined

Event Structure

Within every buffer there is an additional 16 word FFM header used for error checking. The buffer contains many events which are separated by a unique word: FFFF in hexadecimal. The FERA (and Silena) headers and data follow thereafter until the next event separator. The FERA header contains the information needed to decode the data from that FERA. The event structure may be pictured as shown in Figure 2.11.

EVENT WORD COUNT or FFM SEPARATOR
1st FERA Header
Data word 1
...
Data word n
2nd FERA Header
Data word 1
...
Data word n
...
Last FERA Header
Data word 1
...
Data word n
NEXT EVENT WC or FFM SEPARATOR
1st FERA Header
Data word 1
...
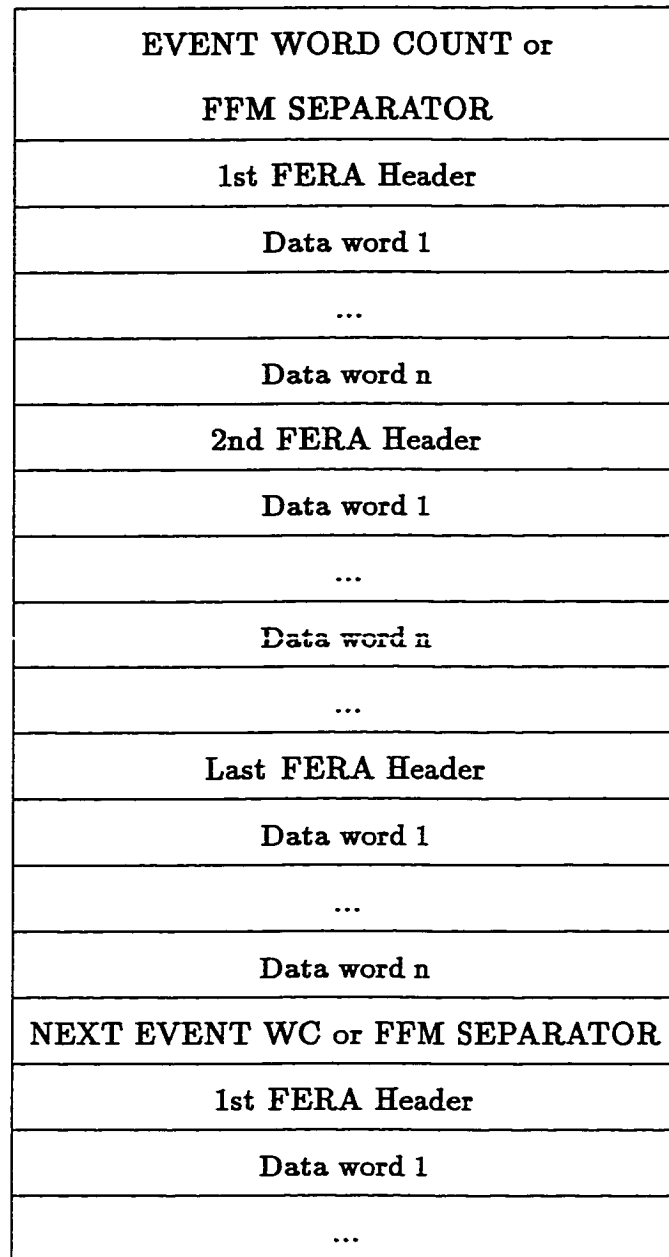
Figure 2.11: The event structure of a data buffer.

Chapter 3

Calibrations and Data Reduction

3.1 Introduction

To convert a raw data tape into a reduced physics tape with physical parameters, an important and time consuming "matching" procedure must be accomplished. This provides for the gain matching of the individual detector responses to a calibrated particle identification template[Ce92]. Two dimensional gain matching is required to get the gate lines and the response function for each individual detector. A newly developed routine MTK (see: http://nucwww.chem.sunysb.edu/dali/mtk.html) makes this process convenient and minimizes the amount of time for calibrating the large number of detectors in the MSU 4π Array. A similar procedure, described in section three, was followed to obtain gain matching for the forward array and the main ball detectors, including $\Delta E - E$ and the $BCC - \Delta E$ telescopes.

Calibrations for the 45 newly added Si detectors have been done separately. The procedure includes the energy calibration, TOF calibration and the

$Si - HRA \, \Delta E$ 2D matching to a particle identification template. The calibration parameters for all Si detectors and other detector arrays were assembled in tables as input for the program to create physics tapes.

3.2 Calibration of the Silicon Detectors

3.2.1 Energy Calibration

For Si detectors, the relationship of pulse height to energy loss for different particles has the same linear form. In principle, one can use a Th-C source with two α decay energies (6.09,9.08MeV) to do the energy calibration of the Si detectors. Since these energies are very close compared to those for the fragments emitted from our heavy ion reactions, large errors could be introduced. Instead, we also use the set of punch-through channels for different particles or fragments found from 2D displays of HRA ΔE-Si [Co98] as shown in Figure 3.1. The corresponding energy can be calculated [Ke92] since we know the thickness of Si detectors. Thus we obtain more points in the higher energy region; and a calibration curve is plotted as energy vs channel number as shown in Figure 3.2.

3.2.2 Time Calibration

The TOF calibration requires a process to find the parameters for determining the time-of-flight (TOF) of slow moving heavy fragments detected in the Silicon detectors. In our experiment, the absolute TOF of a particle (
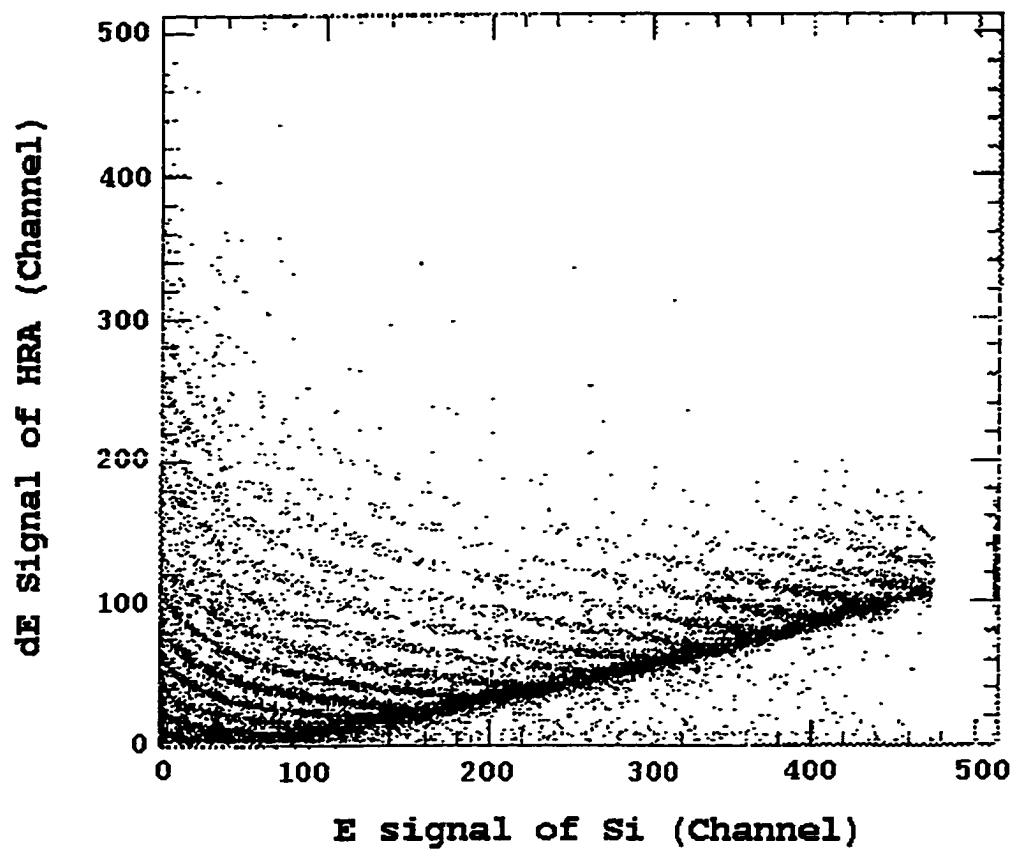
Figure 3.1: 2D energy spectrum (in channel) of HRA fast-Si to find the punch through channel of different particles
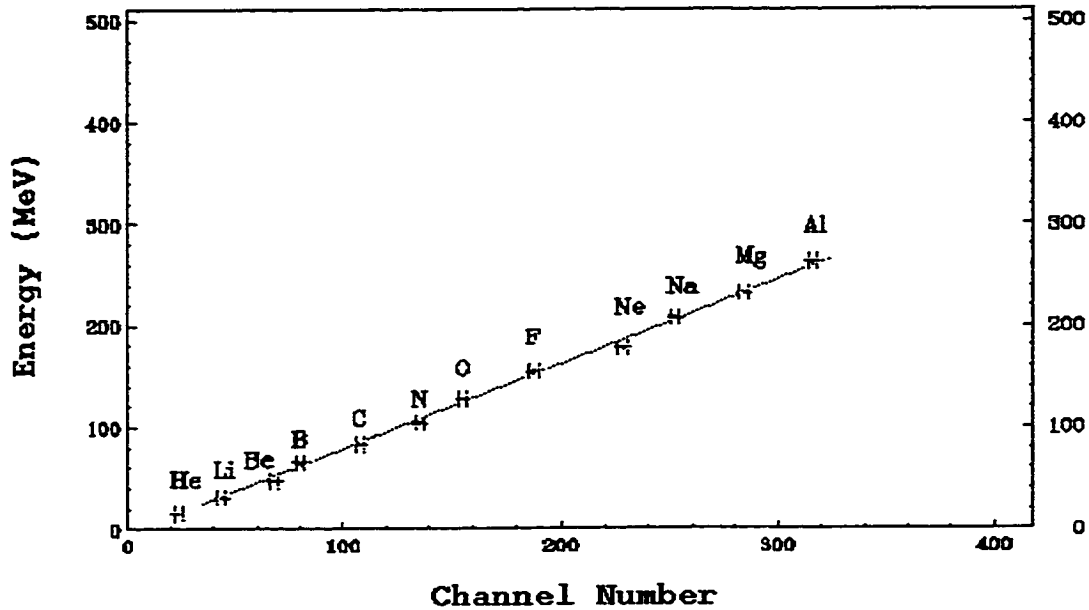
Figure 3.2: Energy calibration curve of a Si detector

or fragment) is given by

$$TOF = \Delta T + TOF_{leading\ particle}. \tag{3.1}$$

Where the ΔT is the measured time difference between the particle (fragment) hitting one detector and the "leading particle" that hit another detector. The absolute $TOF_{leading\ particle}$ is assigned by using the following method: if the leading particle is identified (in the ball), $TOF_{leading\ particle}$ can be determined by its energy and mass; otherwise, we use the beam velocity to estimate the $TOF_{leading\ particle}$. Typically the value of $TOF_{leading\ particle}$ is $\sim 3 - 6 ns$. So the TOF calibration can be mainly reduced to the calibration of ΔT.

In general, the time T of a detector can be calibrated as

$$T = (C_0 - C) * \alpha. \tag{3.2}$$

where the C's are channel numbers and α is the gain of the TFC. In our experiment, the START/STOP mode of FERETs are set as a common stop, so the reference channel C_0 is at a higher channel. The gain α is measured by inputing pulses with a constant time interval of $20ns$ into the TFC of each detector. Since the ΔT in equation 3.1 is defined by two different detectors, one is a main ball detector fired by the "leading particle" and the other is a silicon detector fired by a heavy fragment. We first need to normalize the offsets of all the detectors, or to define the relative offsets for all the detectors. A pulse was used to obtain these relative offsets as follows: input a pulse into ball summer and then input a second pulse, into each discriminator (one by one). The relative offsets of the Si detectors were corrected by normalizing the calculated ΔT of a Si detector to that of the HRA behind it. With these relative offsets, the ΔT can be written as follows:

$$\Delta T = ((C - C_r) * \alpha)_L - (C - C_r) * \alpha, \qquad (3.3)$$

where C is the recorded channel number, C_r is the relative offset, and the subscript $()_L$ represents the detector hit by the "leading particle". The final calibration parameters of the ball sets as well as the Si detectors are summarized in Table 3.1.

In the program of phy_tape (decribed in section five), we compare $(C - C_r) * \alpha$ of the ball detectors to find the leading particle, hence to calculate ΔT for Si detectors by equation 3.2. The total uncertainty of the TOF calibration process is about 3ns. Figure 3.3 shows Energy-Time 2D data of one of the Si detectors, with a correction for the Pulse-Height Defect as decribed in the

next subsection.
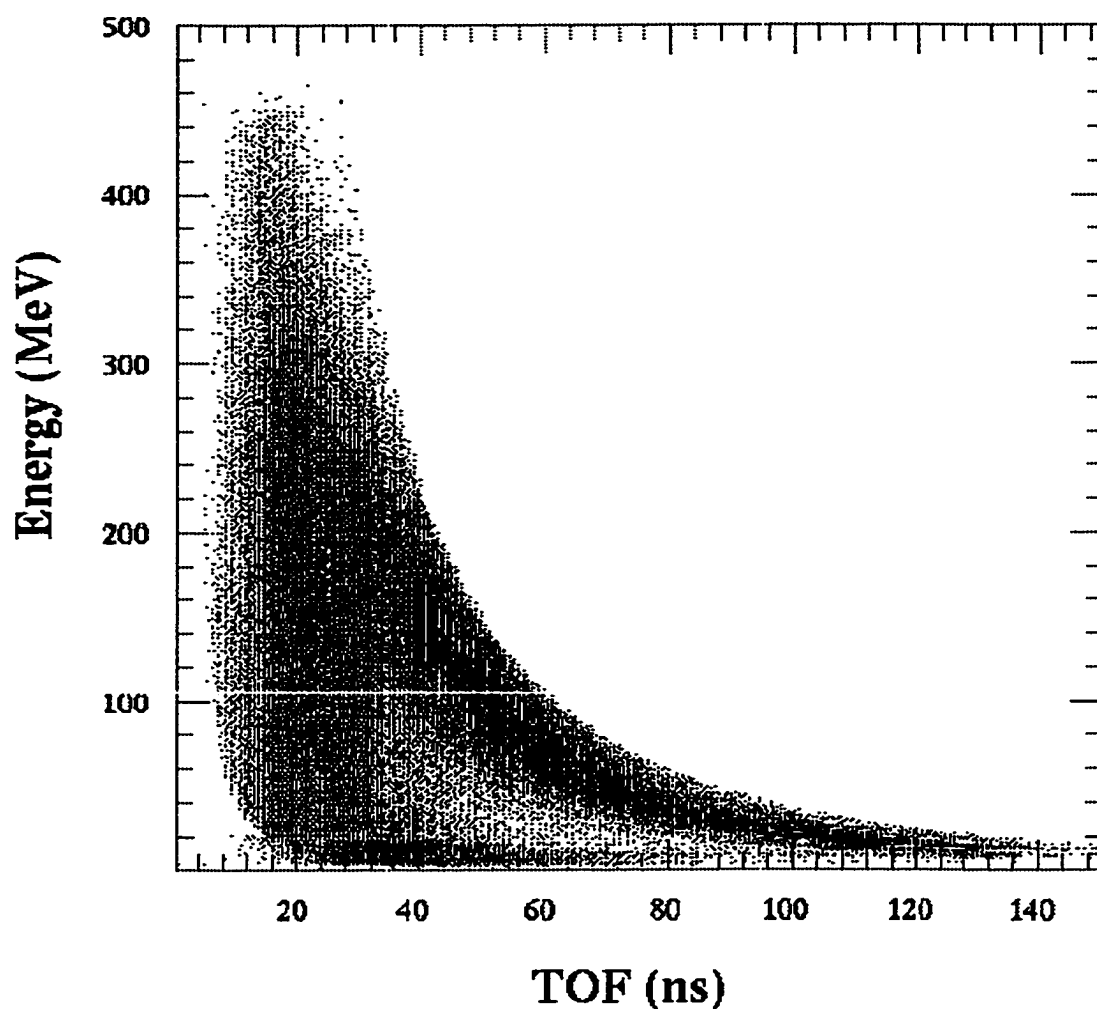
Figure 3.3: 2D energy-time spectrum of Si detector. The data are selected from the reaction of 17 ^{40}Ar+ Ag.

3.2.3 Correction for the Pulse-Height Defect

For the heavy fragments, one must correct for the energy non-linearity of each Si detector. This non-linearity is given by the pulse-height defect (PHD) which is the difference between the detector responce to a heavy ion and to

Bank number	Slope (ns/Channel)	C_r	Detectors
1	0.0901	1340	odd_a
2	0.0861	1330	odd_b
3	0.0794	1294	odd_c
4	0.0824	1380	odd_d
5	0.0798	1469	odd_e
6	0.0828	1312	odd_f
7	0.0848	1312	eve_a
8	0.0821	1312	eve_b
9	0.0848	1345	eve_c
10	0.0881	1336	eve_d
11	0.0811	1314	eve_e
12	0.0804	1305	eve_f
13	0.0909	1312	RF
14	0.0878	1315	HRA 1-15
15	0.0881	1316	HRA 16-30
16	0.0871	1321	HRA 31-45
17	0.0449	1328	Si 33-45
18	0.0871	1132	MFA
19	0.0826	1252	Si 17-32
20	0.0780	1140	ZDD
21	0.0800	1328	Si 1-16

Table 3.1: Summary of time calibration parameters.

an alpha particle of the same energy loss. We use the method suggested by J. B. Moulton [Mo78] to make this correction, which can be summarized by the following two equations:

$$PHD = 10^b E_d^a \qquad (3.4)$$

and

$$a(A) = 0.03486(A^2/10^4) + 0.5728$$

$$b(A) = 0.2840(100/A) + 0.0381 \qquad (3.5)$$

where E_d is the deposited energy, which gives the true total energy if we ignore the the energy loss in the dead layer, a and b are two mass dependant parameters.

In practice, the measured energy E_α is based on a linear calibration for the relatively lighter fragments, which is related to E_d by $E_d = E_\alpha + PHD$. Since the mass A' of a heavy fragment can only be calculated by the energy before the correction (E_α), and in equation 3.5 the mass A should be calculated from the energy after the correction (E_α), this leads to an iterative calculation. From the relationship of $A'/A = E_\alpha/E_d$, we can derive a recurrance formula as

$$E_{n+1} = \frac{28.4\frac{E_\alpha}{A_n}}{0.0381 - log(PHD) + [0.5728 + 0.0348(\frac{A_n}{E_\alpha})^2\frac{E_n^2}{10^4}]logE_n} \qquad (3.6)$$

with an initialization condition of

$$PHD = (-6.0 + 0.3A_0)E_\alpha/100 \qquad (3.7)$$

to ensure convergence, where A_0 is the mass calculated from E_α and n is the

order of recurrence. The recurrent calculation is stopped with the condition that the step differences of both mass and energy are less than 1 unit.

3.3 Matching of Telescopes

The energy of a charged particle that is deposited in a unit length of material, dE/dx, is proportional to the square of its charge and inversely proportional to the square of its velocity, and to its mass,

$$\frac{dE}{dx} \propto \frac{z^2}{mv^2}.$$ (3.8)

Where z, m and v are charge, mass and velocity of the particle, respectively. A plot of dE/dx versus the particle's residual range will look something like that shown in Figure 3.4 In this figure the BCC, ΔE and E represent the ionization chamber, the fast and the slow elements of the ball detector respectively. If a particle has an energy large enough to give a strong signal in the slow scintillator element, the identification will make use of a ΔE-E contour map. The response functions, as determined from a previous calibration experiment [Ce92], are given by:

$$C_{fast} = aE_{fast}^{\alpha} - b \quad and \ by$$

$$C_{slow} = C\left(\frac{E_{slow}^{\beta}}{A^{\gamma}Z^{\delta}}\right)$$ (3.9)

These equations convert the transformed fast and slow channel numbers into energy loss in the corresponding plastic detector for a fragment of mass number A and charge Z. The exponential parameters α, β, γ and δ, and arbitrary con-

stants a, b and c are determined by simultaneously fitting curves that follow this functional form.
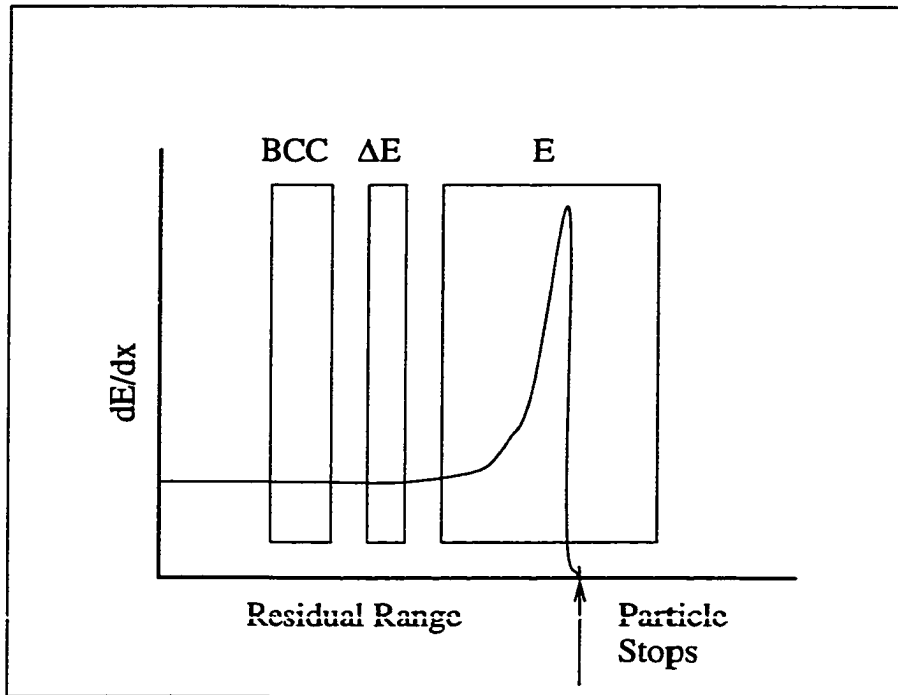
Figure 3.4: Energy loss vs. residual range of ball telescope.

For a particle stopped in the fast scintillator (or if the signal in the slow scintillator is too weak), we use BCC-ΔE contour maps for the identification. The calibration of BCC-ΔE maps is accomplished [Ce91] in a similar fashion to that for phoswich calibration. The formulae are given by:

$$C_{BCC} = aE_{BCC}^{\alpha Z + \epsilon} \qquad and\ by$$

$$C_{fast} = b(\frac{E_{fast}^{\beta}}{A^{\gamma}Z^{\delta}}) \qquad (3.10)$$

where exponential parameters $\alpha, \beta, \gamma, \delta$ and ϵ, and arbitrary constants a and b are determined by fitting the curves described by these equations to the bands

in the contour maps. Charge Z was introduced into the exponential of the transmission mode equation to better fit the data produced by using lighter ionizing gases in the BCCs.

The telescopes have several two-dimensional combinations that are used for particle identification, including Ball BCC-Fast and Fast-Slow, HRA, MFA and ZDD Fast-Slow, and Si-HRA Fast. All of these combinations, except the last one, are analysed by a matching program MTK. The MTK is a revised program with graphic language Tcl-TK for the particle identification of the MSU 4π array, which includes functions of both PIKMAKE and BRAGGMATCH[Pa96].

Figure 3.5 shows a display of MTK for $\Delta E - E$ matching of an HRA detector in the reaction of 65 A MeV Ar + Ag; the left panel shows the $\Delta E - E$ maps for raw data, the right panel is the transformed map with the following mapping algorithms [Ce92]:

$$L_{fast} = G_{fast} \times [(C_{fast} - Y_0) - (C_{slow} - X_0)M_n] \quad and$$

$$L_{slow} = G_{slow} \times [(C_{slow} - X_0) - (C_{fast} - Y_0)/M_p] \tag{3.11}$$

where L_{fast} and L_{slow} are transformed channel numbers, which are proportional to the light produced in the fast or slow scintillators. The G_{fast} and G_{slow} are multiplicative gain factors; X_0 and Y_0 are the coordinates of the intersection point of the neutral line and the punch-in line; and M_n and M_p are the slopes of the neutral and punch-in lines. The six mapping parameters are stored for each detector after fitting the data in the corresponding matching band. The mass number A and charge Z can be obtained from the particle

identification (PID) lookup tables, which is a matrix of transformed channel numbers pointing to a unique A and Z. Similarly, the energy E is obtained from "MeV lookup tables" which convert the transformed channel numbers into the the kinetic energy. The matching for BCC-ΔE follows same process.

For the matching of Si-HRA fast, we follow same process. Each PID and MeV lookup table is created from a sample display of a (Si-HRA fast) 2D map for each Si detector.

3.4   Physical Tape – Summary of Data

When one has all the calibration information, he is ready to create physics tapes, which record data event by event with the multiplicity of that event and six physics parameters for each particle: mass A, charge Z, polar angle θ, azimuthal angle ϕ, energy E and detector number. The physics tape is then produced with program Phytape_93021 which is a revised version to deal with the newly added Si detectors, including the TOF calculation and Pulse-height defect corrections. Following is a schematic list of the logic stream of Phytape_93021.

1. Phytape_init: Load all the configuration and calibration files.
2. Get_a_buffer: Read in a buffer of data and check buffer.
3. Process_buffer:
   a. Find FFM header: count the number of detector fired.
   b. Find FERA/Silena header: extract the CRATE, and SLOT.
   c. Separate each word into two part: Subaddress and Data.
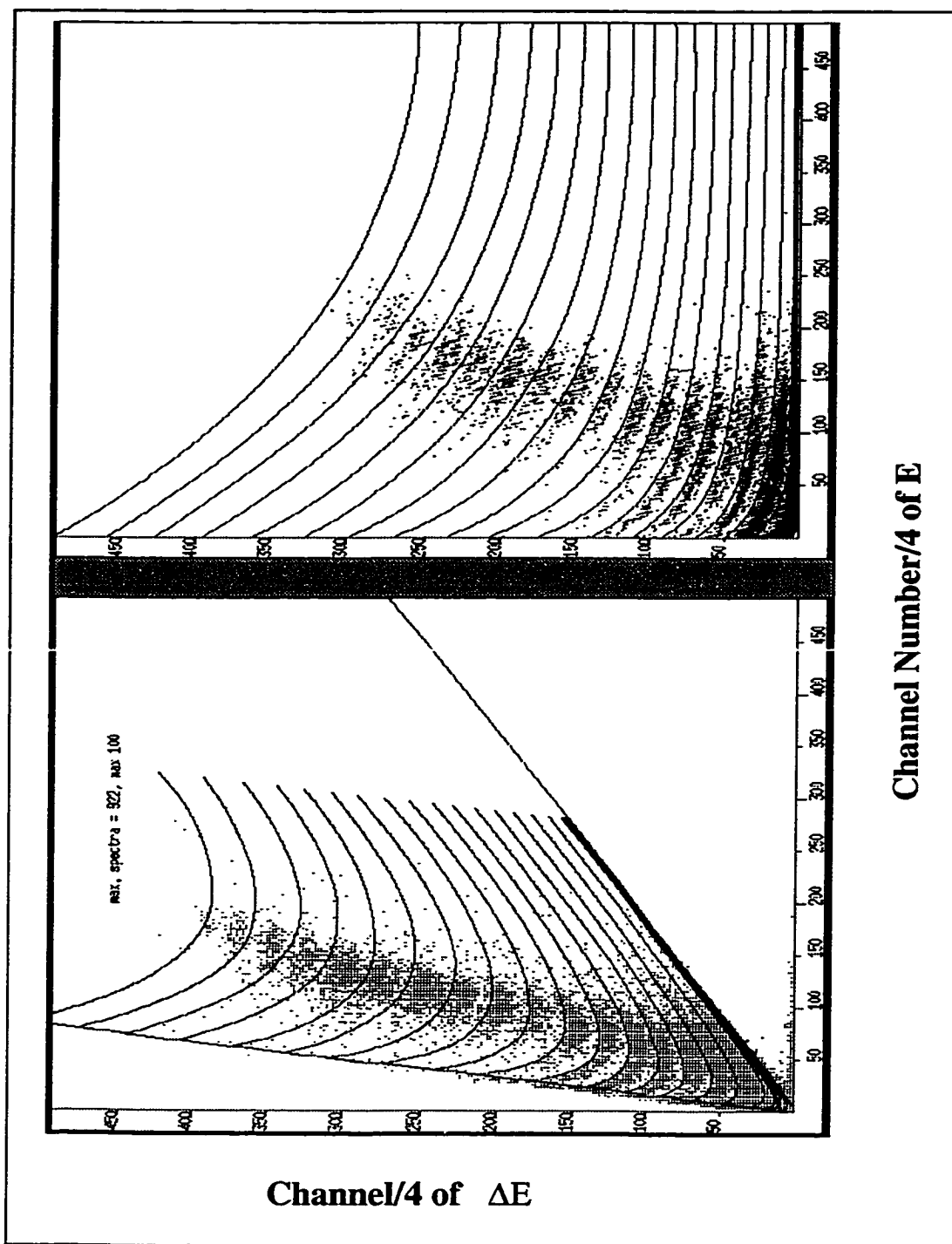
Figure 3.5: A 2D histogram of ΔE-E integrated signal for MFA phoswichs. The data are ^{40}Ar + Ag of 65MeV/nuclean at polar angle $\theta \sim 5^0$.

Extract raw data in channel numbers for T, ΔE, E;

Record detector number;

Transfer Time data in form of $\Delta T' = (C_0 - C) * \alpha$;

enddo c.

enddo b.

enddo c.

4. Increment_buffer:

for each event {

determine the kind of matching telescape;

Transform channel with matching parameter;

Get A and Z from PID table;

Get E from MeV table;

for case of stopping in Silicon: {

Get E from parameter of Si energy calibration;

}

comparing $\Delta T'$ to find the leading particle

Get θ and ϕ from geometrical table;

record physics buffer as:

A, Z, θ, ϕ, E, Idet; for normal case

A, Z, $\Delta T'$, -5, E, -Idet; for case go through Si

-100,-100,$\Delta T'$, -4, E, -Idet; for case stopped in Si

} end event

Calculate the TOF of leading particle.

for that event: {

    for case of -Idet: {

    calculate time, $TOF = (\Delta T'_{leading\ particle} - \Delta T') + TOF_{leading\ particle}$;

    calculate velocity v by TOF;

    for case stopped in Si: {

        Use TOF and initial E, recurrently calculate the mass A and

        final E with method of Section 3.1.2.}

    record phyics buffer as:

    A, -A/2, TOF, 100v, E, -Idet; }

}

The physics tapes in this format can be sorted and analysed by the ADF macros (http://nucwww.chem.sunysb.edu/dali/ADF.html). Many analysis programs have been generated with those macros for different purposes. We also create simulation tapes in the same format, so that we can compare simulated results with experimental results by using the same analysis programs.

Chapter 4

Splintering Central Collisions

4.1 Introduction

Heavy-ion reactions at incident energies of $\sim 15 - 150$ MeV per nucleon have been of considerable experimental and theoretical interest in the last decade. They cover the transition from mean-field dynamics in the low-energy domain[Sc84] to two-body nucleon-nucleon collisions in the high energy domain[Kr89]. For mass asymmetic reactions at only slightly above Columb barrier energies (e.g. < 10 A MeV), there is essentially complete fusion and essentially complete thermalization into a compound nucleus e.g.[Ba80]. As the incident energy is increased from ~ 10 to 35 A MeV, the fractional momentum transfer in such fusionlike reactions slowly declines e.g.[Mo84, Vi82, Ma96] and is accompanied by a small percentage of forward-peaked, prethermalization particles e.g. n, ^{1,2,3}H, and ^{4}He. For higher, but still intermediate energies, (e.g. ~ 35 to 150 A MeV), attention to date has been mainly focused on testing models for multifragmentation of the hot nuclei produced, and a consistent

picture has not emerged for the dynamical mechanisms of energy dissipation and thermalization. One class of experiments implies an essential domination by two-body, deeply inelastic reactions, even for the central collisions e.g.[Qu93, Na95]. Another implies a possible continuation of incomplete fusion, possibly followed by very rapid and even explosive decay into fragment and particle emission e.g.[Na95]. This latter process could send out a cloud of nucleonic smoke and ashes and leave no clear indicator for the overall impact pattern in the form of a heavy residual nucleus e.g.[Au86].

It is measurements of such heavy residual nuclei that have provided the classic probes of linear momentum transfer e.g.[Mo84, Vi82, Ma96], and it is their associated ejectile multiplicities that have given major probes of the initial energy deposition e.g.[Pi91]. The combination of such measurements has not been jointly pursued for intermediate energy heavy ion reactions, particularly including the rather slow moving, heavy fragments[Yo92].

In this chapter, the data of 17-115 A MeV ^{40}Ar + Ag are presented for a systematic study of the incident beam energy and impact parameter dependence of the mass and velocity of the heavy residual nuclei in conjuction with the light charged particles and fragments. Results for other systems have also been studied and are presented in the thesis of Eric Colin [Co98]. These results lead to an overview of the evolution of incomplete fusion ($\sim$ 17-44 A MeV) into splintering central collisions ($\sim$ 44 - 115 A MeV), a new mechanistic classification. The multiplicities and velocities of various charged particles and fragments are also investigated to seek an overview of the momentum and mass balance as a function of incident energy.

4.2 Overview of mass and velocity distributions

To obtain a generalized understanding of the reaction dynamics, we present distributions of heavy residual nuclei, the light charged particles and intermediate-mass fragments (IMF) as contour maps in velocity vs mass. Data for 44 A MeV ^{40}Ar + Ag are selected to show various details in Figure 4.1. The left hand panels show detected multiplicity distributions, the shaded parts indicate the multiplicity gates used. The middle panels show mass distributions and the right hand panels show 2d maps of velocity vs mass corresponding to the multiplicity gates in the left hand panels. All the events are hardware conditioned by two hits in the ball and software selected with "completeness" requirements for inclusion of $\geq$ 75% of system charge and $\geq$ 70% of the incident momentum. Without multiplicity selection, as shown in the bottom row, an overall view of the products is displayed in various mass and velocity ranges. When we select the lowest 15% multiplicity as shown in the middle row, these products are clearly grouped into projectilelike fragments (PLF) with velocity close to projectile velocity ($V_{\parallel}/V_{c.m.}$ = 3.7) and targetlike fragments (TLF) with a very low velocity. However, for the selection of highest 15% of multiplicity as shown in the top row, the fragments have lost their resemblance to projectilelike and targetlike fragments.

Figure 4.2 gives an overview series of contour maps in mass and longitudinal velocity $V_{\parallel}/V_{c.m.}$ for the charged ejectiles from mid-central (or mid-peripheral) collisions. These reactions were triggered by two or more hits in the ball plus a software requirement of low overall charged particle multipli-
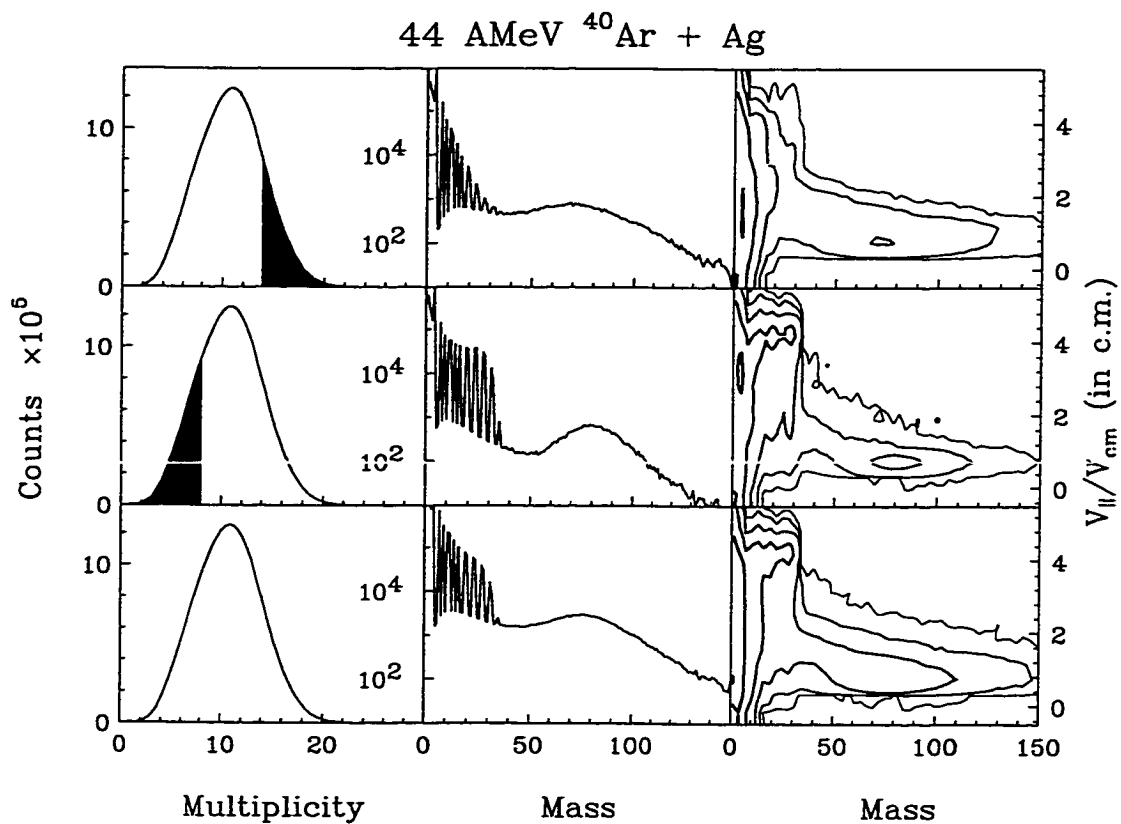
Figure 4.1: Velocity vs mass distributions for different multiplicity gates for 44 AMeV ^{40}Ar + Ag. The neighboring contour lines in right hand panels are changing by a factor of 10.

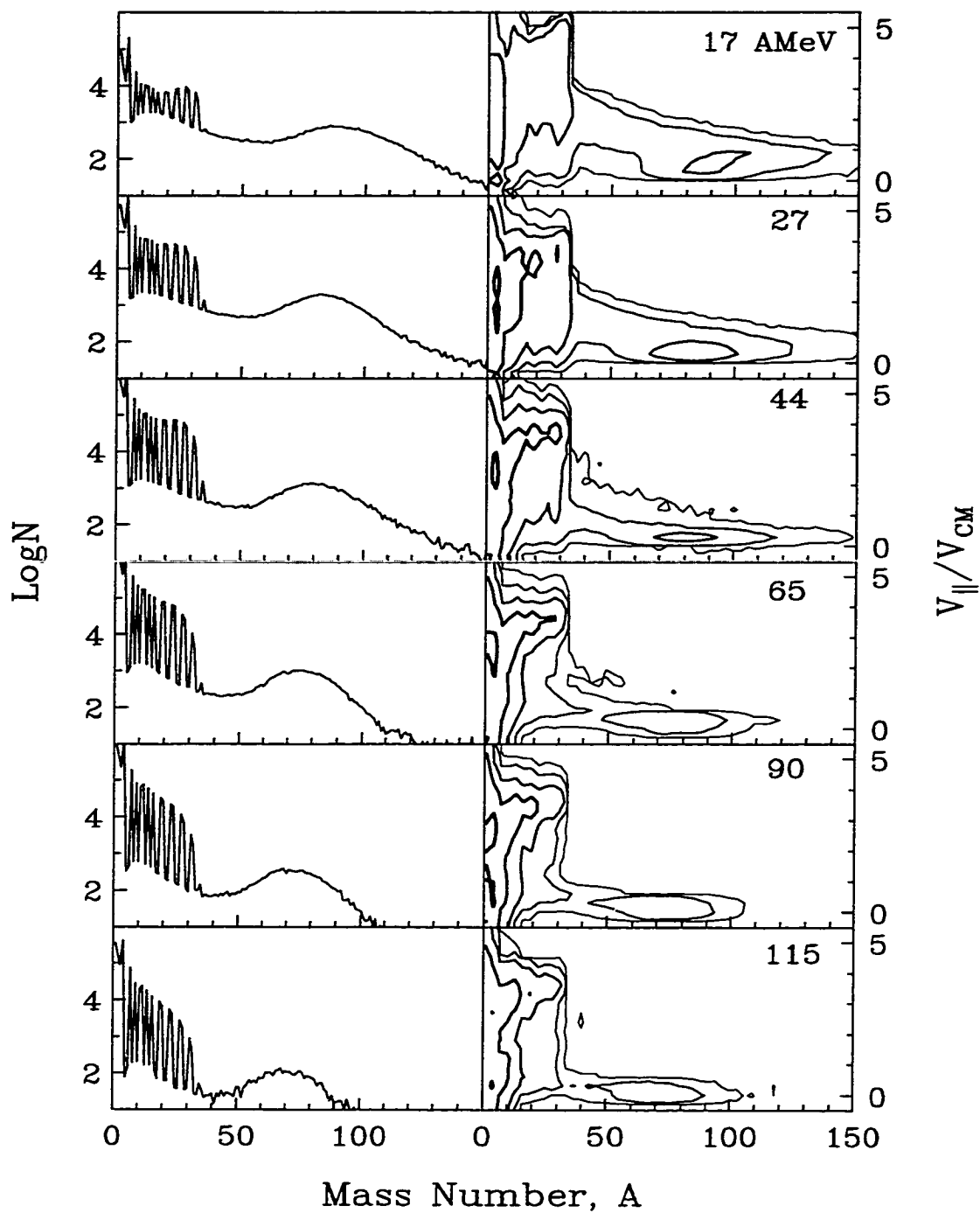Figure 4.2: Velocity vs mass distributions for low multiplicity gates for ^{40}Ar + Ag. The neighboring contour lines in right hand panels are changing by a factor of 10.

city (i.e. the lowest 15%). The most peripheral collisions were excluded by the hardware trigger condition, while the most central were excluded by the low multiplicity requirement. For all energies, one sees clear signatures of the well-know deep-inelastic reactions (DIR). There is a finger of projectilelike fragments (PLF) with velocity and mass near to that of projectile ($A \sim 30$, $V_{||}/V_{c.m.} = 3.7$) and a group of targetlike fragments (TLF) with mass near to that of the target ($A \sim 90$) and a very low velocity of $0.25 < V_{||}/V_{c.m.} < 0.5$. In addition, there are small contributions from fusion like reactions for the low energies (< 44 AMeV), with heavy fragments that have velocities of $V_{||}/V_{c.m.} \sim 0.8$ and mass up to 130.

Figure 4.3 also shows mass velocity information but now gated by the highest 15% of the overall multiplicity. In contrast to Figure 4.2, for these high-multiplicity and more central collisions, the yield-mass curves change continuously with increasing energy. A peak for fusion evaporation residues[Ma96] at $V_{||}/V_{c.m.} \sim 1$ and $A \sim 100\text{-}130$ for 8 (not shown) and 17 A MeV[Et92] evolves into a broad smear of lower masses as the incident energy is increased to $\geq$ 44 A MeV. Also, there is a growing group of lighter fragments of $A \lesssim 20$ with velocities quite different from that of projectile. These intermediate mass fragments (IMF's) have essentially lost their resemblance to projectilelike and targetlike fragments, i.e. the finger at $V_{||}/V_{c.m.} \sim 3.7$ has been smeared out and even obliterated for $E/A > 44$ MeV. The heaviest fragment group changes with energy in a very regular way. Its average velocity ratio $V_{||}/V_{c.m.}$ drops steadily from ~ 0.9 at 17 AMeV to ~ 0.3 at 115 at MeV, and similarly its average observed mass number drops from ~ 100 to ~ 55.

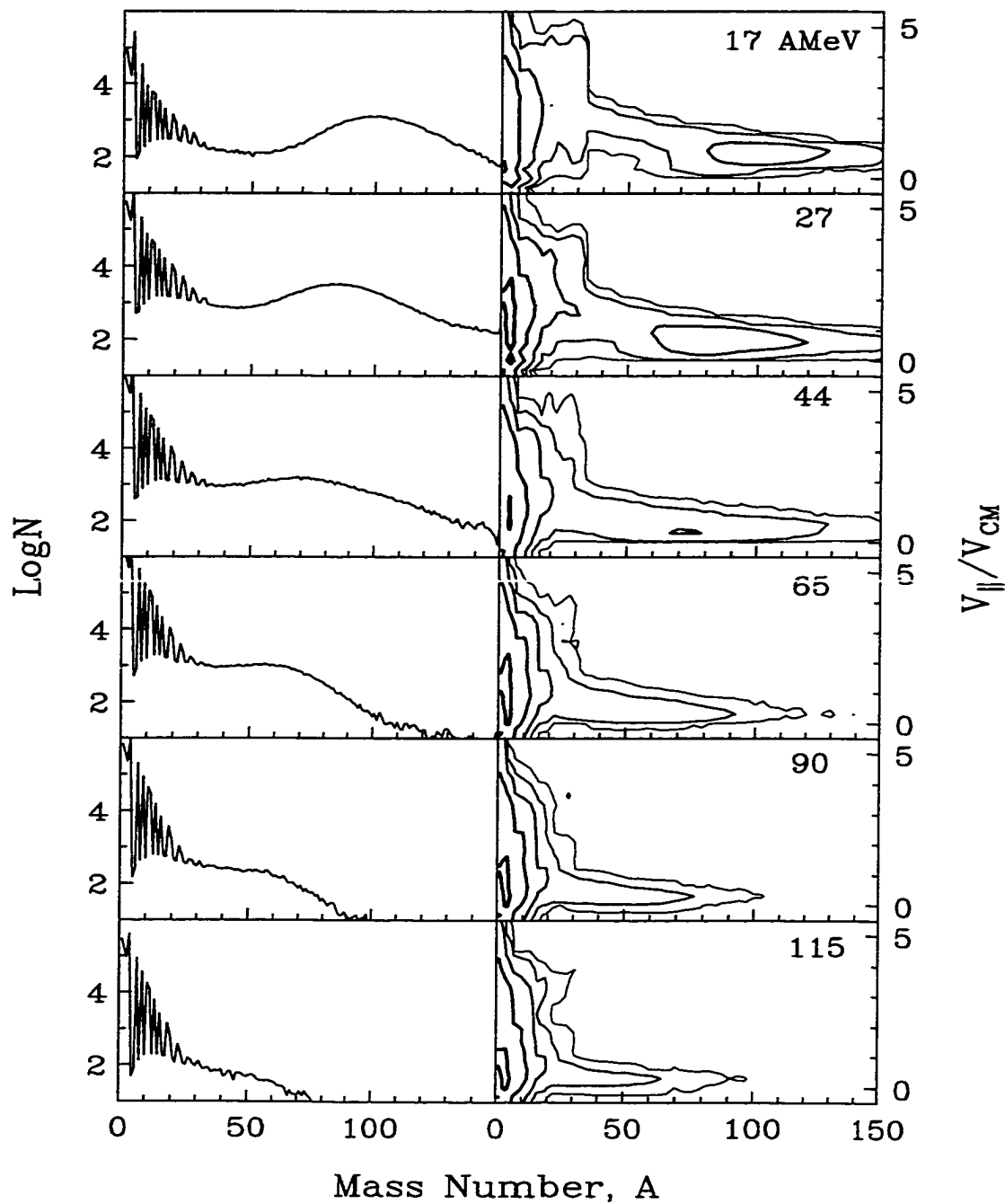# ^{40}Ar + Ag, High Multiplicity Gate

Figure 4.3: Velocity vs mass distributions for high multiplicity gates for ^{40}Ar + Ag. The neighboring contour lines in right hand panels are changing by factor of 10.

For the low multiplicity gate as indicated by Figure 4.2, the fast PLF's and slow TLF's are dominant as is the case for all of the more perpheral reactions for all targets and all energies. By contrast for the high-multiplicity cut (Figure 4.3), a remarkable evolution is indicated as the energy increases. There is a dominant peak for the well-known incomplete fusion process with an evaporation residue ($A \sim 90$ and $V_{\parallel}/V_{c.m.} \sim 0.8$) in coincidence with predominantly forward peaked lighter fragments for the low energies up to 44 AMeV. As the energy is increased to 65 AMeV, we see a heavy fragment with $A \sim 60$ and $V_{\parallel}/V_{c.m.} \sim 0.3$ along with very light IMF's of $A \sim 10$ and a wide range of velocities. It is this class of reactions that we refer to as splintering central collisions. The projectile has been shattered or splintered into a number of light fragments and particles, largely forward peaked in the c.m. frame and with a wide range of longitudinal velocities. A heavy fragment remains, moving rather slowly, but carrying more than 1/4 of the momentum from the collision (more such results are indicated in next section). The majority of the momentum is distributed over the set of light ejectiles comprising a forward-peaked spray.

4.3   Distributions of ejectile velocities and multiplicities

For the most violent collisions (selected by their high charged particle multiplicity) we seek an overview of the momentum balance as a function of the incident energy. In Figure 4.4(a), we show the average velocity ratio $<V_{\parallel}/V_{c.m.}>$ and in panel (b) the average multiplicity for the various fragments

detected in each event. For 17 and 27 A MeV ^{40}Ar + Ag, the heaviest fragments of A $\gtrsim$ 50 have average velocities very close to the c.m. velocity (i.e. $\approx$ 0.9) typical of incomplete fusion [Ma96]. By contract, the fragments of subprojectile mass (A $\leq$ 40) have much higher average velocity ratios characteristic of a persistance of the projectile motion.

As the incident energy is increased to $\gtrsim$ 44 A MeV the typical observed light fragment exhibits smaller mass (Figure 4.2), while its high average velocity ratio persists (Figure 4.3). By contrast, for the heavier fragments, (A $\gtrsim$ 50) the average velocity ratio continually decreases with energy for the complete range of heavier masses (Figure 4.3). Recall that the c.m. system is also the zero-momentum system so that fragments with velocity ratios below unity must be accompanied by ejectiles with velocity ratios greater than unity. In Fig. 4.4 (a) we show values of the velocity ratios for the lighter ejectiles in coincidence with the heaviest detected mass in the event. The idea is to show a complementarity in these c.m. velocities for the lightest and the heaviest detected ejectiles, i.e. a match between high and low velocity ratios that accounts for the linear momentum balance. Such complementarity is clear in Figure 4.4 for each energy; all light ejectiles have velocity ratios above unity while the heavy fragment always has a ratio below unity.

One must also examine the average ejectile multiplicities, which are of equal importance for the momentum balance. Multiplicities of the light ejectiles are shown in Figure 4.4 (b); these average multiplicities increase monotonically with increasing beam energy. Roughly speaking the light ejectiles comprise only $\sim$ 10% of the total mass for 17 A MeV while they increase to $\sim$ 50% for
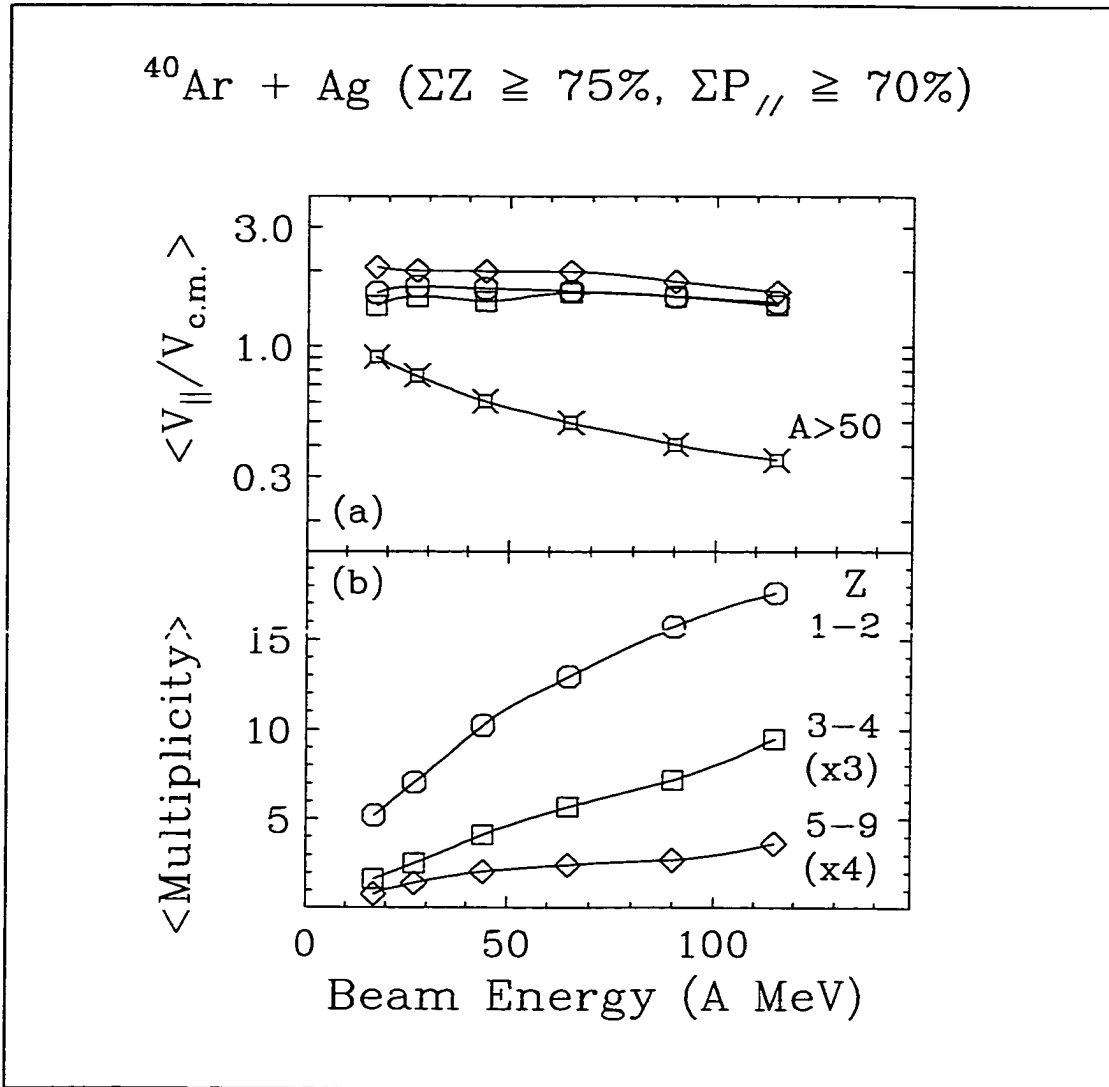
Figure 4.4: (a) ^{40}Ar + Ag: Average velocity ratio $<V_{||}/V_{c.m.}>$ for heavy fragments of A $\geq$ 50 (i.e. an average over each plateau in Figure 4.3) and for lighter ejectile groups in correlation with them. (b) Average observed multiplicities of these light fragment groups in coincidence with a fragment of A$\geq$ 50.

115 A MeV. Correspondingly the mass of the typical heavy residual nucleus decreases from ~90% to $\lesssim$ 50% of the total mass. Let us try to construct an overall picture that can account for these results for near central collisions

4.4 Summary

In this chapter, we have presented measurements for near 4π detection of light charged ejectiles along with slow moving heavier nuclei. For 8–44 A MeV the results for the most violent (highest 15% of the multiplicities) collisions show majority momentum transfer typical of complete and incomplete fusion. For 65-115 A MeV the most violent (highest 15% of the multiplicities) reactions exhibit majority momentum retention by an ejectile spray from splintering central collisions. This spray consists of a complex collection of light charged ejectiles with a wide range of velocities that is very different from the incident projectile.

Chapter 5

Nuclear Stopping and Energy Removal in Central Collisions

5.1 Introduction

Central collisions between mass asymmetric heavy nuclei of $\sim$ 10 - 100 A MeV deposit substantial amounts of energy into a core nuclear system, e.g. for $\sim$ 100 A MeV ^{40}Ar + Ag one finds $\gtrsim$ 1 GeV (or $\gtrsim$ 10 MeV/nucleon [Co98]). One expects that the addition of energy to a nuclear system will cause it to expand in size and ultimately lead to its disassembly, but we do not yet have a systematic picture of the evolution from nuclear evaporative decay to such disassembly. In this spirit we study the reactions of Cu, Ag and Au with ^{40}Ar from 8-115 A MeV. What are the roles of nuclear stopping vs transparency in these reactions? What fragments carry away the undissipated energy, and what ejectiles remove energy via isotropic emission from the very highly excited core nucleus? Is this pattern of energy removal consistent with expectations for an equilibrated nuclear system? Is there any evidence for a

liquid-gas phase transition e.g. [Po95]? These are questions that we address in this chapter.

In this chapter we focus on the multiplicities, angular, and energy distributions of charged ejectiles. As described in the last chapter, we select violent central collisions via the highest 15% of the multiplicity distributions, and we require that each event include $\geq$ 75% of the system charge and $\geq$ 70% of the incident momentum. In section two, we group the various ejectiles into two components: (a) an isotropic component in the moving frame of the heaviest fragment and (b) a forward-peaked component in this frame [Ma96]. In section three, we determine the average linear momentum for various ejectile types of each component and hence characterize the residual system after the forward ejections and prior to the isotropic emission. Similarly in section four, we determine the energy removal by the ensemble of isotropic ejectiles and hence characterize the excitation energy of this isotropic emission ensemble (usually taken as thermalized and equilibrated). In section five, the slopes of the energy spectra are studied for Z=1 and 2 particles with isotropic emission. This gives insight into the extent of equilibration and the possibility of extra thermal energy (e.g. radial flow) for the isotropic emission ensembles. These data display a clear picture of the average mass, momentum, and energy balance for these mass asymmetric reactions at intermediate energies. Comparisons to results from the widely used Boltzmann-Uehling-Uhlenbeck theory (BUU) [Be88, Da95] reveal a major inadequacy in its predictions of the nuclear stopping (or momentum transfer).

5.2 Separation of Isotropic and Forward-peaked Components

For mass asymmetric reactions in the near-barrier energy domain of $\lesssim$ 10 A MeV it has been conventional to separate light ejectile emission into an isotropic and a forward-peaked component, commonly termed the evaporation and direct components e.g. [Ma96]. For incident energies greater than $\sim$ 30 A MeV, experiments have often been performed with near 4π detector arrays that give a wonderful view of the light or fast ejectiles[Du97]. Often these arrays are not sensitive to the low-velocity heavy fragments. Without such heavy fragment detection one has no independent handle on a source velocity for isotropic emission; therefore, it has not been possible to separate these two components with good confidence. The multisource fits to inclusive particle spectra have been appropriately characterized as simply multiparameter fits.

In our experiment, the heavy fragment velocities are measured and used, along with the 4π array for the light particles and fragments, to separate H, He, Li and fragments of $4 < Z < 17$ into isotropic and forward-peaked components in the frame of the heaviest fragment. Using data for the reactions of Ar + Ag, the procedure is illustrated as following. The events are selected by the highest 15% of the charged particle multiplicity (i.e. for the central collisions). For events that include a heavy residual fragment, its detection is required by the completeness condition of $\geq$ 75% of detected charge and $\geq$ 70% of detected momentum. Mass and velocity limitations are then applied for these heaviest fragments as listed in Table 5.1. These conditions exclude the fission

events, especially at low energies, fragments near to projectile velocities and IMF's.

Beam Energy (A MeV)	Mass Gates (Mass Number, A)	Velocity Gate (cm/ns)
17	$58 \leq M_{HF} \leq 140$	$V_{HF}/V_{cm} \leq 2.0$
27	$50 \leq M_{HF} \leq 140$	$V_{HF}/V_{cm} \leq 1.5$
44	$50 \leq M_{HF} \leq 130$	$V_{HF}/V_{cm} \leq 1.0$
65	$30 \leq M_{HF} \leq 130$	$V_{HF}/V_{cm} \leq 1.0$
90	$30 \leq M_{HF} \leq 130$	$V_{HF}/V_{cm} \leq 1.0$
115	$30 \leq M_{HF} \leq 130$	$V_{HF}/V_{cm} \leq 1.0$

Table 5.1: Mass and velocity gates for heavy fragments for the reactions of Ar + Ag.

The velocity of the heaviest fragment then can be determined; its velocity, on average, represents the velocity of the isotropic emission source. The various ejectiles were transformed into the frame of the average heaviest fragment. From the angular distributions of these ejectiles, samples of which are shown in Figure 5.1, an isotropic component in the heavy fragment frame is defined by reference to the detectors at laboratory angles of $\gtrsim 90^{\circ}$ or $\gtrsim 120^{\circ}$ in the moving frame. In Figure 5.1, a correction was given for losses due to the energy thresholds. This was done by fitting the energy spectra with equation 5.1 for H particles. For He particles and IMFs a common energy thresholds was applied in the moving frame. The detected isotropic multiplicities, obtained from integration of these transformed energy spectra, are listed in Table 5.2.
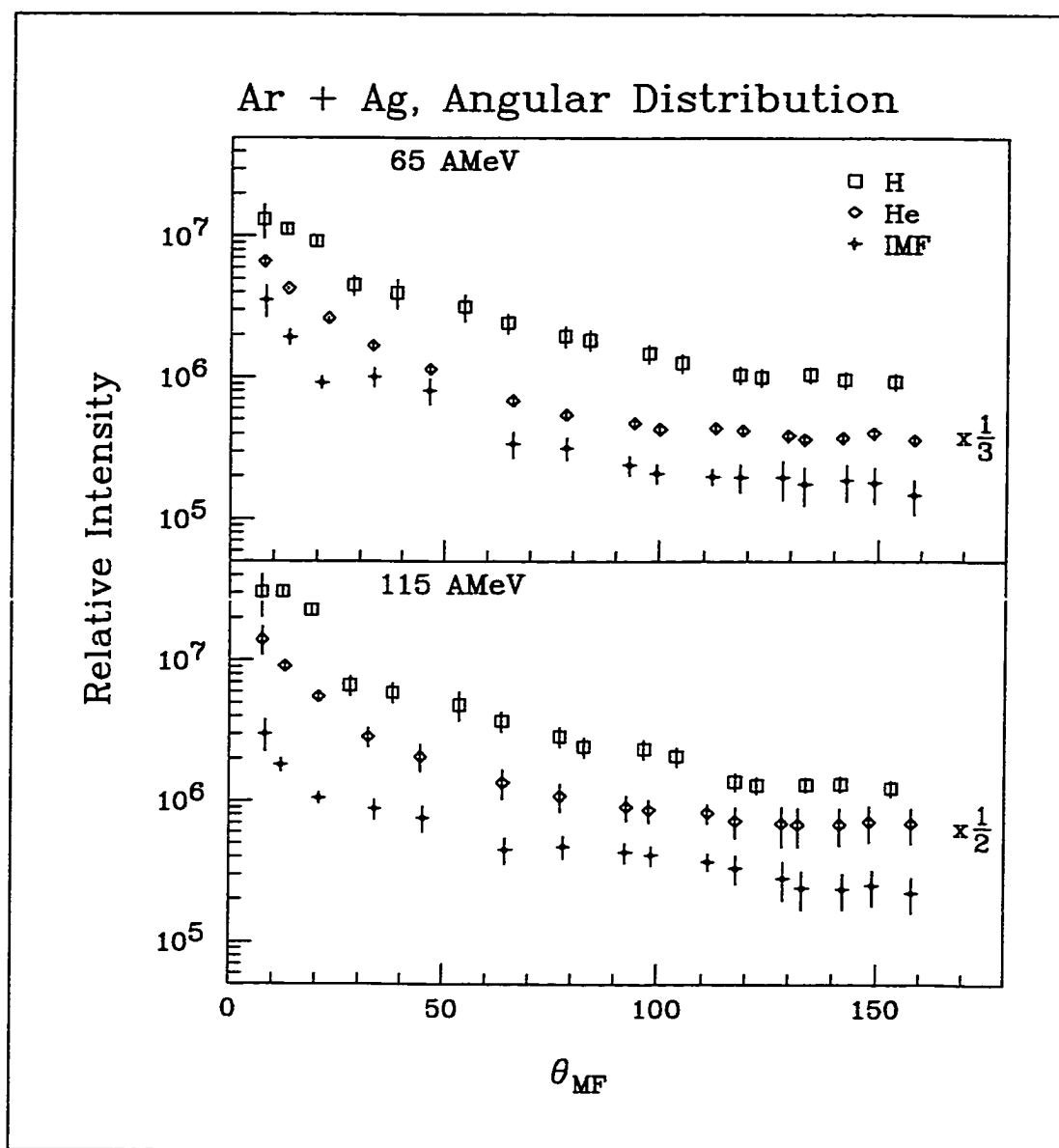
Ar + Ag, Angular Distribution

Figure 5.1: Angular distributions for Ar + Ag reactions.

Energy	H	He	Li	$4 \leq Z \leq 18$
17 AMeV	0.45	2.12	0.28	0.08
27 AMeV	0.82	2.28	0.38	0.14
44 AMeV	1.32	2.30	0.43	0.15
65 AMeV	2.24	3.41	0.51	0.25
90 AMeV	3.16	4.27	0.83	0.26
115 AMeV	3.32	4.69	1.05	0.34

Table 5.2: Detected isotropic multiplicities for various ejectiles of Ar + Ag.

The forward component is obtained from the subtraction of the detected isotropic component from total detected emission in 4π sr. The resultant is shown in Table 5.3.

Energy	n	H	He	Li	$4 \leq Z \leq 18$
17 AMeV	0.5	1.03	0.54	0.09	0.21
27 AMeV	1	1.99	1.06	0.21	0.44
44 AMeV	1.5	3.41	2.23	0.42	0.68
65 AMeV	2	4.53	2.32	0.66	0.89
90 AMeV	2.5	5.43	2.40	0.57	1.03
115 AMeV	3	5.90	2.11	0.47	1.05

Table 5.3: Multiplicities of forward component for various ejectiles of Ar + Ag.

Neutrons are not detected in this experiment; however, a number of measurements in the literature [Ji89, Cr91, Lo93, Hu97] have been used, in conjunc-

tion with our data, to estimate their average multiplicities. These estimated values are listed in Table 5.3 and Table 5.4.

Due to the high energy threshold for Z=1 particles, a correction for the isotropic component is given by fitting the transformed energy spectra with a modified Boltzman equation as follows:

$$dN/dEd\Omega = A(E - E_0)Exp(-\frac{E - E_0}{T})$$ (5.1)

The barrier parameters (E_0) were estimated from the systematics of measured spectra found in the literature [Ge94]. A correction for acceptance of the device is given for all the ejectiles. Table 5.4 shows the corrected isotropic multiplicities; the results for multiplicities for both isotropic and forward-peaked components in the heavy fragment frame are illustrated for in Figure 5.2.

Energy	n	H	He	Li	$4 \leq Z \leq 18$
17 AMeV	10	5.46	3.10	0.28	0.08
27 AMeV	11	6.11	3.23	0.38	0.14
44 AMeV	12	6.68	3.68	0.43	0.15
65 AMeV	12.5	7.58	4.51	0.51	0.25
90 AMeV	13	9.36	5.15	0.83	0.26
115 AMeV	14	10.75	5.43	1.05	0.34

Table 5.4: Corrected isotropic multiplicities for various ejectiles of Ar + Ag.

As a check of the corrected multiplicity values, we compare in Figure 5.3 the observed average residual mass with the mass difference between A_{system} and ΔA_{loss} obtained from the multiplicities for all the reactions. The average
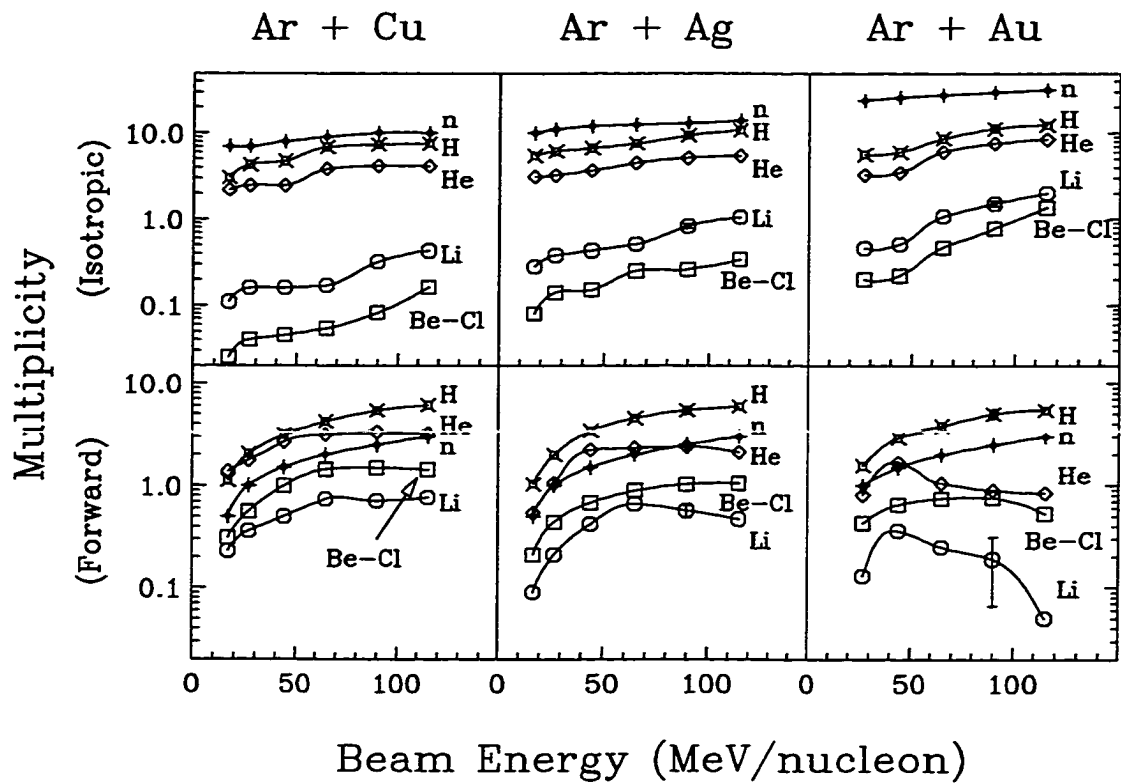

Figure 5.2: Charged ejectile multiplicities from this work for reactions of Ar + Cu, Ag and Au, and neutron multiplicities from systematic extrapolations.

masses used for ejectiles of neutron, H, He, Li and IMF were of 1, 1.4, 4, 7 and 10 respectively. Also shown in the figure is the average residual mass calculated by a statistical model [Aj96] starting with average energies and masses from the LMT method. As the beam energy increases from 17 A MeV to 115 A MeV, the average residual masses decrease from $\sim$ 80, 110 or 170 to $\sim$ 25, 55 or 100 for Cu, Ag or Au reactions respectively. The observed residual mass values are also consistent with those calculated from the ejectile multiplicities.

In Figure 5.4, we show how the system mass is distributed among the residual fragment, the isotropic emission component and the forward-peaked component in average. For all three systems, the mass of the residual fragment decreases continuously as the energy increases. At 115 AMeV, half of system mass remains for the heaviest residual fragment for Ar+Au, but less than one third for Ar+Cu. Among the emission masses, the isotropic component is dominant in the Ar+Au reactions for all incident energies; however, in Ar+Cu reactions, the masses of the forward-peaked component are comparable with that of the isotropic component, and both increase as the incident energy increases.

5.3 Longitudinal Momentum Distribution between Isotropic and Forward-peaked Components

From the multiplicities of the isotropic and forward-peaked components in section 2 and the total average velocities for the various ejectiles, we can examine the average longitudinal momenta for various ejectile types for each

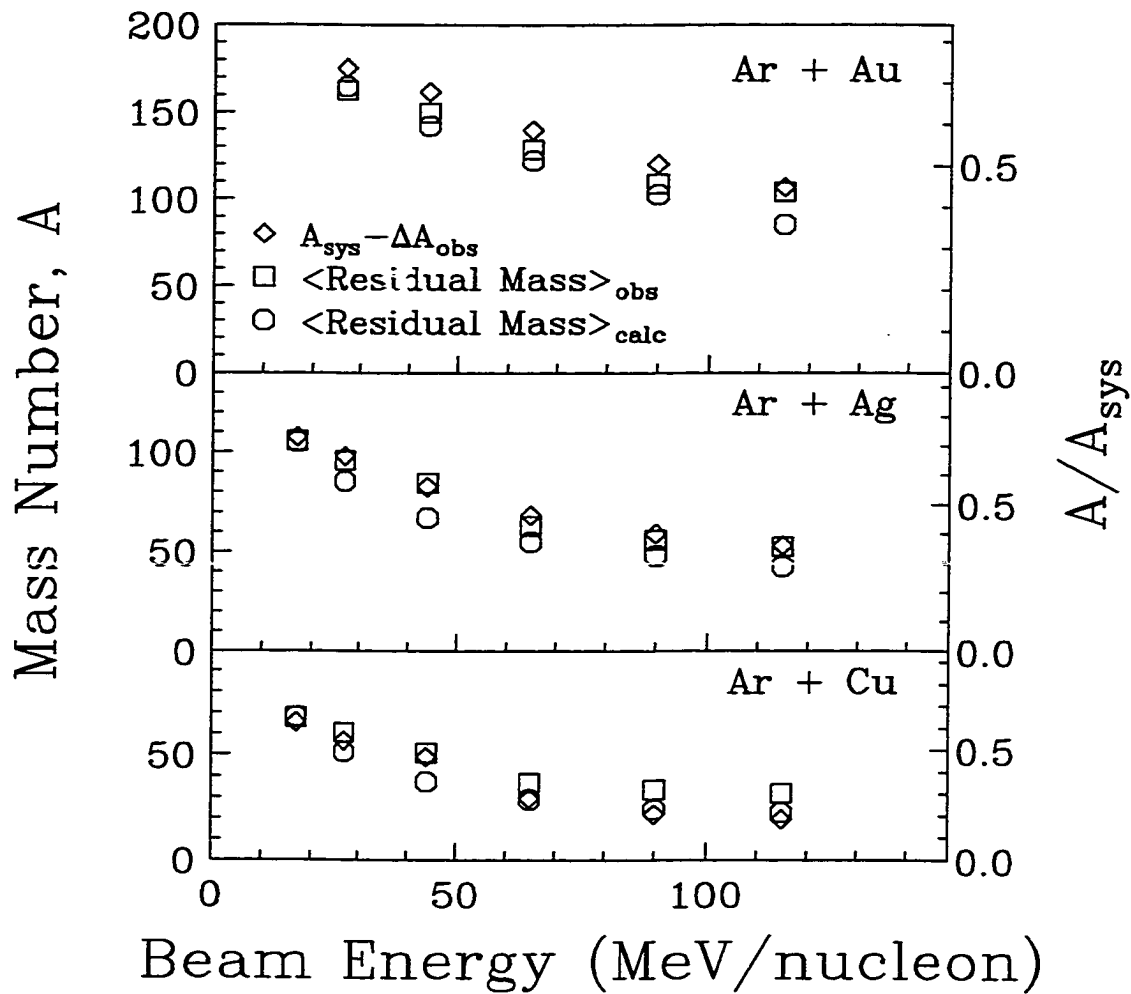Figure 5.3: Comparison of residual mass. Diamond: the difference between system mass and mass loss calculated by multiplicities of ejectiles; Square: observed residual mass. Circle: calculated mass by a statistical model [Aj96] based on the LMT measurements.
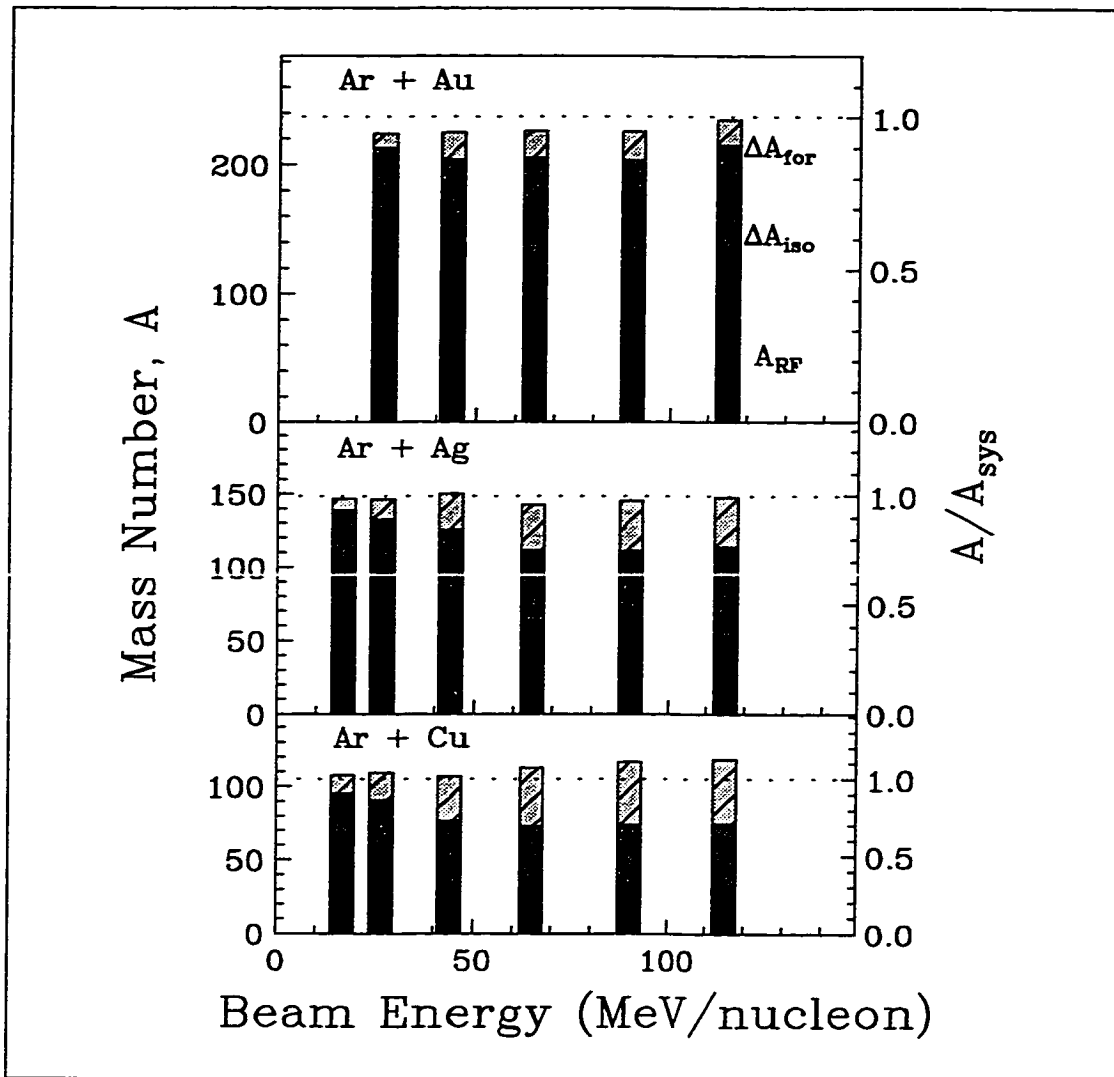
Figure 5.4: The distribution of the system mass among the heaviest fragments, the isotropic emission component and the forward-peaked component.

reaction. In the following paragraphs the average velocity means the longitudinal component of velocity, $V_{//}$. For each type of ejectile, the average velocity of the isotropic component is simply the average velocity of the slow moving heavy fragment; the overall average velocity is taken from the average of the detected velocity in the 4π array; hence the average velocity of the forward-peaked component can be extracted from the following equation:

$$M_{tot}* <V> = M_{iso}* <V>_{iso} + M_{for}* <V>_{for} . \qquad 5.1$$

the M_{tot}, M_{iso} and M_{for} are multiplicities of total, isotropic component and forward-peaked component of that type of ejectiles respectively. The average velocity for forward-peaked neutron components is assumed to be the same as that for Z=1 particles. Table 5.5 shows a sample result from this calculation for the reaction of 65 A MeV Ar + Ag.

Ejectile	M_{tot}	$<V>$ (cm/ns)	M_{iso}	$<V>_{iso}$ (cm/ns)	M_{for}	$<V>_{for}$ (cm/ns)
n				1.50		14.3
H	12.11	5.97	7.58	1.50	4.53	14.3
He	6.83	4.08	4.51	1.50	2.32	9.09
Li	1.17	2.97	0.51	1.50	0.42	5.89
$4 \leq Z \leq 17$	1.14	4.08	0.25	1.50	0.68	7.23

Table 5.5: The average longitudinal velocities of isotropic and forward-peaked components for various ejectiles for 65 A MeV Ar + Ag.

In the upper panel of Figure 5.5 we have summed the average longitudinal momentum for each reaction, separated by ejectile type. The two unshaded

bars indicate the average longitudinal momentum of the heaviest fragment (HF) along with the average summed momenta for its associated isotropic ejectile components (IE). Shaded bars represent the average momenta for the forward-peaked components of type indicated. There is consistency between the arrows for the incident projectile momenta and the sums of the exit channel momenta. The fractional importance of the isotropic components is dominant for the lowest energies where complete and incomplete fusion dominate [Mo84, Vi89, Ha96] and the compound-nucleus model rules. However, for beam energies of $\gtrsim$ 44 A MeV, the forward-peaked components dominate, and the momentum is widely spread over many ejectile types. For this reason the term splintering central collisions was introduced in the Chapter 4. It is interesting that the linear momentum transfer to the heavy core nucleus (unshaded bars) decreases with energy more rapidly for the Cu than for Ag than for Au. One can say that the stopping power increases with target mass as is intuitively reasonable for these central collisions.

In the lower panels of Figure 5.5 the nuclear stopping is illustrated via longitudinal velocity ratios of $V_{\parallel}/V_{c.m.}$ for the heaviest fragments. From the high-multiplicity cut used (15%) one can estimate an average impact parameter of $\sim (1/4)b_{max}$ for the selected experimental events. The multiplicty cut was made on 15% of the detected events; the enabling condition (ball-2, see chapter 2) excluded $\sim$ 30% of the reactions. Thus we accept $\sim$ 10-12% of the reaction cross section. Experimental values are then compared to dynamical BUU model calculations for two limits on the impact parameters $b = 0$ and and $(1/3)b_{max}$. In these calculations the velocity of the core nuclear residual
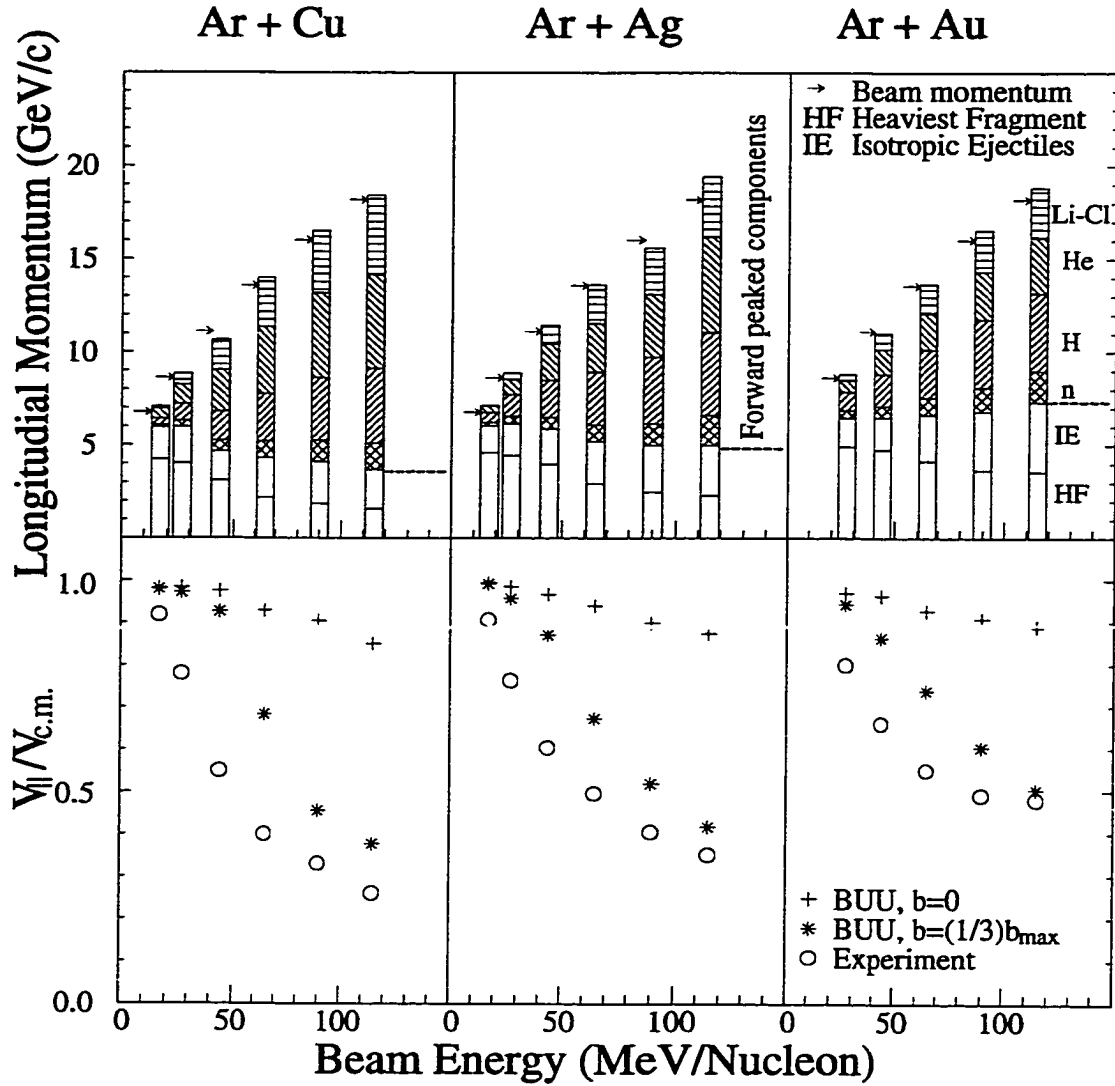
Figure 5.5: Upper panels: Average longitudinal momenta (laboratory) for the isotropic components (not hatched) and the forward-peaked components (hatched), for ejectiles as indicated. Lower panels: Average longitudinal velocity $V_{\parallel}/V_{c.m.}$ for the heaviest fragments. Data points and two model calculations are shown as indicated.

reaches an asymptotic value after $\sim 100\,fm/c$ [Da95], and this value is plotted. The calculated and experimental ratios all approach unity for 17 and 8 A MeV (not shown), but they have a completely different trend as the incident energy is increased. Clearly the nuclear stopping power for this energy domain is much stronger for the BUU model than that found in the experiments. Much of the discrepancy can be attributed to the forward-peaked ejectiles of A $\gtrsim$ 4, which are not addressed in the calculations. It is possible that the free nucleonic cross sections used in the model give an excessive amount of nuclear stopping or the semiclassical transport formulation may be inadequate at these energies due to the Uncertainty Principle.

5.4 Energy Removal by the Isotropic Emission Components

In this section, we examine the energy removed by the isotropic emission components. These components are generally termed as "post-thermalization" or "equilibrium emission". To obtain these values we have made a calorimetric sum of each ejectile's average multiplicity times its average separation and kinetic energies in the emitter frame. The average separation energies have been taken from averages over calculated statistical model decay chains [Aj96]. The average kinetic energies of H and He ejectiles are taken to be $E_0 + 2T$, using the fitting parameters of equation 5.1 in section 2. This takes care of the effect of energy thresholds. For Li and the IMF's, the energy values are averaged directly from the spectra in the emitter frame since the thresholds

are rather low; We classify the neutrons into the two groups. The first is taken to match the observed isotropic protons in both its multiplicity and its spectral slope; these we call "fast neutrons". The remainder of the neutron multiplicity is called "slow neutrons". The average energies of "fast" neutrons are estimated from the average proton energies with a correction for barrier energy. The average energies of "slow neutrons" are estimated by taking twice the spectral temperature from the He energy spectra. Table 5.6 and Table 5.7 list the average separation and kinetic energies of different ejectile types for the reaction of Ar + Ag.

Beam Energy	n	H	He	Li	$4 \leq Z \leq 18$
17 AMeV	8.82	5.61	0.65	12.64	1.16
27 AMeV	8.08	6.04	1.53	12.99	3.79
44 AMeV	8.35	7.37	3.33	15.14	8.54
65 AMeV	8.18	8.00	4.12	16.27	10.30
90 AMeV	8.16	7.65	4.30	17.37	11.04
115 AMeV	8.34	8.11	4.74	17.47	12.73

Table 5.6: Average separation energies (in units of MeV) of isotropic components of various ejectiles obtained from calculated statistical model decay chains for the reactions of Ar + Ag.

In Figure 5.6 we compare the average deposition energy estimated in two ways: (a) the total energy removal by isotropic components. (b) the deposition energies inferred from the average velocities of the heavest fragment [Co98a]. The latter values employed a simple one-dimensional approximation that is

Energy	Slow n	Fast n	H	He	Li	$4 \leq Z \leq 18$
17 AMeV	12	13	15.56	19.24	45.66	61.95
27 AMeV	14	15	16.97	22.70	46.11	63.57
44 AMeV	15	17	19.55	22.54	48.63	64.08
65 AMeV	18	24	26.55	26.02	50.89	66.35
90 AMeV	20	30	32.57	28.46	58.03	67.71
115 AMeV	20	30	31.84	28.30	58.08	68.23

Table 5.7: Average kinetic energy (in units of MeV) of isotropic components of various ejectiles of Ar + Ag.

weak in its details, but evidently not too bad for its average results. The two methods give very similar values of deposition energies. At the lowest incident energies, the ^{40}Ar projectile deposits the bulk of its energy via incomplete fusion with each target. As the energy is increased, the total energy deposited also increases to ~ 1 GeV for Cu compared to ~ 2 GeV for Au. This energy is more than the total binding energy, but contrary to many expectations it does not lead to disassembly of core nucleus into light particles and IMF's.

To examine in more detail the consistency of the energy balance, we show in Figure 5.7 the energy removal by the isotropic and forward peaked ejectiles as compared to total available energies. For each reaction, the main ejectiles for energy removal are the light particles n, H, He with IMF's playing a relatively minor role. For the lower energies of 17 and 27 A MeV, most of the available energy is deposited for isotropic emission, indicating essentially complete thermalization. However for 115 A MeV, only $\sim 1/4$ of total available
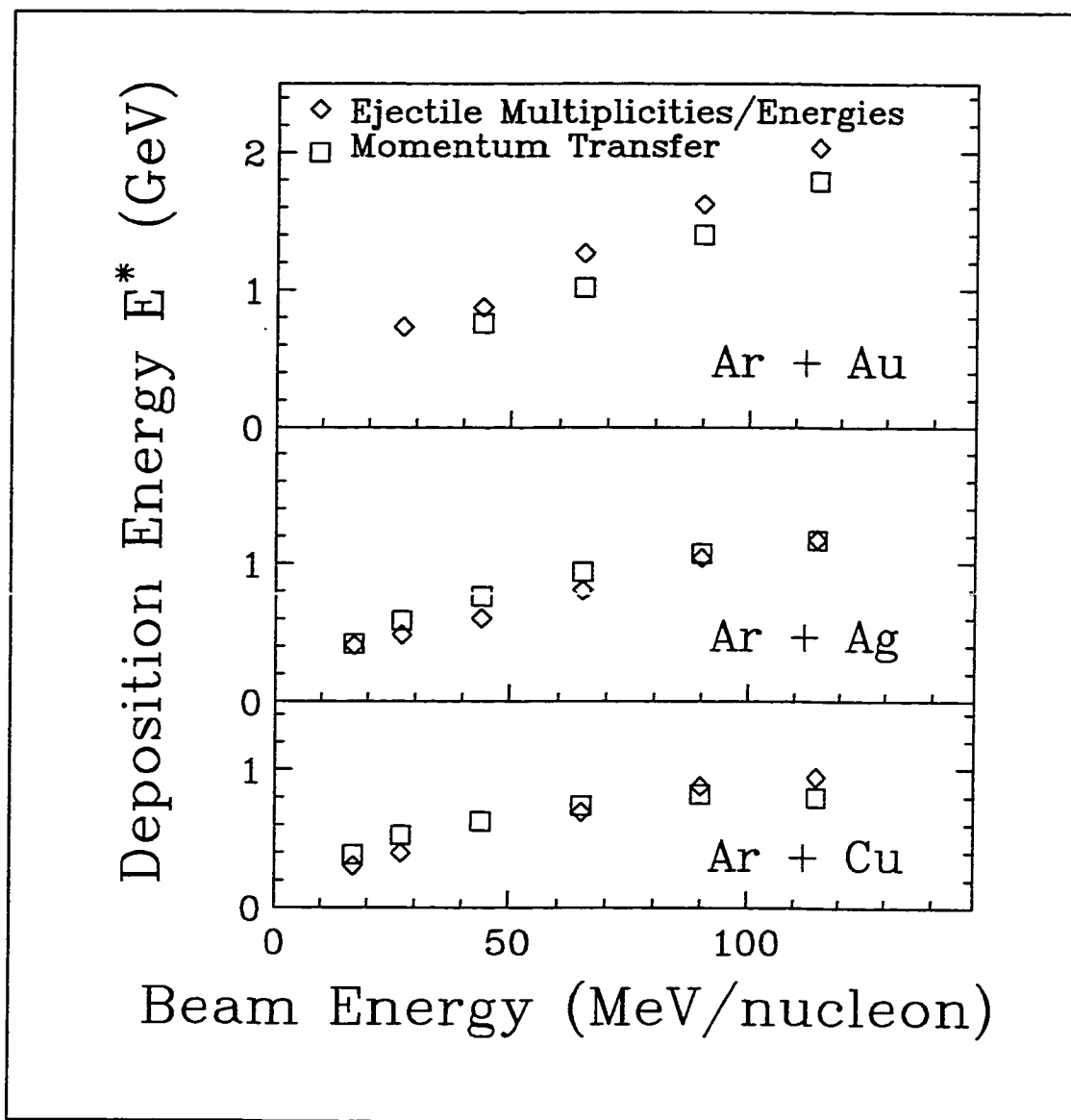
Figure 5.6: Comparison of total energy removal by isotropic emssion with the deposition energy calculated by use of the LMT.
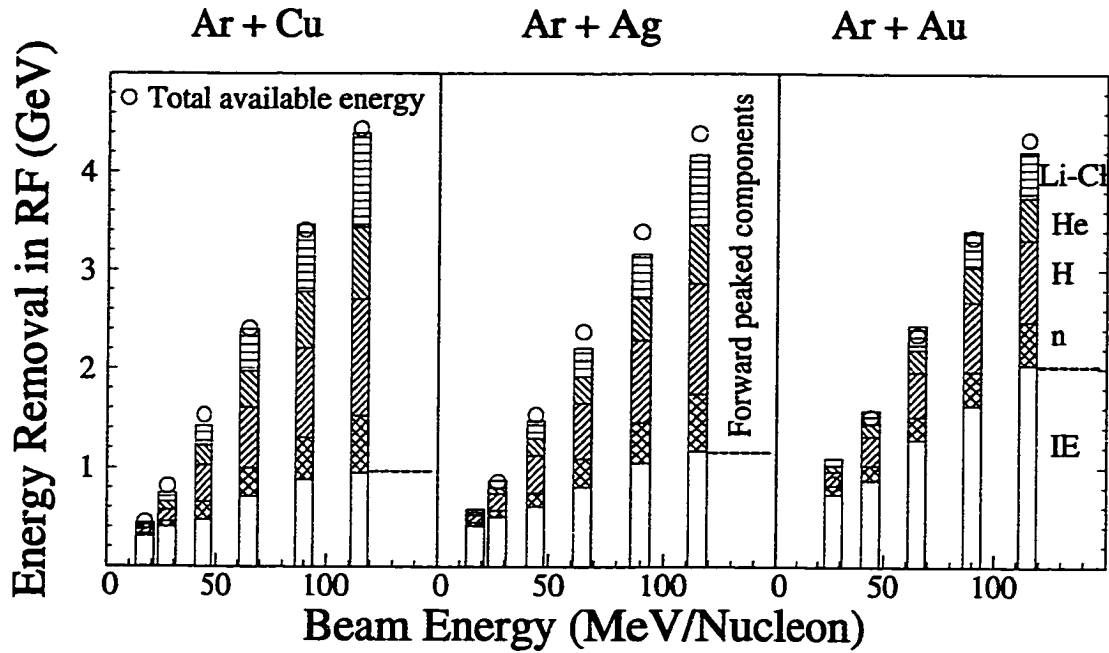
Figure 5.7: Energy removal (moving frame) by the isotropic and forward-peaked ejectiles.

energy is deposited for Ar + Cu and ~ 1/2 for Ar + Au and then converted into isotropic emission. This observation illustrates again the picture of splintering central collisions at high energies, i. e. a dominance of prethermalization breakup into a spray of forward-peaked light chunks.

5.5 The Spectral Slopes and Extra Thermal Energy

What can be said about energy thermalization, extra thermal energy and the possibility of collective radial flow at these very large excitation energies? In this section we will examine the spectral slopes (or kinetic temperatures) observed for $Z = 1$ and 2 particles at a lab angle of ~ 93°. The spectra were transformed into the system of average heaviest residual fragment and are well

fit by a Maxwell form $P(E) \propto (E - V)exp(-E/s)$. Figure 5.8 shows smooth curve fits to the experimental spectra for the reactions of Ar + Ag. The same fitting precedure has also been used for calculations from the statistical model [Aj96] with initial excitation energies from Figure 5.6. Values of the barrier parameters were taken from systematics, and the best-fit values of s are shown in Figure 5.9. The solid points give experimental data, and the open points result from a statistical model [Aj96] calculation. The relation of the initial temperature to the value of s can be expressed as $T = f \times s$ where $f \approx 1.0$ for He and ≈ 1.2 for H [Ch97].

For He emission there is close agreement between calculated and observed values of s. We conclude that the He emission comes from extensively termalized sourses. By contrast the H emission carries significantly more than just thermal energy for $\gtrsim$ 44 A MeV. In addition the excitation energy dependence of these spectral temperatures for He gives no clear indication of an S shape that has been cited as evidence for a phase transition [Du97, Ha97].

For H emission the observed spectral slopes grow much more rapidly with energy than do the calculated values. From arguments described in e.g. [La98], one could attribute this divergence or extra thermal energy to an increasing importance for radial flow with increase deposition energy. This would require an average radial flow velocity of $\sim 0.1c$ for ^{1}H from 115 A MeV ^{40}Ar reactions. In this view the collective radial flow is mainly carried away by the H emission, and seems to be considerably damped out before most of the He emission occurs.
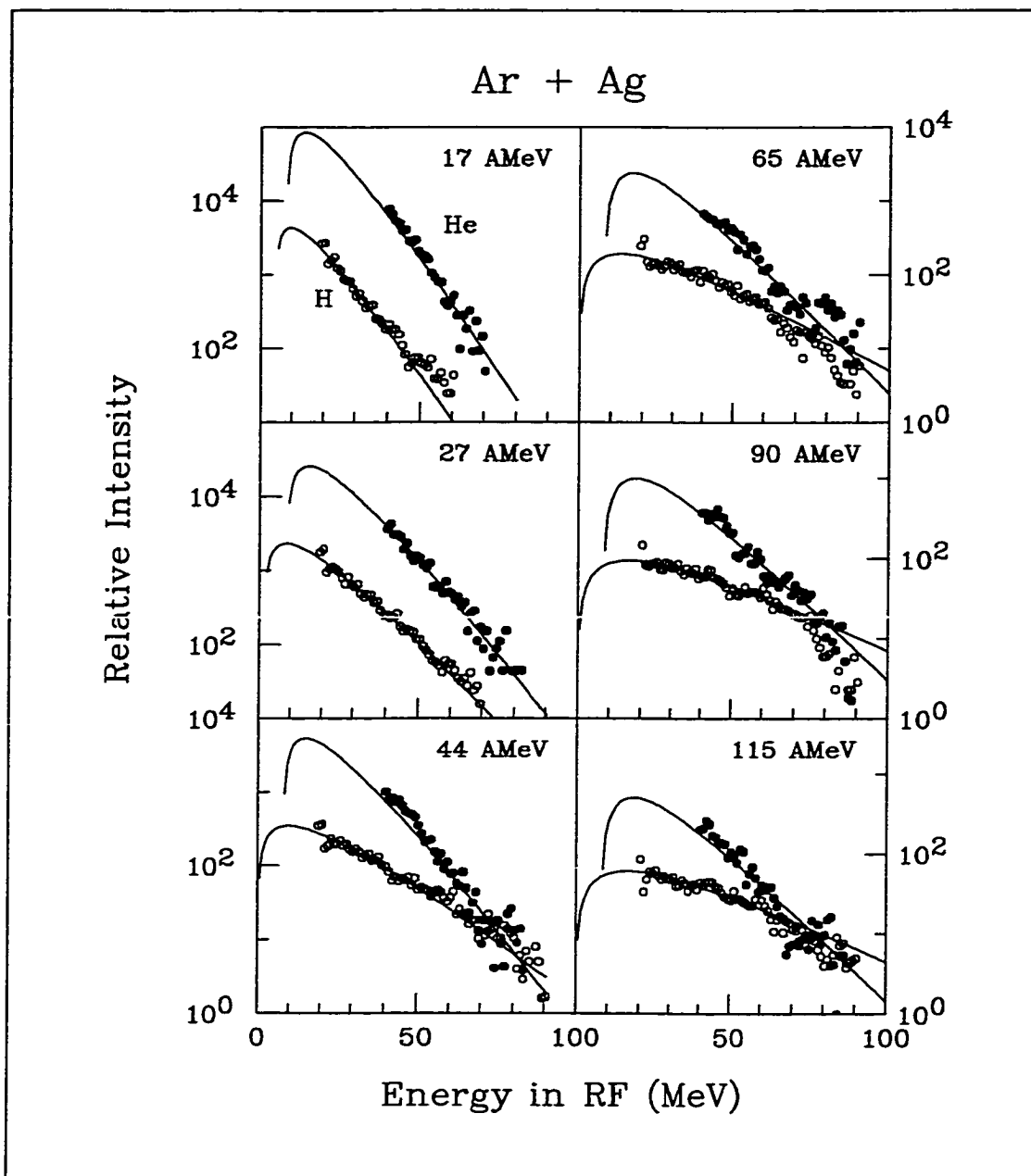
Figure 5.8: Energy spectra of ejectiles in the HF frame for Ar+Ag reactions, the solid lines are fits to a Maxwell form $P(E) \propto (E - V)exp(-E/s)$.
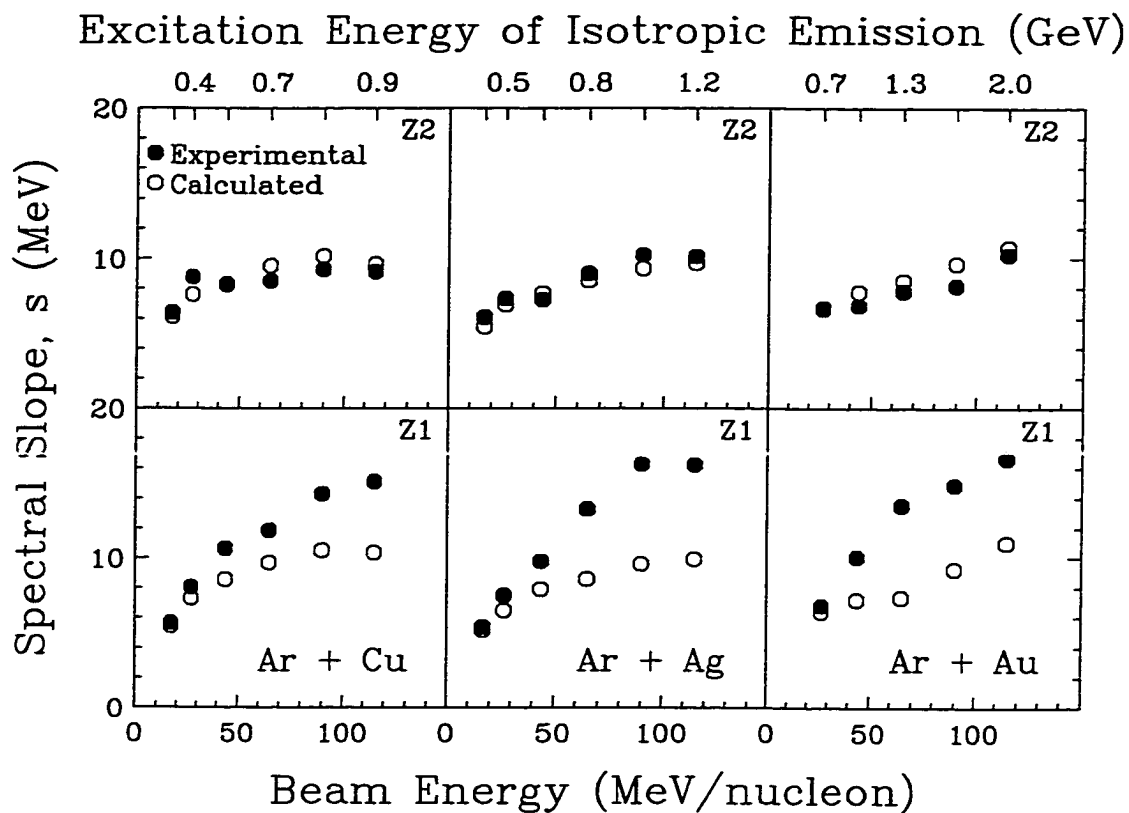
Figure 5.9: The spectral slope or kinetic temperature of H and He for Ar+Cu, Ag and Au reactions. Solid circles show the experimental results and empty circles show statistical model (Modgan) calculations.

5.6 Summary

The nuclear stopping or momentum deposition has been characterized for ^{40}Ar + Cu, Ag, Au. For $\sim 40 - 100$ A MeV the stopping is much smaller than predicitions of the BUU model. Nevertheless, core nuclear excitations of ~ 1-2 GeV are achieved for 115 A MeV ^{40}Ar as determined by calorimetric reconstruction of the isotropic emission ensembles. These large energy depositions do not generally lead to complete nuclear disassembly as is often expected. Significant extra thermal energy (conceivably collective radial flow) is found in the Z=1 ejectiles, but much less than that found elsewhere for the reaction 1 A GeV Au + ^{12}C[La98]. It seems that even the isotropic emission components are significantly affected by entrance channel dynamics, which challenges the simple notion of equilibration.

Chapter 6

Directed Transverse Flow

6.1 Introduction

The study of collective motion in heavy ion collisions can provide information about the equation of state of nuclear matter, one of major goals of nuclear physics [St86, Gu89, Ga90, Pa93]. The presence of collective motion can be inferred from the distribution of products with respect to the entrance channel reaction plane using observables such as the in-plane transverse momentum and the azimuthal angular distributions. The term "flow" was introduced since the transverse collective motion was interpreted as a hydrodynmical side-splash due to the compression of nuclear matter [St80, Gu89]. Recent studies indicate that collective transverse flow in the reaction plane disappears at an incident energy, termed the "balance energy "[Pa97a, Og90]. The balance energy represents the point where the attractive scattering, dominant at energies around 10 MeV/nucleon, balances the repulsive interactions dominant at energies around 400 MeV/nucleon [Mo85, Be87]. Our experiment with

a broad bombarding energy range and different projectile-target combinations give us an opportunity to study the dependence of the directed transverse flow on mass asymmetry in the entrance channel.

What kind of role do the size of the target nucleus and the asymmetry of the reaction system play in the determination of the directed transverse flow? As two nuclei collide, the pressure and density increase in the interaction region, i.e., compression of the nuclear matter occurs in the participant volume. The transverse flow of nuclear matter occurs in the direction of the lowest pressure, which is affected by the masses of participant nuclei. In this chapter we present results on the evolution of transverse flow from 27 AMeV to 115 AMeV for the reaction systems of Ar + Cu, Ag and Au. Results for the rotational flow are given in Appendix D.

6.2 Reaction plane determination

The term "flow" is used to describe preferences in the momentum distribution of ejectiles with respect to the reaction plane. The determination of the reaction plane is a first and most important step to study the collective flow. The reaction plane is defined geometrically by the set of momentum vectors between center of the projectile and the target. The impact parameter b, which joins the center of the projectile and target at their distance of closest approach, also lies within this plane. These geometrical relationships are shown schematically in Figure 6.1.

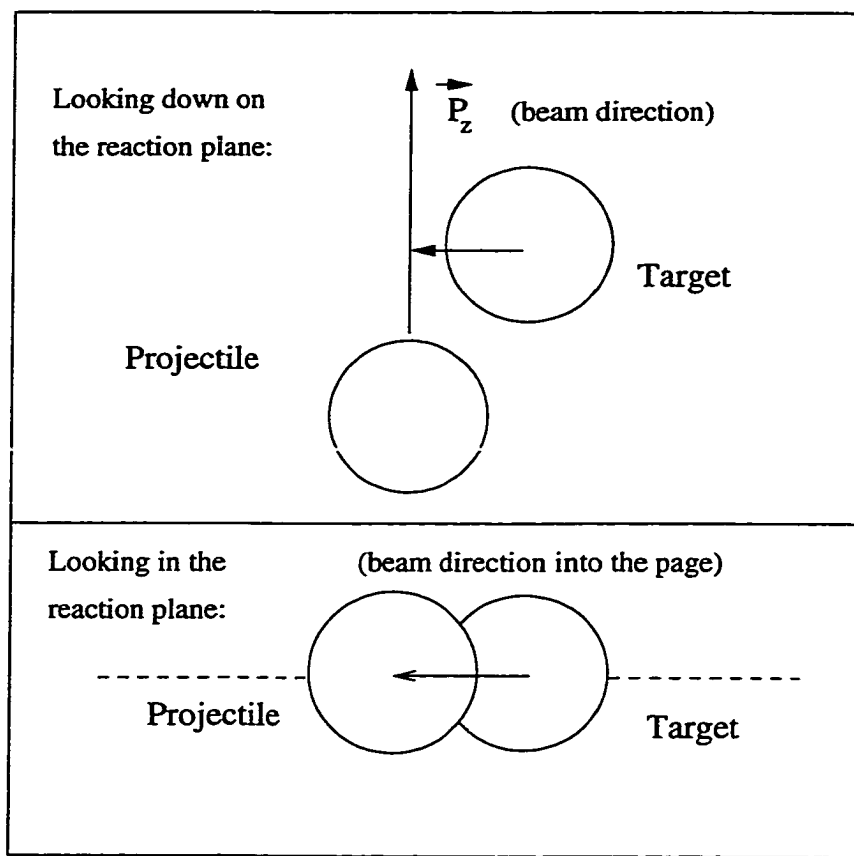Various methods have been developed to reconstruct the reaction plane

Figure 6.1: A geometrical description of the reaction plane.

on an event-by-event basis from the measured distribution of light fragments produced in heavy-ion collisons. The commonly used techniques used for reaction plane determination include the sphericity tensor method[Cu82, Gy82], and transverse momentum analysis[Da85] for reactions with beam energy from 100MeV/nucleon to more than 1 GeV/nucleon, and azimuthal correlation techniques[Wi92, Pa96] used for relatively lower energy reactions of several tens of MeV/nucleon.

In the sphericity tensor method, the shape of event in momentum space is determined by diagonalizing the flow tensor F_{ij}:

$$F_{ij} = \sum_{v=1}^{N} w_\mu p_i(\mu) p_j, \qquad (6.1)$$

where N is the number of particles in an event, p_i are the Cartesian components of the momentum of particle μ, and w_μ is a weighting factor associated with that particle, typically $1/2m_\mu$. The reaction plane is taken as the plane defined by the beam axis and major axis of the resulting flow ellipsoid.

In the transverse momentum analysis, a vector $\mathbf{Q}$ is constructed from the transverse momenta of the particles in an event:

$$bfQ = \sum_{v=1}^{N} w_\mu bf P_\mu^\perp, \qquad (6.2)$$

where the weight w_μ is chosen to be positive for particles emitted in the forward hemisphere (c.m.) and negative for particles emitted in the backward hemisphere (c.m.). The reaction plane is defined by the beam axis and $\mathbf{Q}$. The absolute value of w_μ is chosen to provide the maximum sensitivity to the reaction plane. In practice this is usually achieved by randomly dividing

events into two subevents, calculating $\mathbf{Q}$ for each subevent, and selecting w_μ to minimize the difference between the resulting reaction planes.

The azimuthal correlation technique is based on the notion that particle emission is enhanced in the reaction plane[Ts84]. Thus this technique involves finding the plane that generates the largest in-plane enhancement. First a particle of interest (POI) is chosen from the event. A recoil correction or boost is then applied to all the particles given by:

$$\mathbf{V}^\perp_{boost} = \frac{\mathbf{P}^\perp_{POI}}{m_{sys} - m_{POI}},$$ (6.3)

where m_{sys} is the sum of the target and projectile masses, the $\mathbf{P}^\perp_{POI}$ and m_{POI} are the transverse momentum and mass respectively of the particle of interest. In practice, the c.m. momenta of the remaining particles in the event are projected into a plane $(p^x - p^y)$ perpendicular to the beam axis. The slope of the projection line of the reaction plane is determined by minmizing the deviation of distances of all momentum vectors to the projection line. This process maximizes the in-plane enhancement. This method exploits the correlation between azimuthal angle of the reaction plane and azimuthal angles of the particles produced in the collision.

A simple method to determine the reaction plane was used for this experiment; we use the summed momentum vectors of the projectile like fragments (PLF) as the reaction plane. Because the initial momentum vector of the projectile lies in the true reaction plane, it is reasonable to use the sum of exit channel of PLFs to trace back to the original momentum vector. The selection conditions for these PLFs are $A > 8$, $\theta < 60deg.$ and $V/V_{RF} > 2.5$.

Then we use the azimuthal angle of the vector sum as the azimuthal angle of the reaction plane.

6.3 Azimuthal correlations and the flow analysis

As momentioned in the above section we study the transverse flow by using azimuthal correlation functions, which can remove distortions due to the acceptance effects. In this section, we present results for the reactions of Ar+Cu, Ar+Ag, and Ar+Au from 27 MeV/nucleon to 115 MeV/nucleon.

In general, the probability of particle emission at an azimuthal angle measured with respect to the reaction plane can be written in the form of a Fourier series[Po98].

$$E\frac{d^3N}{d^3p} = \frac{1}{2\pi}\frac{d^2N}{p_t dp_t dy}(1 + \sum_{n=1}^{\infty} 2v_n \cos(n(\phi - \Phi_r))),\qquad(6.4)$$

where Φ_r denotes the reaction plane angle, and the sine terms are omitted due to the reflection sysmmetry with respect to the reaction plane. The coefficient v_1 can be thought of as $< p_x/p_t >$ and v_2 as $< (p_x/p_t)^2 - (p_y/p_t)^2 >$. The coefficients v_n can be evaluated by $< cos(n(\phi - \Phi_r)) >$. Figure 6.2 shows a typical correlation function for He ejectiles vs the reaction plane, measured by multi-PLFs. This function is the ratio of the true azimuthal distribution $R(\Delta\Phi)$ to a "fake" azimuthal distribution $F(\Delta\Phi)$:

$$C(\Delta\Phi) = \frac{R(\Delta\Phi)}{F(\Delta\Phi)}\qquad(6.5).$$

The fake distribution is constructed by using mixed events. In Figure 6.2, circles give the results for 44 MeV/nucleon Ar+Ag. The solid line shows the
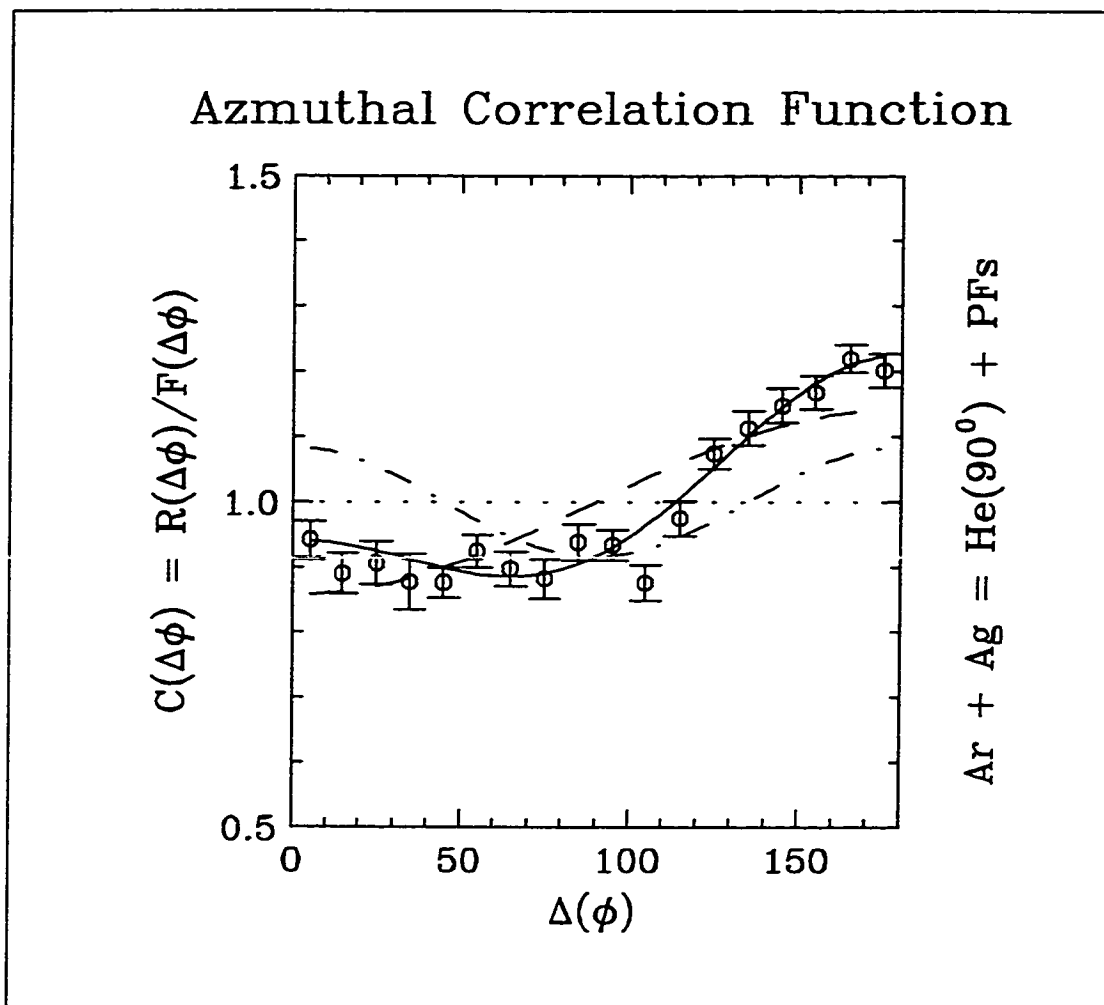
Azmuthal Correlation Function

Figure 6.2: The azimuthal correlation function and its fit by a Fourier expansion for 44 AMeV Ar+Ag, circles are the data points and solid line is the fit by Fourier expansion.

representation by equation of (6.4) with the first two terms of a Fourier series, the dashed line shows the representation by equation of (6.4) with only the first term of a Fourier series, and the dot-dashed line shows the representation by equation of (6.4) with only the second term of a Fourier series. The preferential emission at $\phi = 180^0$ compared to at $\phi = 0^0$ is due to the transverse momentum which is described by the first term of equation (6.4). The in-plane preferential emission exhibits a peaking at both $\phi = 180^0$ and $\phi = 0^0$ with a valley at $\phi = 90^0$, due to nuclear rotation or (angular momentum); it can be termed "rotational flow".

Azimuthal correlation functions for H, He and IMFs from our ^{40}Ar + Cu, Ag and Au reactions (27 to 115 MeV/nucleon) have been studied sysmatically with different rapidity gates. Figure 6.3 shows the rapidity distribution of He in the reaction of 44 MeV/nucleon Ar+Ag; vertical dots show how the rapidity distribution was gated for the azimuthal correlation functions to be shown below. The rapidity is defined by

$$Y = y_{c.m}/y_{c.m.}^{proj} = (y/y_{proj})_{c.m.} \qquad and$$

$$y_{c.m} = y_{lab} - y_{c.m}, \qquad y_{lab} = 0.5 * ln\frac{1 + v_{//}/c}{1 - v_{//}/c}. \qquad (6.6)$$

Where $v_{//}$ is longitudial velocity of the particle. This definition is applied for the whole chapter.

Figure 6.4 shows azimuthal correlation functions for He. The results were selected from events with the highest 15% of the multiplicity. The columns of 30 panels correspond to rapidity gates shown in Figure 6.3. The rows of these panel correspond to bombarding energies, from 27 to 115 MeV/nucleon,
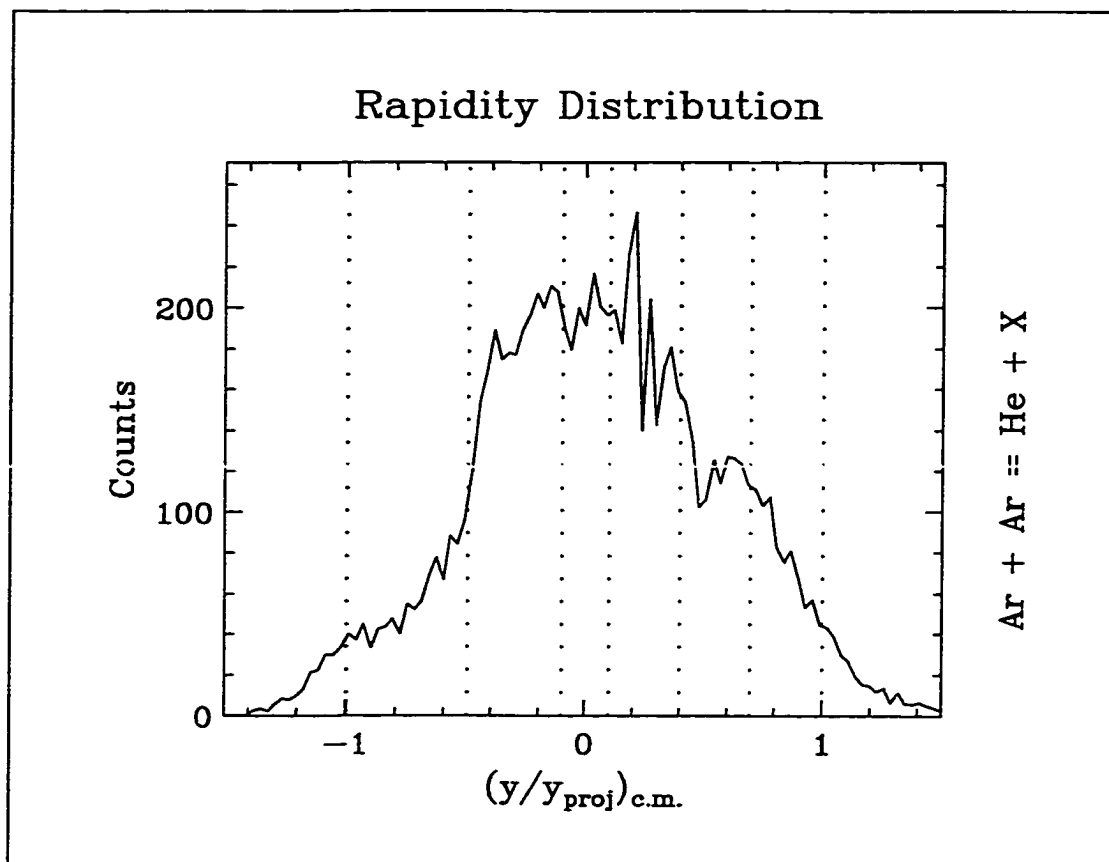
Figure 6.3: The rapidity distribution of He for 44 AMeV Ar+Ag reactions, the dotted line shows the cuts for azimuthal correlation functions.

respectively, from top to bottom. These results exhibit a general picture of the evolution of the transverse momentum. Particles in the low rapidity gates (backward angles in the c.m.), are dominated by the particles emitted from a "cooler" source; they peak at 180 in the azimuthal correlation functions. On the other hand, particles in the high rapidity gates (forward angles in the c.m.), are dominated by the particles emitted from a "hotter" collision zone; they peak at 0^0 in the azimuthal correlation functions. The general trend with increasing energy is that the flow becomes weaker as energy increases.

In Figure 6.5, we display the azimuthal correlation functions for He in Ar+Ag reactions for the mid range of multiplicity, i.e. from about the 15% lowest multiplicity to 15% highest multiplicity. Compared to Figure 6.4 for the high multiplicity cut, it seems that more central collisions exhibit stronger flow. Possibly the more central collisions produce stronger initial attraction and/or higher presures which drive the resultant ejectile flow. More azimuthal correlation functions for other ejectiles and other systems are given in appendix C.

From the azimuthal correlation functions, the $< cos\Delta\Phi >$ can be extracted for different rapidity cuts. Results for various particles from Ar + Cu, Ag and Au are shown in Figure 6.6, 6.7 and 6.8, respectively. Although our rapidity cuts are not densely covered, for each of the particle types the data exhibit the characteristic "S-shape" associated with the directed transverse flow, demonstrating dynamical momentum transfer on opposite sides of the reaction plane. The directed transverse flow generally increases as the fragment mass increases for each incident beam energy, because for the larger fragment, the
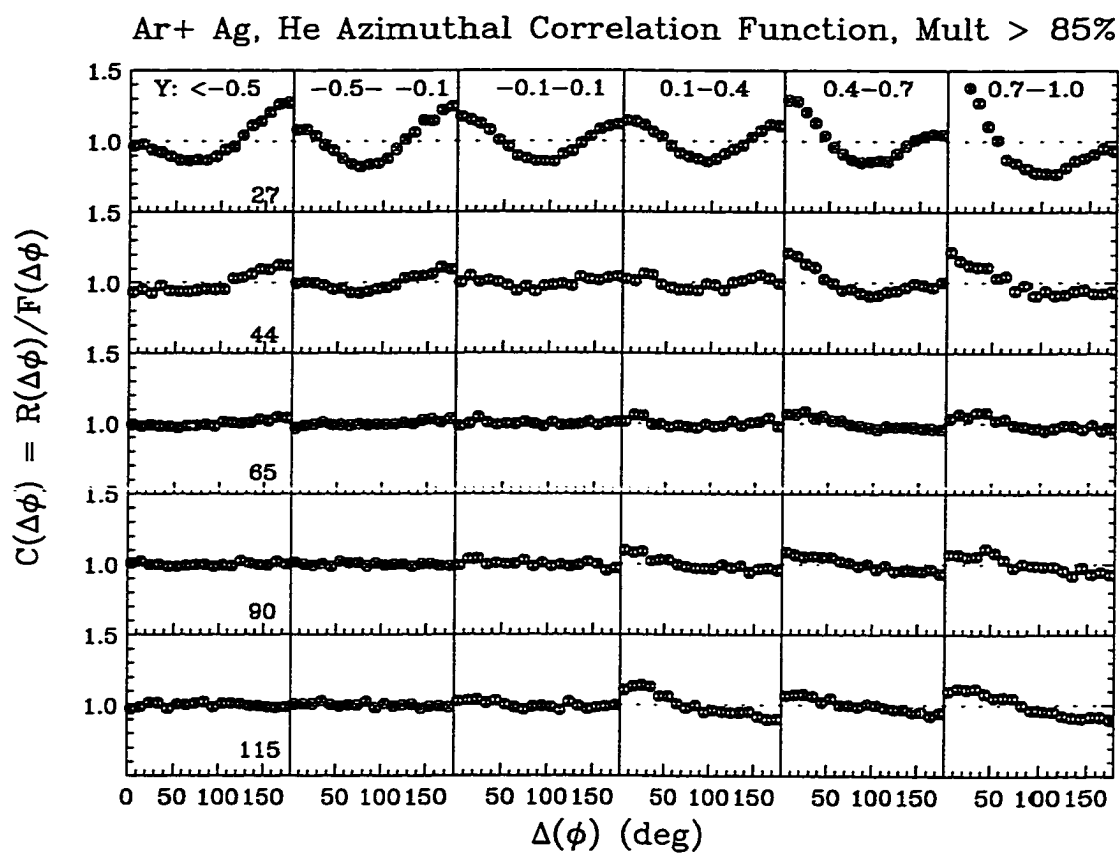
Figure 6.4: Azimuthal correlation functions of He for Ar+Ag reactions, the columns represent different rapidity cuts, the rows represent different beam energies.
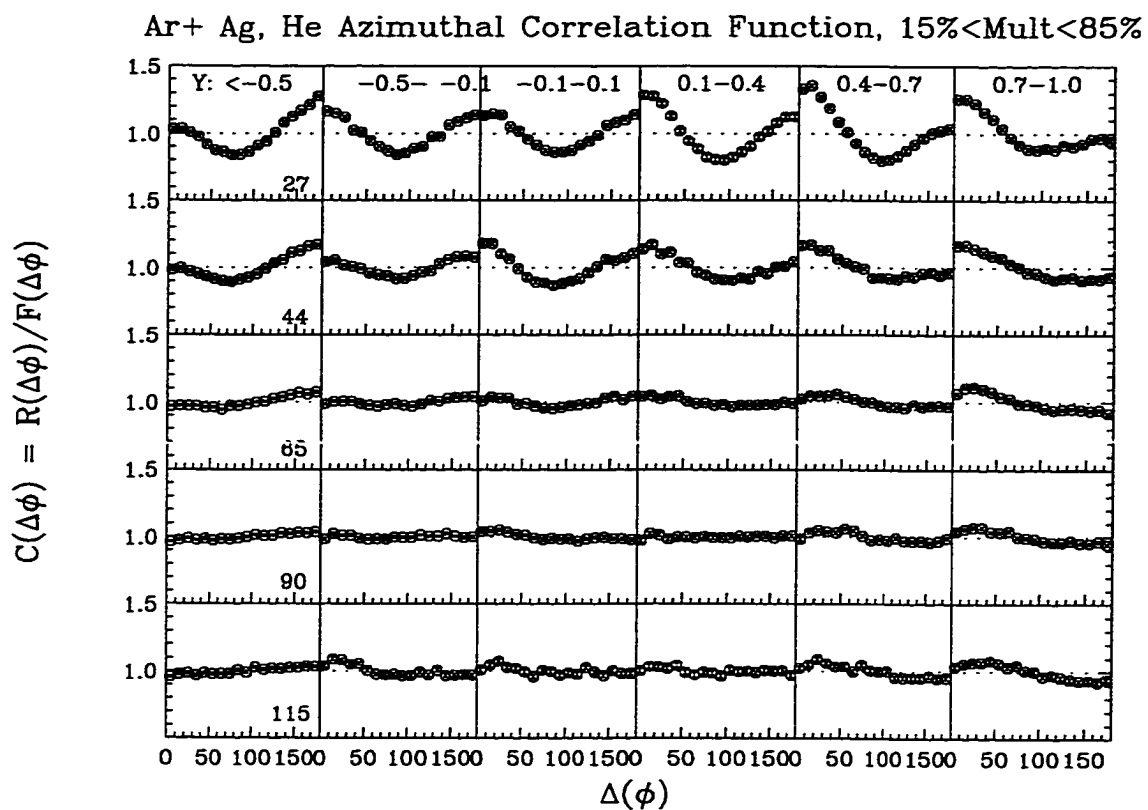
Figure 6.5: Azimuthal correlation functions of He for Ar+Ag reactions, with multiplicity cuts from 15% to 85%.

flow energy is an increasingly larger fraction of the fragment energy while the thermal energy is less important [Do87], This is under the assumption that the thermal energy was equally partitioned for an equilibrated system of nucleons and fragments at fixed freezeout temperature. Comparing these figures, we can see that the larger targets produce weaker flow at lower energies. Possibly the repulsive pressure is becomes larger compared to nuclear attraction as target mass is increased.

In these figures, the solid lines show linear fits in the region of $0.0 \leq (y/y_{proj})_{c.m.} < 1.0$. The slope of the fitted line represents the reduced flow which is $d < cos\phi > /dY$. For these results, the data for He has the best combination of statistical and systematic errors. In upper panels of Figure 6.9, extracted values of the reduced transverse flow for He particles are plotted versus the beam energy for Ar + Cu, Ag and Au collisions with high multiplicity cut (>85%). The errors shown are only the statistical errors. The curves of reduced transverse flow for reactions of Ar+Au and Ar+ Ag pass through minima which are generally thought to correspond to a change from attractive (negative) flow to repulsive (positive) flow. For the lower panels in Figure 6.9, we have therefore changed the sign of the values of those points after the bend in the trend line. Then the data follow a line passing through zero from which we can extract the balance energies. The values of balance energies for reactions of Ar+Au, Ar+Ag and Ar+Cu are $\sim$ 65 MeV/nucleon, $\sim$ 85 MeV/nucleon and $\sim$ 105 MeV/nucleon respectively. These results indicate that the balance energy for different reaction systems decreases as the target mass increases.
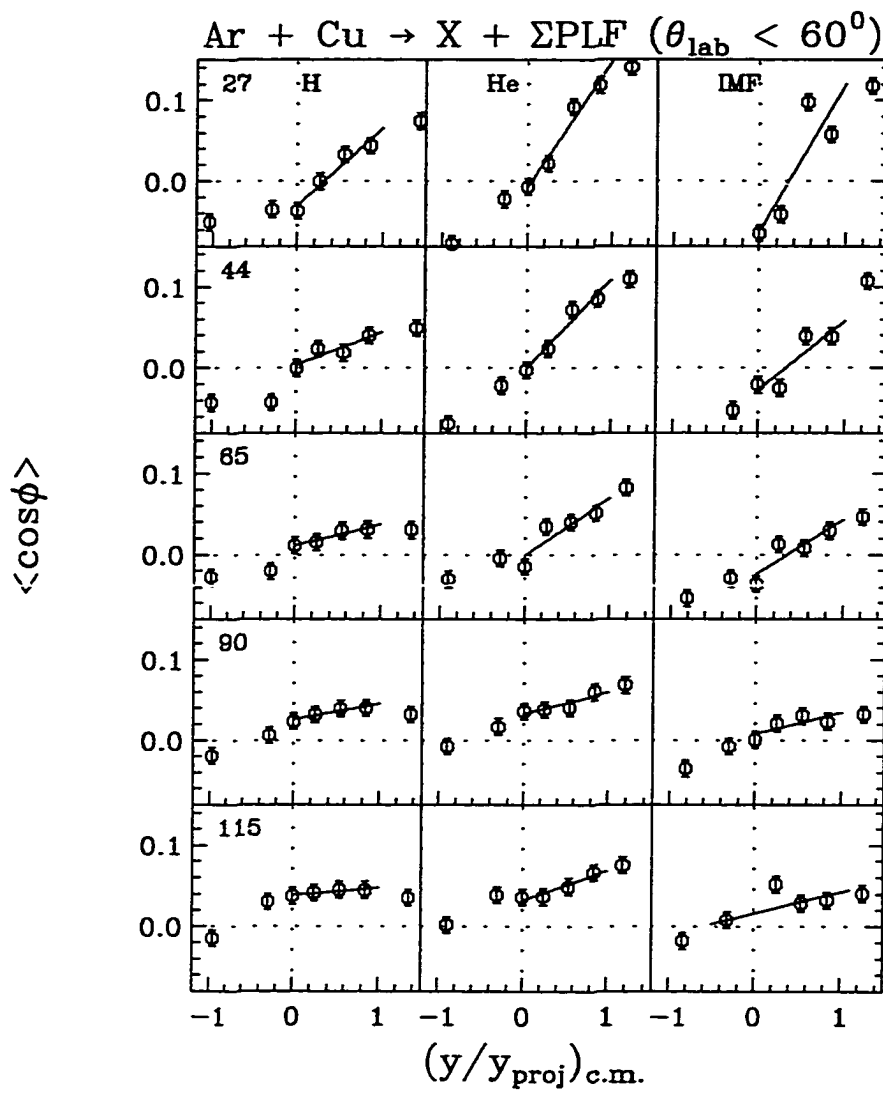
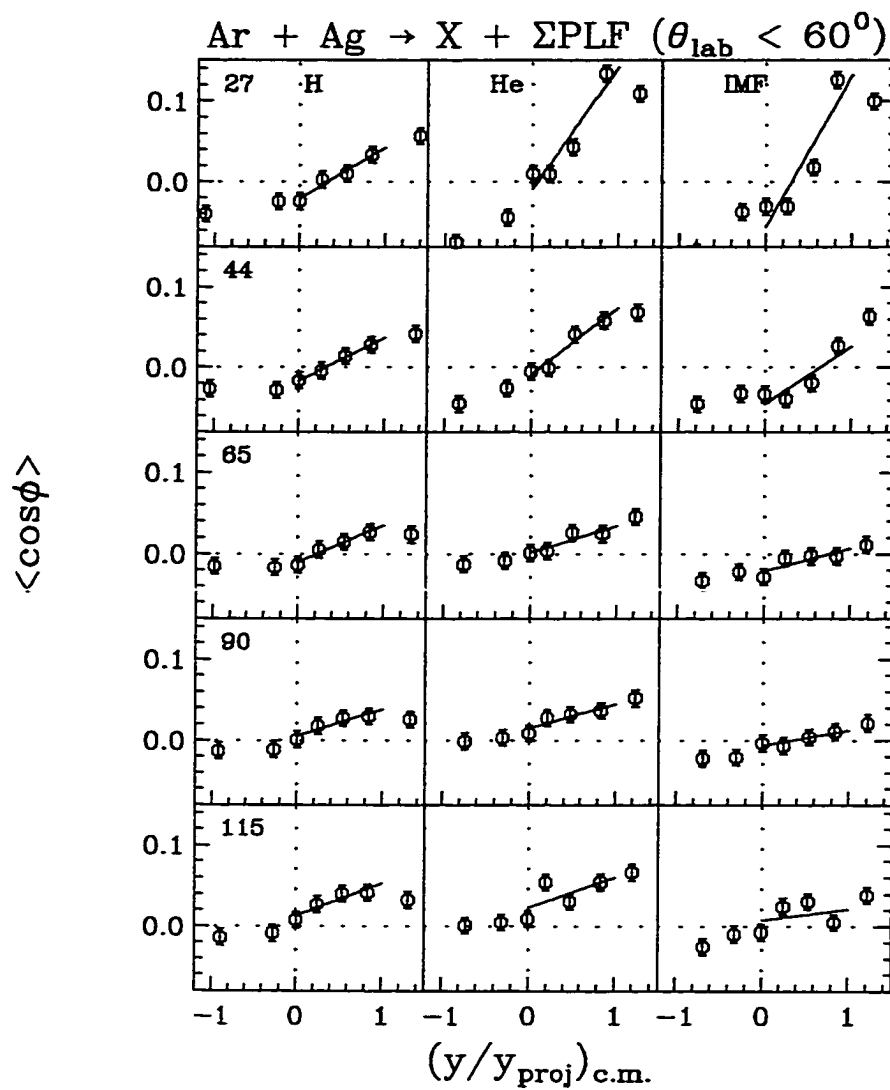Figure 6.6: The average cosine $< cos\phi >$ of H, He and IMF for Ar+Cu reactions.

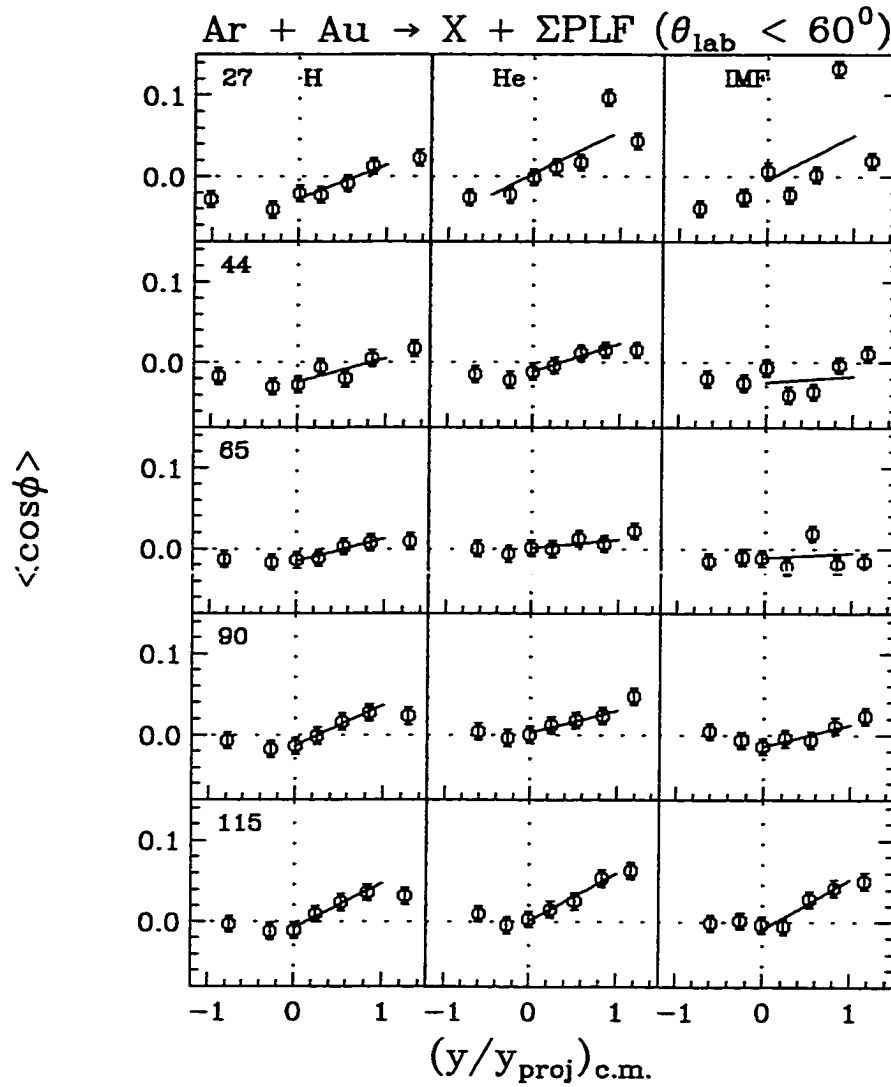Figure 6.7: The average cosine $< cos\phi >$ of H, He and IMF for Ar+Ag reactions.

Figure 6.8: The average cosine $< cos\phi >$ of H, He and IMF for Ar+Au reactions.

We conclude that the more massive the target the stronger the relative strength of the compressional repulsion and hence the lower the energy of transition from attractive to repulsive scattering.
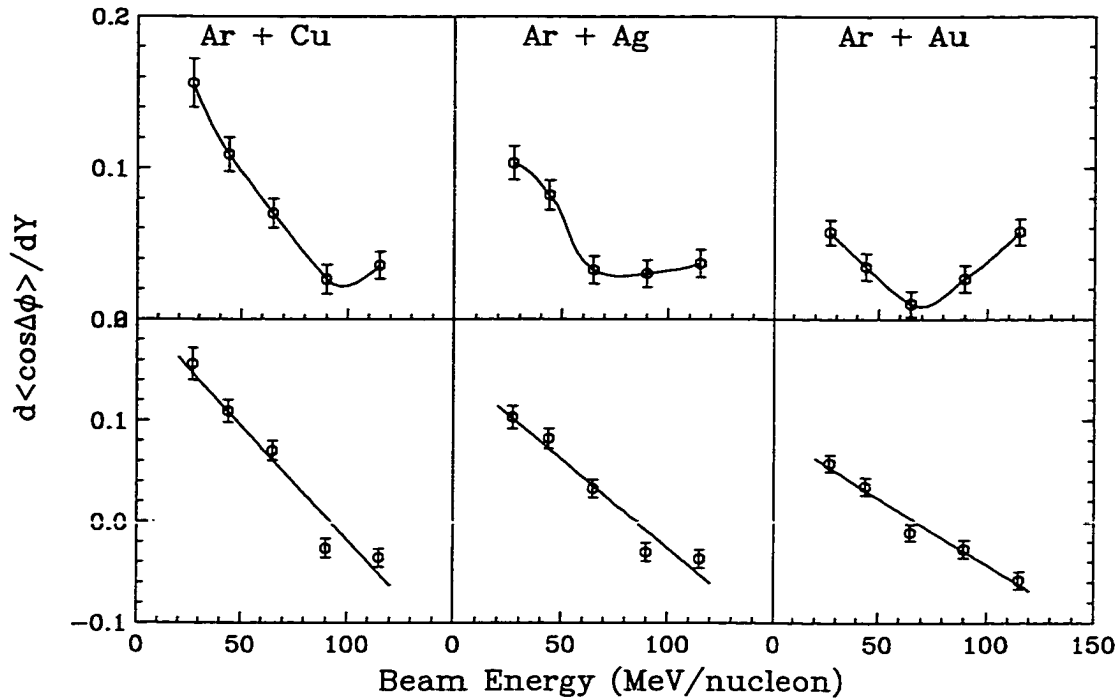

Figure 6.9: The evolution of reduced transverse flow of He particles for Ar + Cu, Ag and Au.

6.4 Summary

The directed or transverse flow has been examined using azmuthal correlation functions for H, He and IMF particles for ^{40}Ar + Cu, Ag and Au. For each system, particles with larger mass exhibit stronger transverse flow. For each ejectile type, as the beam energy increases, the transverse flow decreases

in the lower energy region and then increases again after a minimum (or trend line bend) which indicates an approach to the balance energy. Cu reactions have a stronger transverse flow at low energy and larger balance energy than Ag reactions than Au reactions

Chapter 7

Multifragmentation: Evolution of Decay Modes

7.1 Introduction

Multifragmentation is characterized by the multiple production of nuclear fragments with intermediate mass. It is expected to be the dominant decay mode of heavy nuclear systems with excition energies in the vicinity of their binding energies. The study of multifragmentation can contribute to our understanding of nuclear dynamics and the properties of nuclear matter at high temperature. Of special interest is the possibility of identifying signatures of a liquid-gas phase transition.

In chapter 5, our calorimetric reconstruction results show that core nuclear excitations of $\sim$ 1-2 GeV are achieved for 115 A MeV reactions; these values exceed the total binding energies and are expected to lead to multifragmention. It is interesting to compare these new experimental data with calculations from multifragmention models. In this chapter, we present such comparisons with

calculations from the SMM (or the Copenhagen) model [Bo85a, Bo85b, Ba87] and also from the Berlin model [Gr86, Zh87, Gr90]. In section 2, the mass distributions are compared with these calculations to show the conditions for which the heavy residual fragments disappear. In section 3, the average masses of the heaviest fragments are compared with calculated values to give a general picture of disassembly of hot nuclei. In addition, the decay modes are studied by comparing multiplicities of intermediate mass fragments (Z < 3) and light-charged-particles (Z=1 and 2).

7.2 Disappearance of Heavy Fragments

Our study of the isotropic emission components shows that the most central collisions can produce hot nuclei with excitations higher than their binding energies. Listed in Table 7.1, for example, are these energies for reactions of 115 A MeV Ar + Ag. For such high excitation energy, can heavy residual fragments can still exist? In this section, we compare the mass distributions from the experimental data to simulations from multifragmention models.

Figure 7.1 compares these mass distributions for 65 and 115 A MeV Ar + Ag reactions. In the top panels, the data are gated the by highest 15% of multiplicities while the lower panels are for the highest 1%. Simulations were calculated with excitation energies of 808 and 1173 MeV for 65 and 115 A MeV, respectively, as extracted from experimental data. At 65 A MeV, the data exhibit a plateau and a broad tail of heavy residuals with mass from ∼ 40 to 100, the simulations from both SMM and Berlin models terminate at

Energy	E^*	Isotropic mass	E^*/A
17 AMeV	408.8	140.1	2.92
27 AMeV	485.6	134.1	3.62
44 AMeV	601.5	123.1	4.89
65 AMeV	808.1	116.9	6.91
90 AMeV	1043.7	114.0	9.16
115 AMeV	1172.5	114.5	10.24

Table 7.1: Average excitation energies for reactions for the reactions of Ar + Ag.

a mass of $\sim$ 50. The data clearly indicate that heavier targetlike fragments still exist even for such high initial excitation energies; the simulations predict more disassembly or breakup of the hot nuclei into middle sized pieces. This is also illustrated by the higher calculated yields of fragments in mass region of $\sim$ 15 to 40.

For 115 A MeV ^{40}Ar + Ag, the qualitative pattern is very similiar; the data have a broad tail of heavy residual masses while the models predict more complete disassembly into even smaller fragments.

Next we narrow the data selection to even more violent collisions with a gate on the highest 1% of multiplicities as displayed in the lower panels. Here we expect the data to show the most complete disassembly. At 115 A MeV, the heavy residual nuclei do indeed disappear, and the simulations fit the mass distribution very well if we use 1300 MeV for the excitation energy. This value is 10% higher than that obtained for the 15% high multiplicity gate, but is

much less than the total available energy of $\sim$ 4000 MeV. For 65 A MeV, there is still a tail of heavy residual fragments, but the simulations can be said to fit the data better for the low mass region. Again we have used an excitation energy only 10% higher than that for the 15% high multiplicity gate. The true deposition energies for the 1% multiplicity cut may well be much greater as discussed below. This could lead to complete vaporization for the model calculations also in sharp contrast to the experimental result.
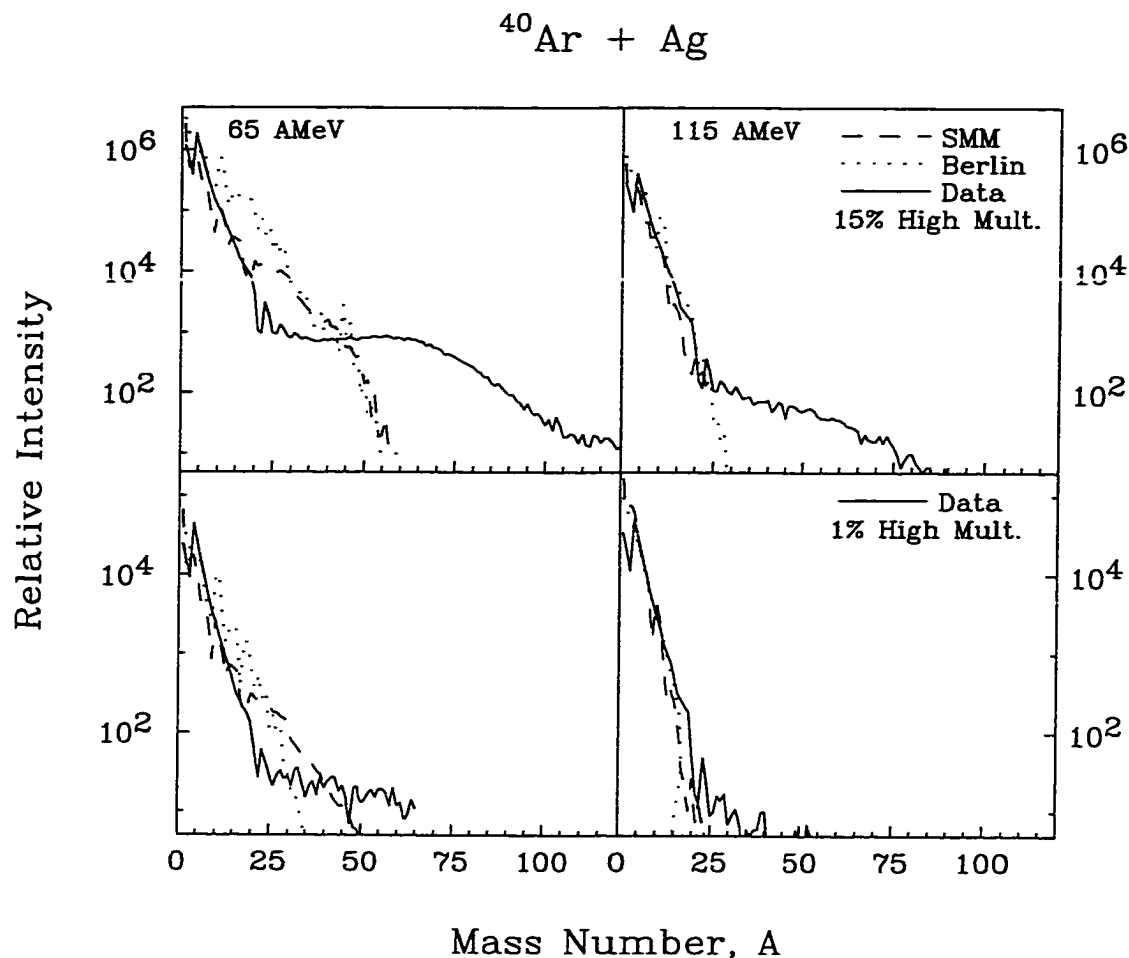
$$^{40}Ar + Ag$$

Figure 7.1: Comparison of mass distributions with multifragmentation models for $^{40}Ar + Ag$.

115 A MeV Ar + Ag
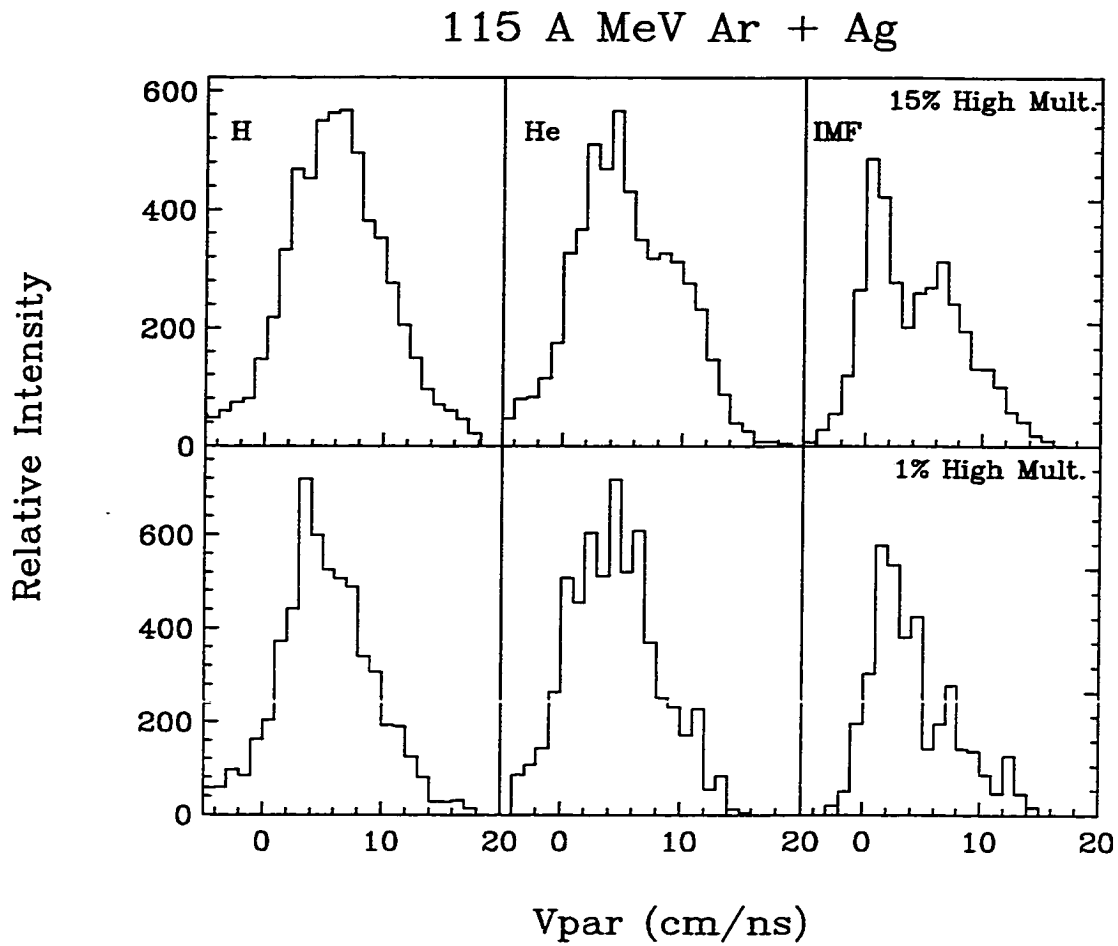

Figure 7.2: Distributions of the longitudinal velocity of H, He and IMFs for 115 AMeV Ar + Ag.

Ideally, we can extract excitation energies for all the reactions with 1% highest multiplicity gates using the same procedure described in chapter 5 for 15% highest multiplicity gates. However, we do not have sufficient statistics. Nevertheless, we can get some rough estimations from the emmision pattern of ejectiles.

In Figure 7.2, we compare distributions of the longitudinal velocity $(V_{//})$ for H, He and IMFs for 115 AMeV Ar + Ag with 15% highest multiplicity gate and 1% highest multiplicity gate. As decribed in chapter 5, for 15% highest multiplicity gate (top panels), all the velocity distributions of H, He and IMFs can be separated as isotropic components and forward-peaked components in the moving frame of the heaviest fragment with velocity of $\sim 1.5 cm/ns$. The isotropic components with a peak at $\sim 1.5 cm/ns$ in their velocity distributions are evaparated from the heaviest fragment. The forward-peaked components with a peak at velocity larger than $V_{c.m.}$ ($\sim 4.0 cm/ns$) are the spray of projectile "splinters". In the case of 1% highest multiplicity gates (lower panels), the velocity distributions of H, He almost comprise one component with a peak at $V_{c.m.}$ ($\sim 4.0 cm/ns$), indicating a loss of memory of the projectile and the occur of vaporization decay. By contrast, the velocity distribution for IMFs still seems to have two components with a dominant isotropic component peaked at velocity of $\sim 2.0 cm/ns$, which indicates the existance of decay from a heavy fragment with velocity somewhat larger than for the case of 15% highest multiplicity gate but still lower than $V_{c.m.}$ of $\sim 4.0 cm/ns$. We can say that there is a considerable change of the ejectile emmision pattern from the 15% highest multiplicity gate to the 1% highest multiplicity gate. There must be a considerable increase in the excitation energy, which is probably the driving force for the large change in the ejectile emmision patterns. Probably the increase in excitation energy is larger than the 10% (from the 15% highest multiplicity gate to the 1% highest multiplicity gate) that we used for the model calculations, shown in Figure 7.1.
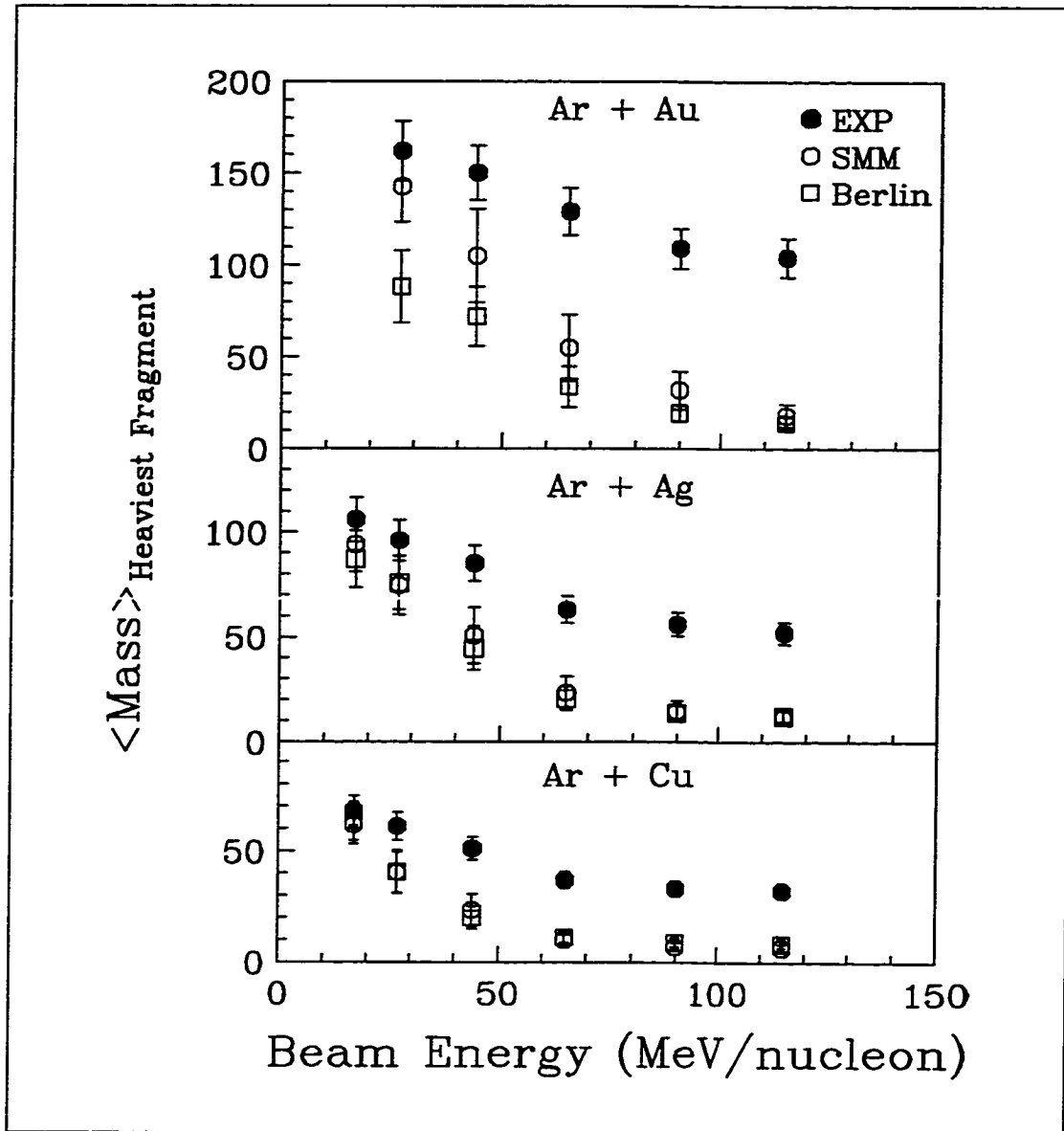
Figure 7.3: Comparison of the average mass of the heaviest fragment with multifragmentation models for ^{40}Ar + Cu, Ag and Au.

7.3   Evolution of Decay Modes of Hot Nuclei

To get a general picture of the decay modes of the hot nuclei, two properties of composite nuclei are studied in this section: 1) the average mass of the heaviest residual fragments; 2) The multiplicities of IMFs and LCPs. All the data are gated by requirement of highest 15% multiplicity.

Figure 7.3 shows the average mass of heaviest residual fragments versus beam energy for the three reaction systems of Ar + Cu, Ar + Ag and Ar + Au. All the data are gated by the highest 15% multiplicities, and the calculations use the excitation energies and masses extracted from data for the isotropic components. For an energy of 17 A MeV, results from the calculations and the data are generally very close (For Ar + Au, the Berlin model gives predominantly binary fission at the lower energies.). As the energy increases, the divergences increase. At 115 A MeV, experimental results for the average mass of heaviest fragments are about 30, 50 and 110 for Ar + Cu, Ar + Ag and Ar + Au respectively, however, values from the simulations are about 8, 12, and 18. This large divergence in the high energy region from 65 to 115 A MeV, indicates an over estimation of the breakup of heaviest fragments by the multifragmentation models.

This can be illustrated further by comparing average multiplicities of IMFs and light charged particles (LCPs) as shown in Figure 7.4. In the left hand panels, the data points show average multiplicities for the isotropic components of IMFs in the moving frame of heaviest residual. At the low energy of 17 A MeV, again the simulations and the data are rather close. But as the energy
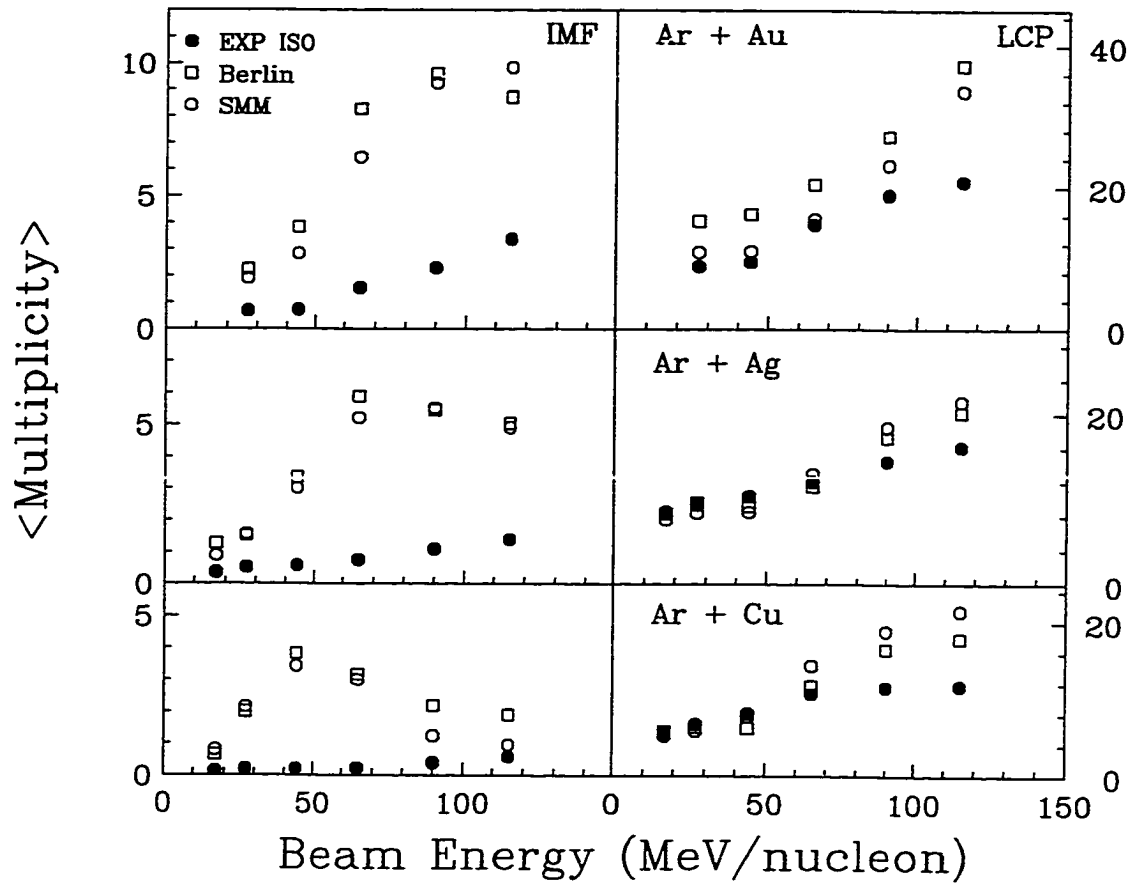
Figure 7.4: Comparison of the average multiplicity of IMFs and LCPs from multifragmentation models for ^{40}Ar + Cu, Ag and Au.

increases, the models predict larger multiplicities than the experimental results. For Ar + Au this divergence increases continously as the energy increases; however, for Ar + Ag and Ar + Cu, the simulated average multiplicities of IMFs decrease after a peak at 90 A MeV and 44 A MeV respectively. In the right hand panels, similar comparisons are displayed for LCPs. We can see that the data also increase continously as energy increases. However, for energies where the calculated multiplicities of IMFs decrease, there is an inflection point at which the multiplicities for LCPs increase even more rapidly. This is because the hot nuclei are being broken into even smaller pieces, i. e. into H and He particles. This can be said to be the onset of nuclear vaporization.

It seems clear that the models predict that a greater fraction of energy will go toward breaking up the nuclear bonding. The experimental data indicate that a larger fraction of the isotropic energy removal goes into kinetic energy. In the context of the multfragmentation models this "excess" kinetic energy could be called extra thermal energy. According to one's taste, extra thermal energy might be ascribed to prethermalization energy, blast energy, radial flow etc.

7.4   Summary

We have presented comparisons of experimental data to simulations from multifragmentation models. Average masses of the heaviest residual nuclei from these relatively high energy reactions are compared with models of multifragmentation. Large divergences appear between the experimental data and

calculated values. The multifragmentation models also predict essentially complete disassembly of these heavy nuclei for 65-115 A MeV; the experimental results show that there is only partial disassembly.

Chapter 8

Conclusions

8.1 Summary

The main body of this dissertation characterizes charged particle production along with slow moving heavy fragments for 8 − 115 AMeV ^{40}Ar + Cu, Ag, and Au reactions. The experiment was conducted with the K1200 cyclotron at the National Superconducting Cyclotron Laboratory (NSCL), MSU. Charged particles and fragments were detected and identified with the MSU 4π array. Energy and TOF, hence mass of heavy fragments, were determined with newly added Si detectors. The experiment focused on overall charged particle multiplicity and momentum measurements to determine the nuclear stopping and energy removal for central collisions and to compare the results to statistical and multifragmentation model predictions.

The reactions are classified by centrality or collision violence via the multiplicities of charged particles. For the mid-peripheral collisions, the mass and velocity measurements show characteristics of the well-known deep-inelastic

reactions, characterized by a group of projectile like fragments with average velocity near to that of the beam and a group of heavy target-like fragments with very low velocity. These characteristics persist even up to 115 A MeV reactions.

A continuous increase in the multiplicities from the central or most violent collisions is observed with increasing projectile energy. The heavy residual nuclei are found to accept a majority fraction of the projectile momentum only up to $\sim$ 44 A MeV, but then to yield this majority fraction to the ejectile spray for 65-115 A MeV. This confirms a dominance of the familiar incomplete fusion processes up to $\sim$ 44 A MeV, but then demonstrates a succession to splintering central collisions, a new reaction class for the Fermi energy domain.

For the central collisions, isotropic and forward-peaked components in the frame of the heaviest fragment have been separated for each ejectile type. The nuclear stopping is characterized via average longitudinal momenta for the heaviest fragment and for each ejectile type. The fractional importance of the isotropic components is dominant for the lowest energies where complete and incomplete fusion dominate and the compound-nucleus model rules. However, for beam energies of $\gtrsim$ 44 A MeV, the forward-peaked components dominate, and the momentum is widely spread over many ejectile types. The data show that the linear momentum transfer to the heavy core nucleus decreases with energy more rapidly for reactions of ^{40}Ar + Cu than for ^{40}Ar + Ag than for ^{40}Ar + Au, or one can say that the stopping power increases with target mass as is intuitively reasonable for these central collisions. Comparison of measured values of the average longitudinal velocity for the heaviest fragment with

BUU calculations shows that nuclear stopping power for this energy domain is much stronger for the BUU model than that found in the experiments. Average energy removal has been obtained for both isotropic and forward peaked ejectiles. The main ejectiles for energy removal are the light particles n, H, He with IMF's playing a relatively minor role. Ejectiles emitted isotropically in the frame of the heaviest fragment define average deposition energies that reach 1-2 GeV, but there is no clear signature for a liquid-gas phase transition.

Collective tranverse and rotational flow were measured via azimuthal correlation functions between each ejectile and the reaction plane which was determined by summing the momenta of projectile-like-fragments. More central collisions exhibit stronger flow than the mid-peripheral collisions. For these central collisions, the larger systems produce weaker flow at lower energies. The energy at which collective transverse flow disappears, termed the balance energy, was found to decrease as the mass of the target increases. These observations point toward stronger repulsive forces for the heavier targets.

The disassembly of the heaviest nuclei for these relatively high energy reactions has been compared with calculations of two multifragmentation models; large divergences appear between experimental data and calculated values. While the data indicate that heavier targetlike fragments persist even for higher initial excitation energies, the simulations predict more disassembly or breakup of the hot nuclei into middle sized pieces. As the energy is increased, the experimental results show a monotonic increase in IMF production from fragmentation of the hot nuclei. By contrast, the multifragmentation models predict that hot nuclei break down further into even smaller pieces, i. e. H and

He. This prediction for the increase of disassembly toward vaporization is not borne out for the 15% multiplicity cut in these reactions. The data indicate significantly more extra thermal isotropic kinetic energy removal than do the multifragmentation models.

Bibliography

[Aj96]   N.N. Ajitanand and J.M. Alexander, *Nucl. Instrum. Methods Phys. Res.* **A376**, 213 (1996).

[Al85]   S. Albergo et al. *Nuov. Cim.* **A89**, 1 (1985).

[Au86]   G. Auger et al., *Phys. Lett.* **B169**, (1986).

[Ba80]   R. Bass, *Nuclear Reactions with Heavy Ions*, (Springer-Verlag, New York, 1980), and references therein.

[Ba87]   H.W. Barz, J.P. Bondorf, and H. Schulz, *Nucl. Phys.* **A462**, 189 (1987).

[Ba92]   W.Bauer, G.F.Bertsch, H.Schultz, *Phys. Rev. Lett.* **69**, 1888 (1992).

[Be87]   G.F. Bertsch, W.G. Lynch, and M.B. Tsang, *Phys. Lett. B* **189**, 384 (1987).

[Be88]   G.F. Bertsch and S. DasGupta, *Phys. Reports* **160**, 189 (1988).

[Be94]   W. Benenson, D. Morissey, W. Friendman, *Annu. Rev. Nucl. Sci.*, 27 (1994).

[Bo85a] J.P. Bondorf, R. Donangelo, I.N. Mishustin, C.J. Pethick, H. Schulz, and K. Sneppen, *Nucl. Phys.* **A443**, 321 (1985).

[Bo85b] J.P. Bondorf, R. Donangelo, I.N. Mishustin, and H. Schulz, *Nucl. Phys.* **A444**, 460 (1985).

[Bo94] J. Boger, J.M. Alexander, R.A. Lacey, and A. Narayanan, *Phys. Rev.* **C49**, 1587 (1994).

[Ce91] D.A. Cebra, S. Howden, J. Karn, D. Kataria, M. Maier, A. Nadasen, C.A. Ogilvie, N. Stone, D. Swan, A. Vander Molen, W.K. Wilson, J. Yurkon, G.D. Westfall, and E. Norback, *Nucl. Instrum. Methods* **A300**, 518 (1991).

[Ce92] D.A. Cebra, W.K. Wilson, A. Vander Molen, and G.D. Westfall, *Nucl. Instrum. Methods* **A313**, 367 (1992).

[Ch97] A. Chbihi et al., *Phys. Rev.* **C34**, 652 (1997).

[Co98] E.Y. Colin, PhD thesis, devant l'Université Claude Bernard Lyon-1, 1998.

[Co98a] E.Y. Colin et. al., *Phys. Rev.* **C57**, R1032 (1998).

[Cr91] E. Crema et. al., *Phys. Lett.* **B258**, 266 (1991).

[Cu82] J. Cugnon, J. Knoll, C.Riedel, and Y. Yariv, *Phys. Lett.* **109B**, 167 (1982).

[Da85] P. Danielewicz and G. Odyniec, *Phys. Lett.* **157B**, 146 (1985).

[Da95]   P. Danielewicz, *Phys. Rev. C* **51**, 716 (1995).

[Do87]   K.G.R. Doss, H.Å. Gustafsson, H. Gutbrod, J.W. Harris, B.V. Jacak, K.H. Kampert, B. Kolb, A.M. Poskanzer, H.G. Ritter, H.R. Schmidt, L. Teielbaum, M. Tincknell, S. Weiss, and H. Weiman, *Phys. Rev. Lett.* **59**, 2720 (1987).

[Du97]   D. Durand, *LPC Caen Report LPC C98-02 Lectures at Mont-St. Odile* Sept. 1997, and references therein.

[Et92]   T. Ethvignot, N.N. Ajitanand, C.J. Gelderloos, J.M. Alexander, E. Bauge, A. Elmaani, R.A. Lacey, P. Desesquelles, H. Elhage, A. Giorni, D. Heuer, S. Kox, A. Lleres, F. Merchez, C. Morand, D. Rebreyend, P. Stassi, J.B. Viano, F. Benrachi, B. Chambon, B. Cheynis, D. Drain, C. Pastor, *Nucl. Phys.* **A545**, 347c (1992).

[Ga90]   C. Gale et al., *Phys. Rev.* **C41**, 1545 (1990).

[Ga96]   E.J. Garcia-Solis and A.C. Mignerey, *Phys. Rev.* **C54**, 276 (1996).

[Ge94]   C.J. Gelderloos, *PhD Thesis*, Dept. of Physics, State University of New York at Stony Brook. 1994.

[Gr82]   C.R. Gruhn, M. Binimi, R. Legrain, R. Loveman, W. Pang, M. Roach, D.K. Scott, A. Shotter, T.J. Symous, J. Wouters, M. Zisman, R. de Vries, Y.C. Peng, and W. Sondheim, *Nucl. Instr. and Methods* **196**, 33 (1982).

[Gr86]   D.H.E. Gross, Zhang Xiao-Ze, Xu Shu-yan, *Phys. Rev. Lett.* **56**, 1544 (1986).

[Gr90]   D.H.E. Gross, *Rep. Prog. Phys.* **53**, 605 (1990).

[Gu89]   H.H. Gutbrod, A.M. Poskanzer, and H.G. Ritter, *Rep. Prog. Phys.* **52**, 1267 (1989).

[Gy82]   M. Gyulassy, K.A. Frankel, and H. Stöcker, *Phys. Lett.* **110B**, 185 (1982).

[Ha96]   F. Haddad et al., *Phys. Rev.* **C53**, 1437 (1996).

[Ha97]   J. A Hauger et al. *Phys. Rev. Lett.* **77** 2, 235 (1996).

[Hu97]   B. Hurst et al., *Cyclotron Institute Report 97-06*, Texas A & M University, College Station, TX 77843-3366.

[Ji89]   D.X. Jiang et al., *Nucl. Phys.* **A503**, 560 (1989).

[Ke92]   W.L. Kehoe, A.C. Mignerey, A. Moroni, I. Iori, and G.F. Peaslee, et al., *Nucl. Instrum. Methods* **A311**, 258 (1992).

[Kr89]   D. Krofcheck, W. Bauer, G.M. Crawley, C. Djalali, S. Howden, C.A. Ogilvie, A. Vander Molen, G.D. Westfall, W.K. Wilson, R.S. Tickle, C. Gale, *Phys. Rev. Lett.* **63**, 2028 (1989).

[La87]   G. La Rana, D.J. Moses, W.E. Parker, M. Kaplan, D. Logan, R. Lacey, J.M. Alexander, R.J. Welberry, *Phys. Rev.* **C35**, 373 (1987).

[La88]   R. Lacey, N.N. Ajitanand, J.M. Alexander, D.M. de Castro Rizzo, G.F. Peaslee, L.C. Vaz, M. Kaplan, M. Kildir, G. La Rana, D.J. Moses, W.E. Parker, D. Logan, M.S. Zisman, P. DeYoung, L. Kowalski, *Phys. Rev.* **C37**, 2561 (1988).

[La98]   J. Lauret et al., *Phys. Rev.* **C57**, R1051 (1998).

[Lo93]   B. Lott et al., *Z. Phys.* **A346**, 20 (1993).

[Ma96a]   N. Marie, et al. *Phys. Lett.* **B391**, 15 (1996).

[Ma96]   M.T. Magda, E. Bauge, A. Elmaani, T. Braunstein, C.J. Gelderloos, N.N. Ajitanand, J.M. Alexander, T. Ethvignot, P. Bier, L. Kowalski, et al., *Phys. Rev. C* **53**, R1473-R1477 (1996).

[Mo78]   J.B. Moulton, J.E. Stephenson, R.P. Schmitt and G.J. Wozniak, *Nucl. Instrum. Methods* **A157**, 325 (1978).

[Mo84]   H. Morgenstern, W. Bohne, W. Galster, K. Grabisch, A. Kyanowski, *Phys. Rev. Lett.* **52**, 1104 (1984).

[Mo85]   J.J. Molitoris and H. Stöcher, *Phys. Lett.* **162B**, 47 (1985).

[Mo92]   L.G. Moretto, G.J. Wozniak, *Annu. Rev. Nucl. Part. Sci.* **43**, 379 (1992).

[Og90]   C.A. Ogilvie et al., *Phys. Rev.* **C42**, R10 (1990).

[Pa93]   Q. Pan and P. Danielewicz, *Phys. Rev. Lett.* **70**, 2062 (1993).

[Pa96]   R. Pak Ph.D. *Thesis*, Department of Physics, Michigan State University, 1996.

[Pa97a] R. Pak, Bao-An Li, W. Benenson, O. Bjarki, J.A. Brown, S.A. Hannuschke, R.A. Lacey, D.J. Magestro, A. Nadasen, E. Norbeck, D.E. Russ, M. Steiner, N.T.B. Stone, A.M. Vander Molen, G.D. Westfall, L.B. Yang, and S.J. Yennello, *Phys. Rev. Lett.* **78**, 1026 (1997).

[Pa97b] R. Pak, W. Benenson, O. Bjarki, J.A. Brown, S.A. Hannuschke, R.A. Lacey, Bao-An Li, J. Lauret, A. Nadasen, E. Norbeck, P. Pogodin, D.E. Russ, M. Steiner, N.T.B. Stone, A.M. Vander Molen, G.D. Westfall, L.B. Yang, and S.J. Yennello, *Phys. Rev. Lett.* **78**, 1022 (1997).

[Pi91]   E. Piasecki et al., *Phys. Rev. Lett.* **66**, 1291 (1991).

[Po87]   J. Pochodzalla, C.K. Gelbke, W.G. Lynch, M. Maier, D. Ardouin, H. Delagrange, H. Doubre, C. Gregoire, A. Kyanowski, W. Mittig, A. Peghaire, J. Peter, F. Saint-Laurent, B. Zwieglinski, G. Bizard, F. Lefebvres, B. Tamain, J. Quebert, Y.P. Viyogi, W.A. Friedman, D.H. Boal, *Phys. Rev.* **C35**, 1695 (1987).

[Po95]   J. Pochodzalla et al., *Phys. Rev. Lett.* **75**, 1040 (1995).

[Po98]   A.M. Poskanzer and S.A. Voloshin, *Phys. Rev. C*, in pressed.

[Qu93]   B.M. Quednau et al., *Phys. Lett.* **B309**, 10 (1993).

[Na95] J.B. Natowitz, *Nuclear Chemistry Award Symposium*, American Chemical Society, Anaheim, California, 1995.

[Ra93] J. Randrup, G. Batko, *Prog. Part. Nucl. Phys.*, **30**, 117 (1993).

[Ru98] N.D. Russ, *Ph.D Thesis*, University of Maryland, 1996.

[Sc84] W.U. Schröder and J.R. Huizenga, em Treatise on Heavy-Ion Science, Vol 2, Ed. by D.A. Bromely, Plenum, New York, 1994; Chapter 3.

[St80] H. Stöcker, J.A. Maruhn, and W. Greiner, *Phys. Rev. Lett.* **44**, 725 (1980).

[St86] H. Stöcker and W. Greiner, *Phys. Rep.* **137**, 277 (1986).

[St96] N. T. B. Stone, Ph.D. Thesis, Michigan State University, Department of Physics, 1996.

[Ta96] B. Tamain and D. Durand, *Proceedings of the Summer School*, Les Houches, (1996).

[To92] J. Töke and W.U Schröder, *Annu, Rev. Nucl. Part. Sci.* **42**, 401 (1992).

[Ts84] M.B. Tsang, G.F Chitwood, D.J. Fields, C.K. Gelbke, D.R. Klesch, W.G. Lynch, K. Kwiatkowski, and V.E. Viola, *Phys. Rev. Lett.* **52**, 1967 (1984).

[Ts93] M.B. Tsang, W.C. Hsi, W.G. Lynch, D.R. Bowman, C.K. Gelbke, M.A. Lisa, G.F. Peaslee, G.J. Kunde, M.L. Begemann-Blaich, T.

Hofmann, J. Hubele, J. Kempter, P. Kreutz, W.D. Kunze, V. Linden-struth, U. Lynen, M. Mang, W.F.J. Muller, M. Neumann, B. Ocker, C.A. Ogilvie, J. Pochodzalla, F. Rosenberger, H. Sann, A. Schuttauf, V. Serfling, J. Stroth, W. Trautmann, A. Tucholski, A. Worner, E. Zude, B. Zwieglinski, S. Aiello, G. Imme, V. Pappalardo, G. Raciti, R.J. Charity, L.G. Sobotka, I. Iori, A. Moroni, R. Scardoni, A. Ferrero, W. Seidel, Th. Blaich, L. Stuttge, A. Cosmo, W.A. Friedman, G. Peilert, *Phys. Rev. Lett.* **71**, 1502 (1993).

[Vi82] V.E. Viola, *Z. Phys.* **A307**, 221 (1982).

[Vi89] V. E. Viola et al., *Nucl. Phys.* **A502** 531 (1989).

[We85] G. D. Westfall et al., *Nucl. Instrum. Methods* **A238**, 347 (1985);

[Wi52] D.H. Wilkinson, *Rev. Sci. Instr.* **23**, 414 (1952).

[Wi92] W.K. Wilson, R. Lacey, C.A Ogilvie, and G.D. Westfall, *Phys. Rev.* **C 51**, 3136 (1995).

[Yo92] A. Yokoyama et al., *Phys. Rev. C* **46**, 647 (1992).

[Zh87] X.Z. Zhang, D.H.E. Gross, S.Y. Xu, and Y.M. Zheng, *Nucl. Phys.* **A461**, 641 (1987).

Appendix A

Reaction Simulations and Models

Model predictions serve as a guide to help understand the signatures of reaction mechanisms. In this study several simulation models are used to compare with experimental result. In this appendix, brief introductions from the thesis of Daniel E. Russ [Ru98] and original references are given for those models including the statistical model MODGAN [Aj96], Boltzmann-Uehling-Uhlenbeck (BUU) model [Be88], the Statistical Multifragmentation (SMM or the Copenhagen) model [Bo85a, Bo85b, Ba87] and the Berlin model [Gr86, Zh87, Gr90].

A.1 MODGAN

MODGAN [Aj96] is an evaporation model to follow ejectile kinematics and complex decay chains from highly excited nuclei with multi-step Monte Carlo calculations. In MODGAN, the angular distribution (with respect to the parent spin vector J_p) for emitted particles of orbital angular momentum

l and channel energy ϵ is described as,

$$W(\epsilon,l,\theta) = T_l(\epsilon)\rho(E_p - \epsilon - S, J_p)(l + \frac{1}{2}) \times exp(-\frac{\hbar^2(l+\frac{1}{2})^2}{2T\varphi_d})\frac{1}{2\pi}H, \quad (A-1)$$

where

$$H = I_0(\frac{\hbar^2(J_p + \frac{1}{2})(l + \frac{1}{2})}{T\varphi_d}sin\theta). \quad (A-2)$$

and T is the temperature, ρ is the density, S is the separation energy, and I_0 is an associated Bessel function.

This expression can be analytically integrated to different levels, under the sharp cut-off approximation for T_l, yielding a set of analytical expressions that can be used to quickly build the unrestricted multi-step decay chain described as follows:

1) Choose the particle in proportion to its branching ratio B_i given by,

$$B_i = \frac{\Gamma_i}{\sum_i \Gamma_i}. \quad (A-3)$$

2) Choose the direction θ of the particle with respect to J_p according to the expression,

$$p(cos(\theta)) \propto exp(\beta_2 sin^2\theta). \quad (A-4)$$

3) choose the exit channel orbital angular momentum l according to the expression,

$$p(l) \propto l exp(-\alpha l^2)I_0(2\sqrt{\beta l^2}), \quad (A-5)$$

where $\alpha = (k_1+k_2)/T$, $k_1 = 1/(2\varphi_d)$, $k_2 = 1/(2\mu R^2)$ and $\beta = sin^2\theta(k_1^2(J_p\frac{1}{2})^2)/T^2$.

4)Choose the channel energy ϵ according to the distribution

$$p(\epsilon) \propto T_l exp(-\frac{\epsilon}{T}). \quad (A-6)$$

5) Finally, choose the direction of l in a plane perpendicular to the particle direction according to the distribution,

$$p(cos\theta_l) \propto \frac{exp[\frac{\hbar^2}{2T\varphi_d}(J_p + \frac{1}{2})(l + \frac{1}{2})cos\theta_l]}{\sqrt{sin^2\theta - cos^2\theta_l}}, \qquad (A-7)$$

where θ_l = angle of l) with respect to J_p and $-|sin\theta| < cos\theta_l < |sin\theta|$.

6) Obtain the properties of the residual nucleus such as charge, mass, spin vector, thermal excitation energy, and recoil velocity using conservation laws.

7) Repeat steps 1-6 for the next emission. Continue building the chain in this manner. Terminate the chain when the temperature of residual nucleus falls below 0.5 MeV.

A.2 Boltzmann-Uehling-Uhlenbeck Equation (BUU)

The BUU equation is a combination of the cascade model and the Vlasov equation[Be88]. In the cascade model, the nucleus is considered as a spherical collection of point particles. The nucleus is then boosted to beam velocity and given a particular impact parameter with respect to the target. The projectile and target nucleons are allowed to scatter off each other and are followed throughout the reaction. The cascade model treats only the hard scattering of nucleons and ignores mean-field effects. The Vlasov equation is an approximation of time dependent Hartree-Fock theory. The BUU equation is

$$\frac{\partial f}{\partial t} + \nu \bullet \nabla_r f - \nabla_r U \bullet \nabla_p f = \bar{I}|f|, \qquad (A-8)$$

where $\bar{I}|f|$ is the average rate of change of the particle distribution f. This is numerically solved using the cascade model. The left side of the equation,

when set to zero, is the Vlasov equation. The mean-field potential U used in the BUU equation is a density dependent Skyrme potential

$$U(\rho) = A(\frac{\rho}{\rho_0}) + B(\frac{\rho}{\rho_0})^\sigma, \qquad (A-9)$$

where the A term is attractive, the B term is repulsive, $\sigma > 1$, ρ is the density, and ρ_0 is the normal nuclear density ($\sim 0.15 fm^{-3}$).

The solution to the BUU equation is a particle distribution function; it does not produce individual fragments. A clustering routine is necessary to create fragments out of the particle distributions. Garcia-Solis' [Ga96] clustering routine has been used in this study. The routine looks for fragment seeds by breaking up coordinate space into cubes with sides $2r_b$. The cube is considered "interior" if the nuclear density at the center of each face of the cube is greater than normal nuclear density. In this case, the nucleons in the center are surrounded by nuclear matter. A nucleon is an "exterior nucleon" that is part of the cluster if its momentum and position are within the Fermi momentum and r_b, the cube size of the seeds.

A.3 Statistical Multifragmentation Model

The statistical multifragmentation model SMM [Bo85a, Bo85b, Ba87] starts with an excited compressed system characterized by mass A_0, charge Z_0 and total energy E_0. The system goes through three stages. First, during formation of the hot system, cracks form in the system. Second, the system expands and fragments form. Last, light particles evaporate removing the last of the excitation energy. Before the system expands through a break-up volume,

thermal equilibrium is reached and the system attains an average composition of protons and neutrons. After the break-up the system is in a final state partition. The partition consists of all the fragments that the system broke into. The probability that the final state is in partition F is given by

$$\delta\Gamma_F = expS_F(A_0, Z_0, E_0), \qquad (A-10)$$

where S_F is the final state entropy. The final states are constrained by

$$\sum_{A,Z} N_{A,Z}A = A_0, \qquad (A-11)$$

$$\sum_{A,Z} N_{A,Z}Z = Z_0, \qquad (A-12)$$

and

$$\bar{E}_{tot} = \frac{3Z_0^2 e^2}{5R} + \sum_{A,Z} \bar{N}_{A,Z}\bar{E}_{A,Z} = \bar{E}_0^{ground} + \bar{E}_0^* = \bar{E}_0, \qquad (A-13)$$

where $N_{A,Z}$ is the multiplicity of fragments with mass A and charge Z, and E_0^* is the excitation energy above the ground state E_0^{ground}. The total energy E_{tot} is the sum of the Coulomb energy of a homogeneous charged sphere of radius R and the contribution of the individual fragments. The energy $E_{A,Z}$ for each fragment with mass A and charge Z is approximated using the liquid drop model as the sum of bulk, surface, clustering, Coulomb, and translational energies.

A.4 Berlin Multifragmentation Model

The Berlin model [Gr86, Zh87, Gr90] is a statistical multifragmentation model developed by D.H.E Gross of Institute of Hahn-Meitner at Berlin. It has

similar general scenarios with SMM for the decay of excited systems, but differs in detailed treatment. In the Berlin model, a microcanonical Metropolis Monte Carlo (MMMC) method is applied to describe the fragmentation of a hot system characterized by mass A_0, charge Z_0 and total energy E_0. A detailed description of MMMC can be found in the references [Gr86, Zh87, Gr90]; we introduce some essential points here.

The starting point of the Berlin model is a post-collision system of mass A_0, charge Z_0 with excitation energy of E_0. Driven by excitation energy and/or a compression, this system expands to a "freeze-out" stage for the formation of fragments in a volume V. Then the treatment of multifragmentation is approached via a microcanonical ensemble that can be described as follows:

1) A possible configuration f of M particle of a multifragmentation can be defined by an ensemble of microscopic variables

$$f : a_i, z_i, p_i, \epsilon_i, r_i; 1 \le i \le M, \qquad (A-14)$$

where a_i, z_i, p_i, ϵ_i, and r_i stand for the charge, mass, momentum, excitation energy and the position of particle i.

2) Unlike the canonical approach, which fixes the temperature and violates the energy conservation laws, these variables are constrained by the

conservation laws like:

$$
\left\{
\begin{array}{l}
A_0 = \sum_{i=1}^{M} a_i \\[2em]
Z_0 = \sum_{i=1}^{M} z_i \\[2em]
E^* = E_f
\end{array}
\right.
$$

In this particular case of statistical physics, energy is conserved and each partition f of the microcanonical ensemble has an energy equal to the starting excitation energy. There are no explicit constraints imposed on the temperature of the system. The latter is given by the relation of entropy with energy.

3) Each state is considered equally probable of having a partion f that is determined by the number of microscopic states giving rise to that partition and will be determined by its entropy. A statistical weight can therefore be associated with each partition.

Because of the extremely large number of configurations, it is impossible in a computer simulation to populate every configuration. The Metropolis method does not sample the states from the uniform distribution as in ordinary Monte-Carlo calculations, but rather it moves in small steps on a continuous path through the most important part of phase space. Only a few degrees of freedom are changed when going from one state to another.

Appendix B

More Data for Directed Transverse Flow

Ar+ Ag, H Azimuthal Correlation Function, Mult>85%
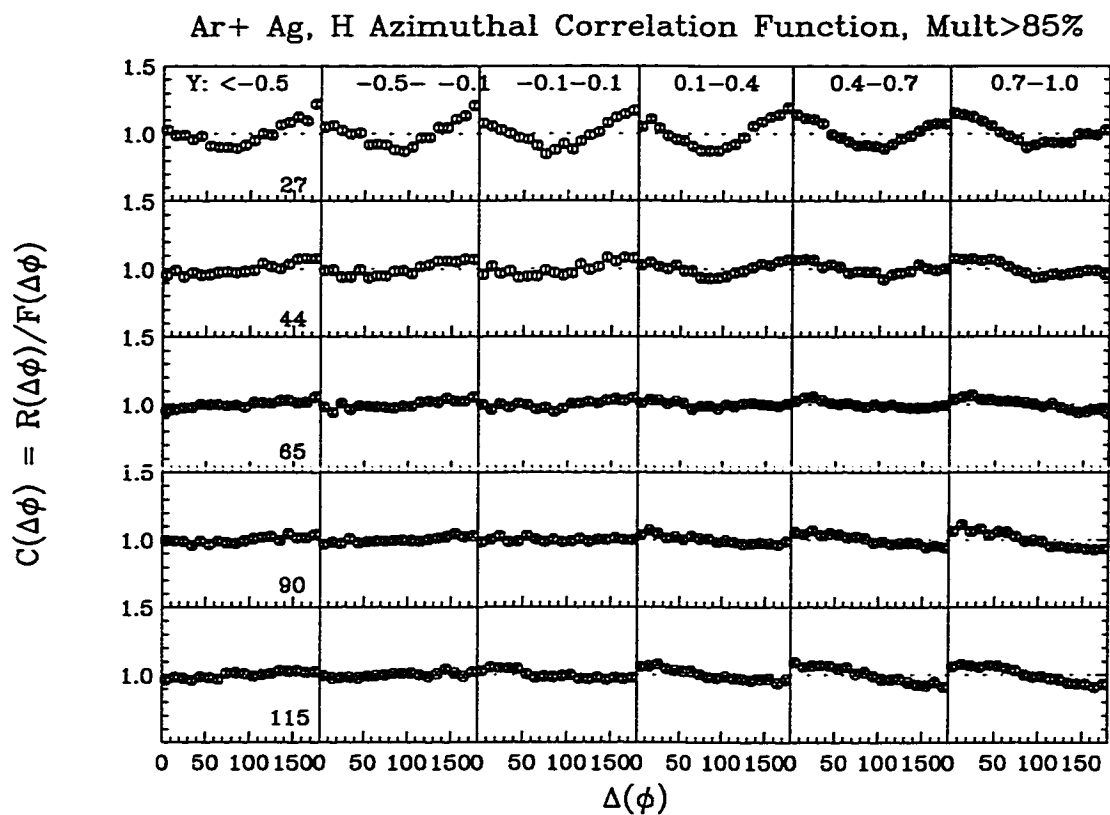
Figure B.1: Azimuthal correlation functions of H for Ar+Ag reaction. the columns represent different rapidity cuts, the rows represent different beam energies.

Ar+ Cu, H Azimuthal Correlation Function, Mult > 85%
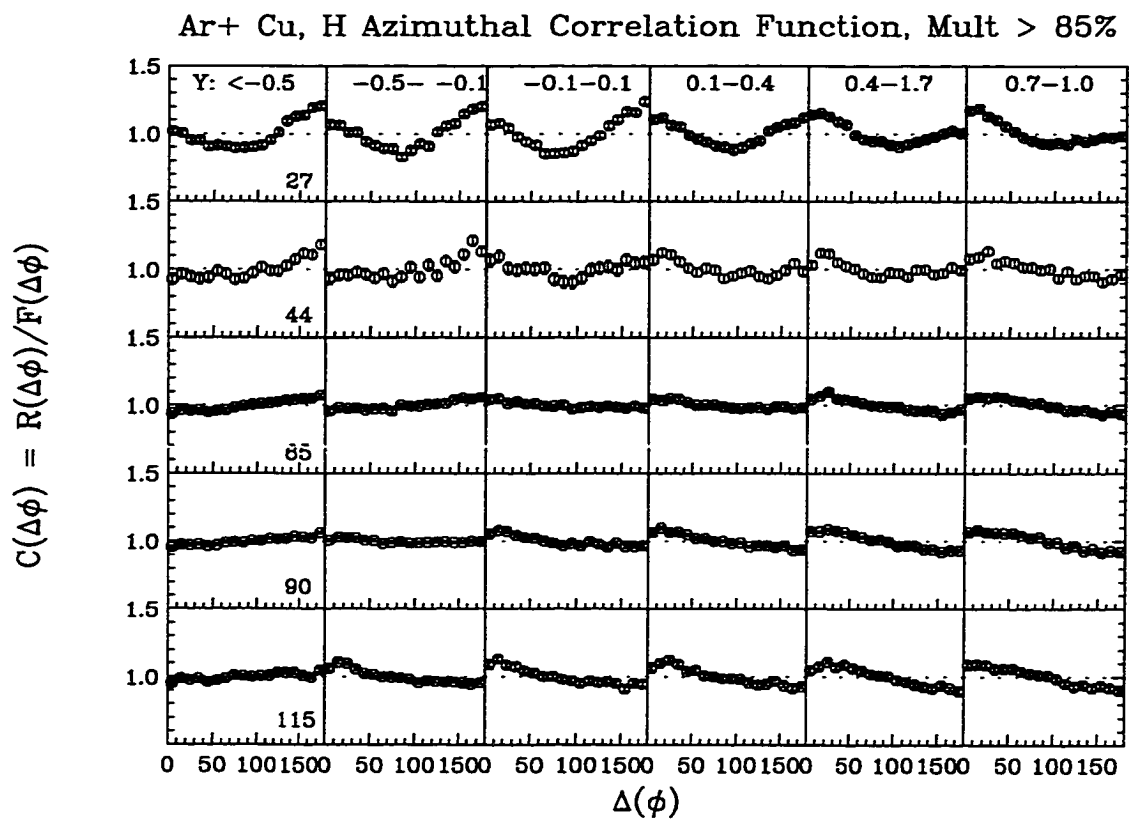
Figure B.2: Azimuthal correlation functions of H for Ar+Cu reactions.
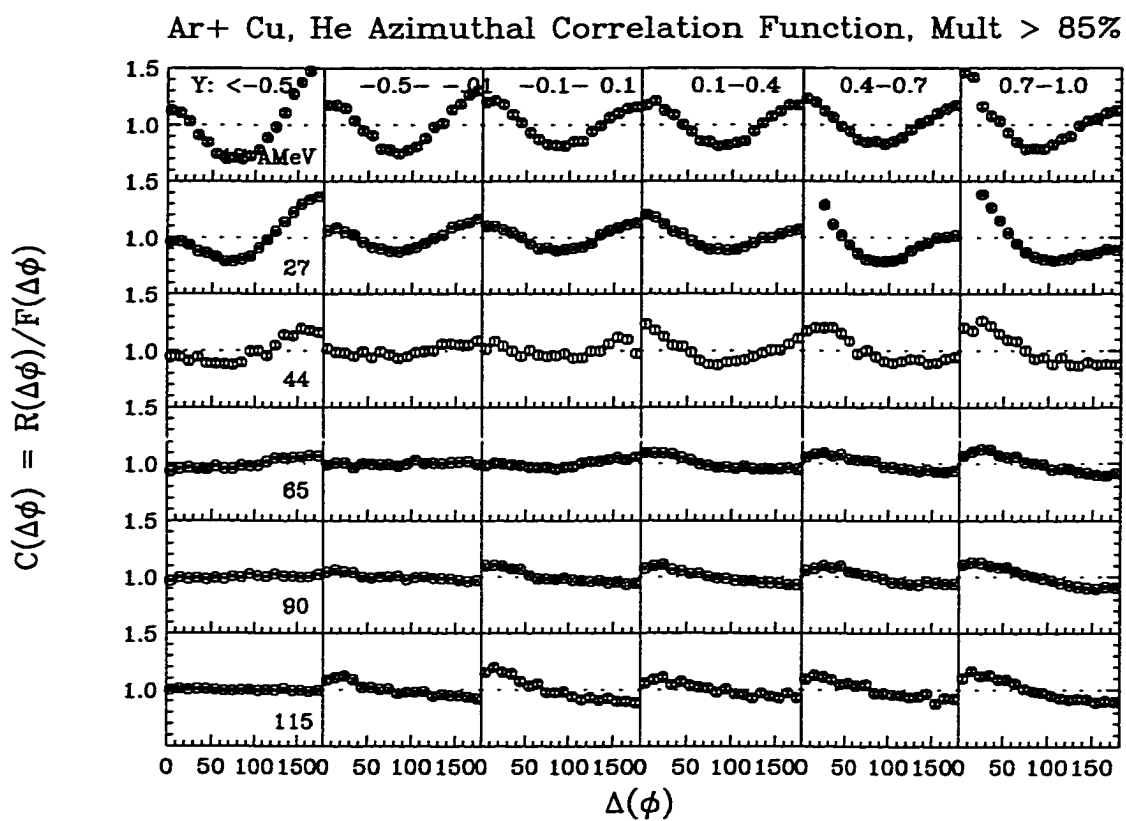
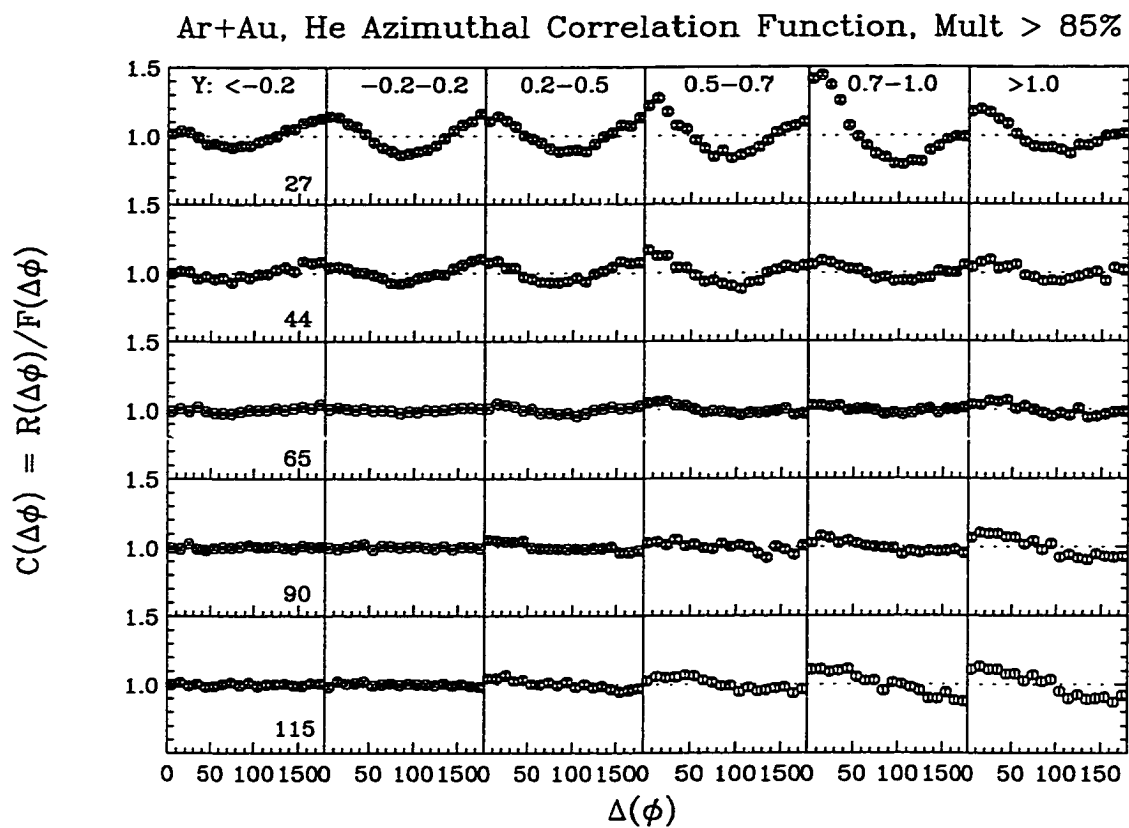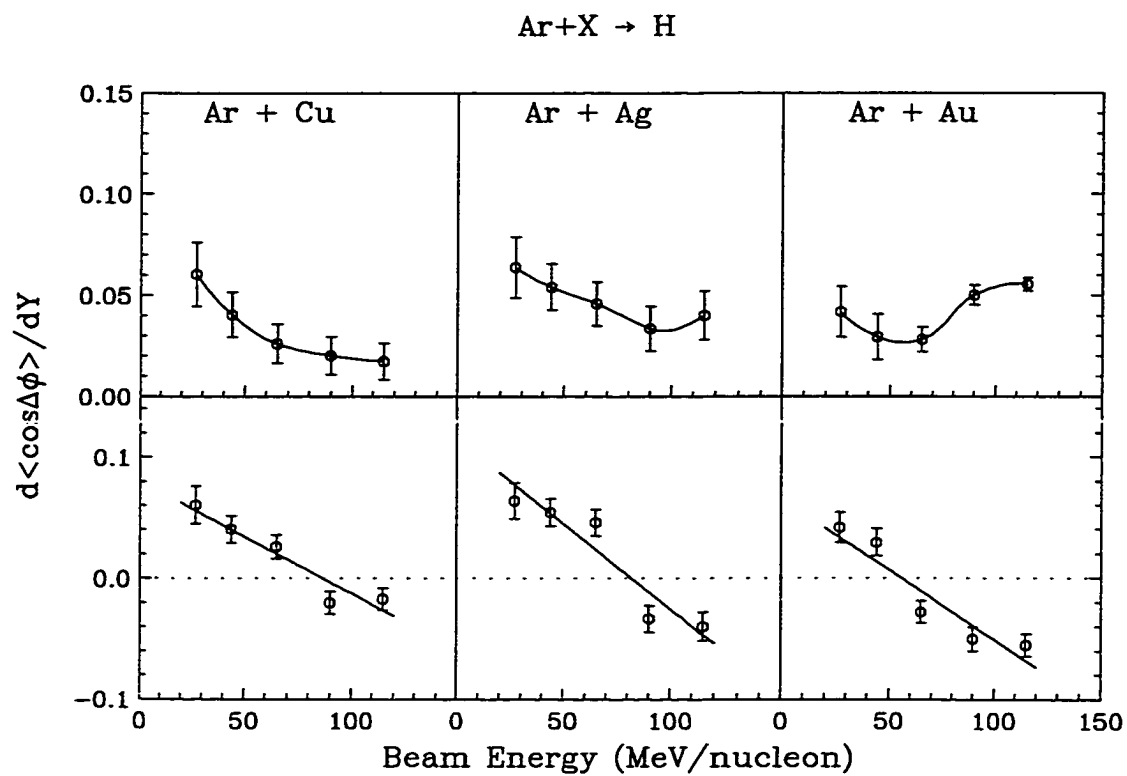**Figure B.3:** Azimuthal correlation functions of He for Ar+Cu reactions.
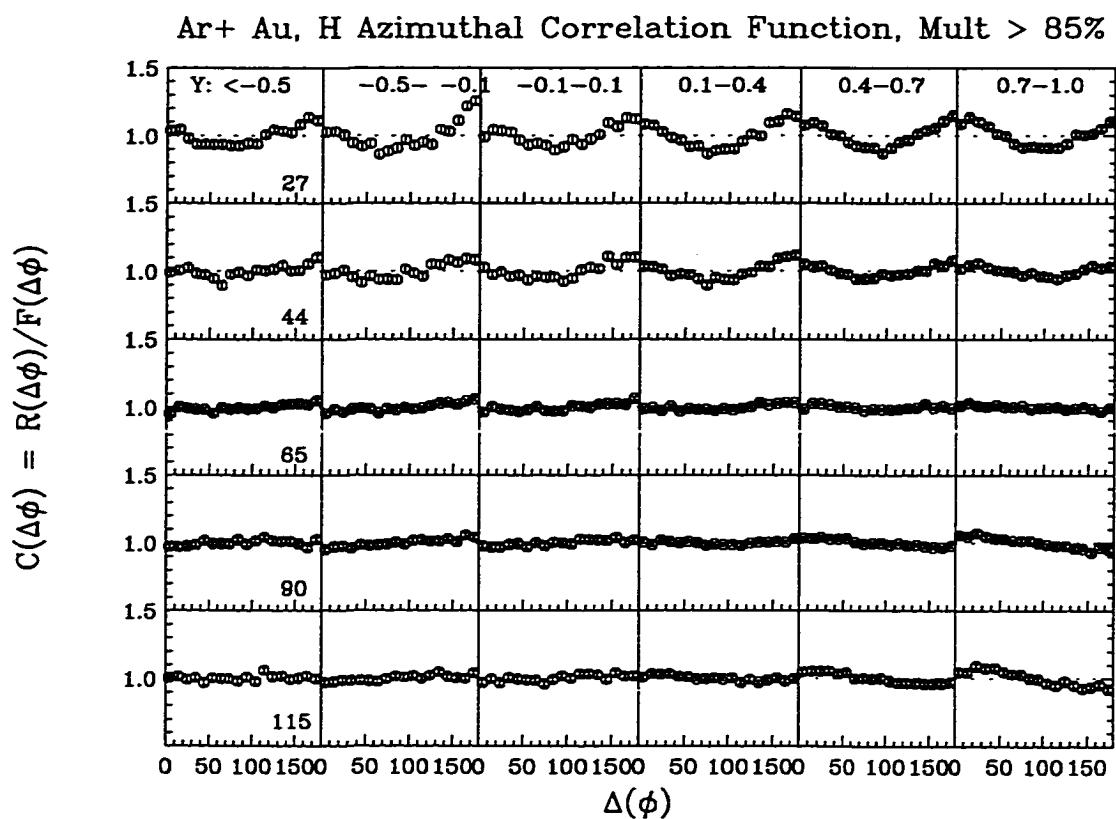
Figure B.4: Azimuthal correlation functions of H for Ar+Au reactions.

Ar+Au, He Azimuthal Correlation Function, Mult > 85%

Figure B.5: Azimuthal correlation functions of He for Ar+Au reactions.

Figure B.6: The evolution of reduced transverse flow of H particles for Ar + Cu, Ag and Au.

Ar+X → IMF
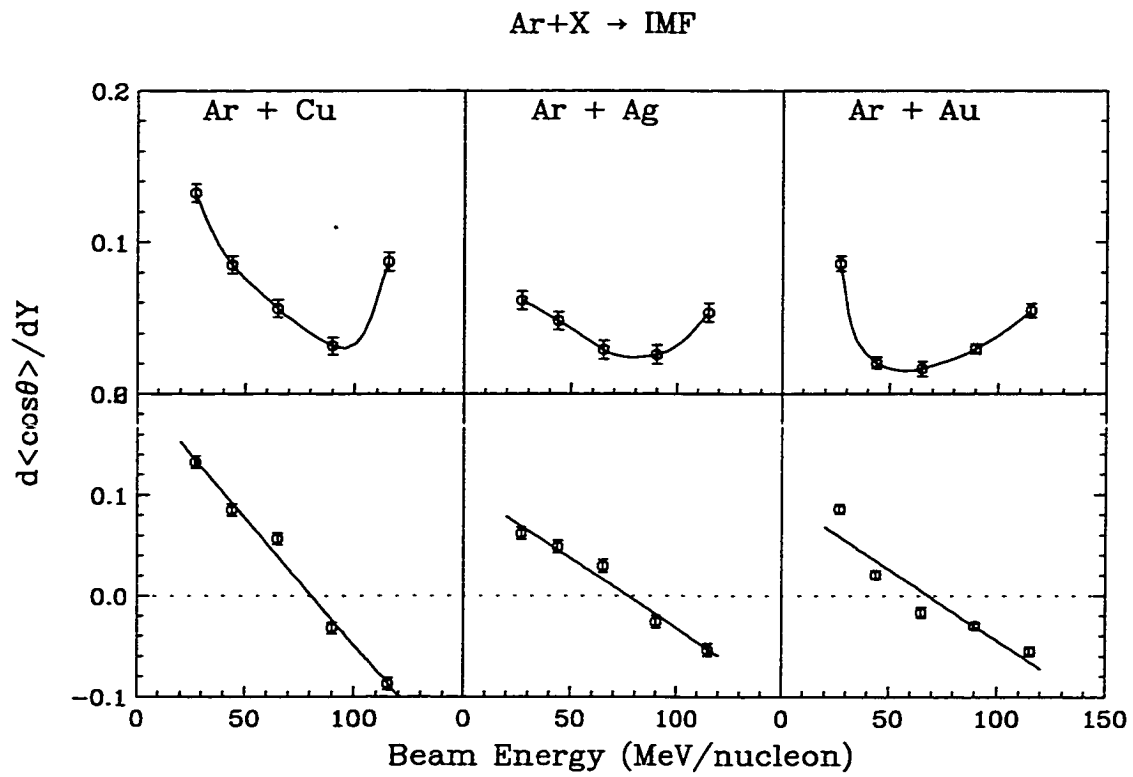
Figure B.7: The evolution of reduced transverse flow of IMF's for Ar + Cu, Ag and Au.

Appendix C

Data for Azimuthal Correlations between Various Ejectiles Selected by Angular Cut
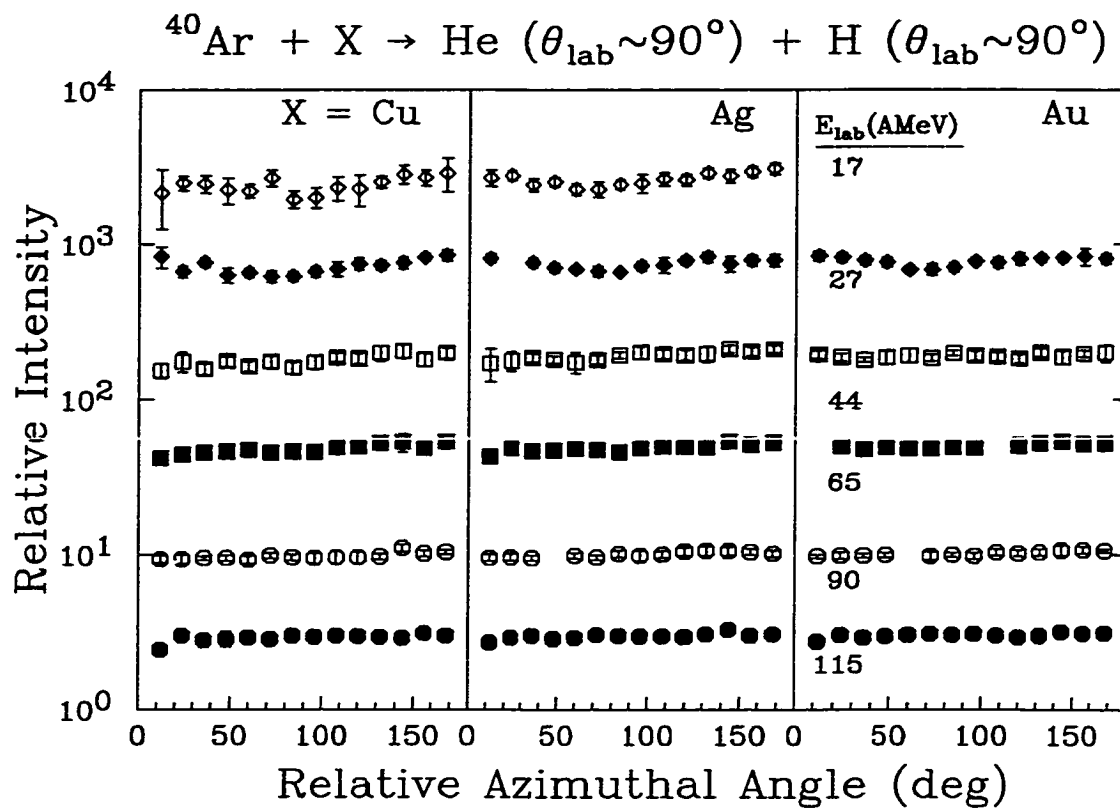
Figure C.1: Correlation functions between He and H at $\theta_{lab} \sim 90^0$ for Ar+Cu, Ag and Au.

$$^{40}\text{Ar} + \text{X} \rightarrow \text{He} \ (\theta_{\text{lab}} \sim 90^\circ) + \text{He} \ (\theta_{\text{lab}} \sim 90^\circ)$$
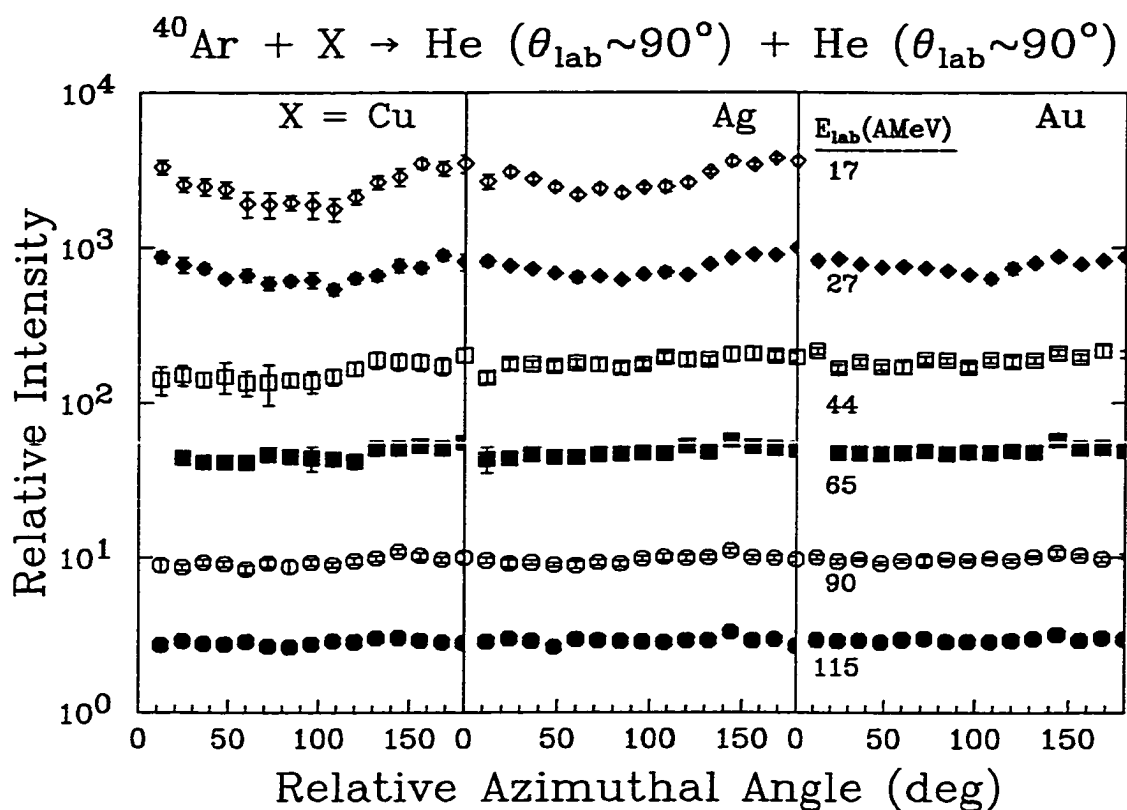
Figure C.2: Correlation functions between He and He at $\theta_{lab} \sim 90^\circ$ for Ar+Cu, Ag and Au.
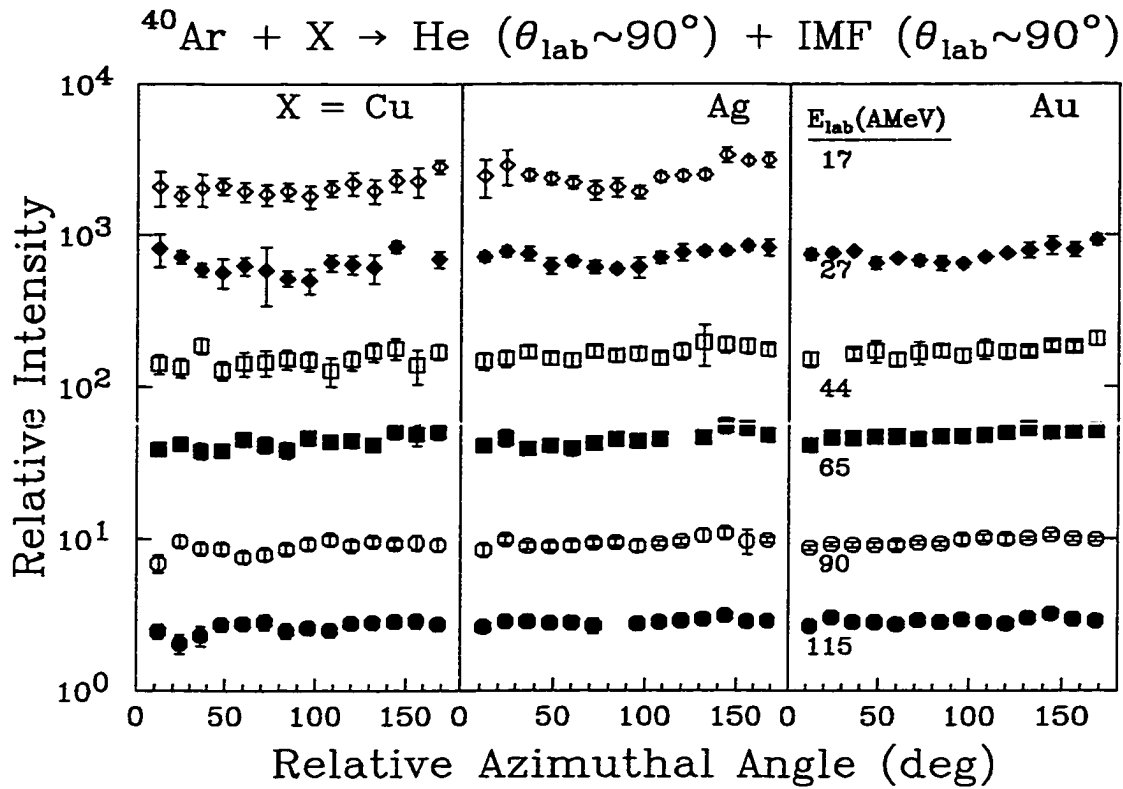
Figure C.3: Correlation functions between He and IMF at $\theta_{lab} \sim 90^\circ$ for Ar+Cu, Ag and Au.
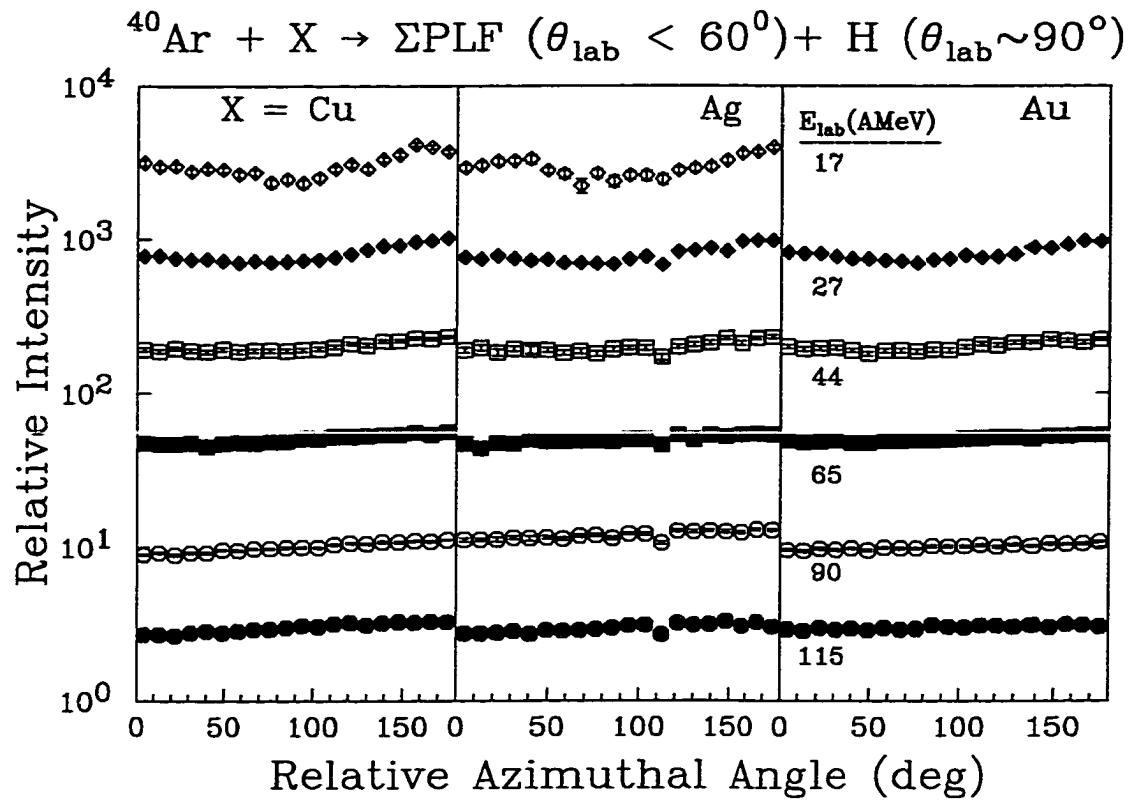
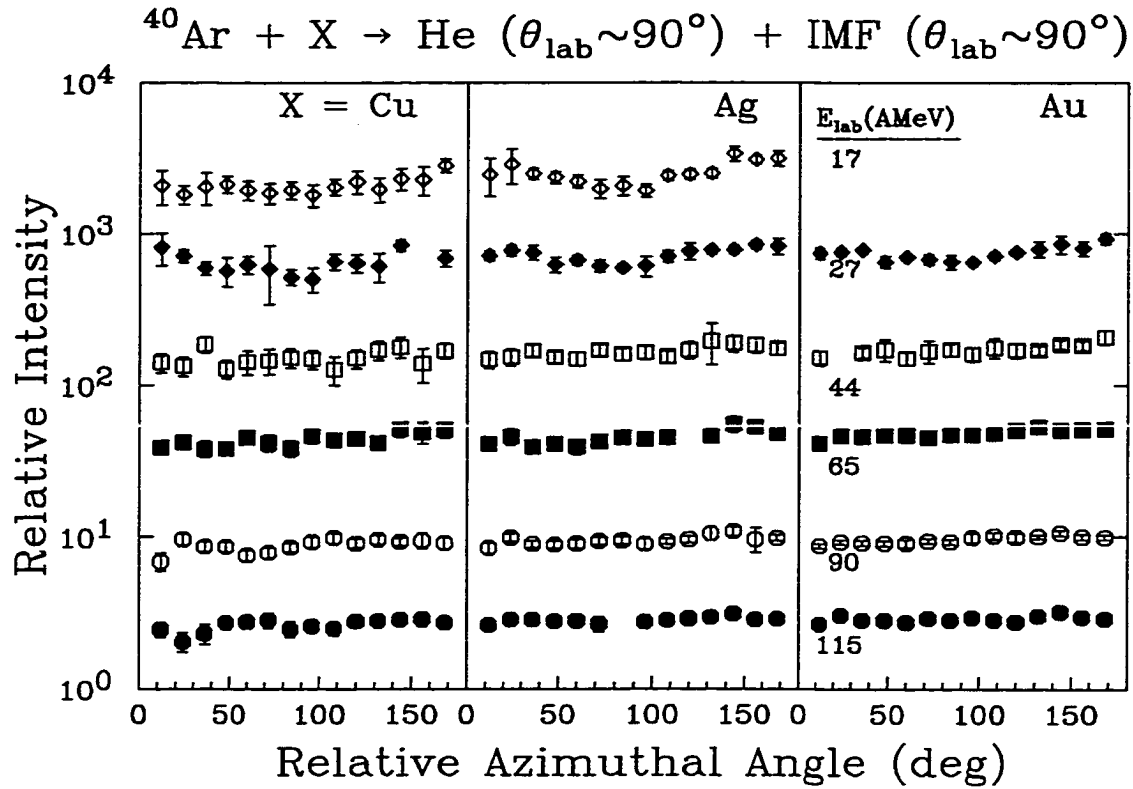Figure C.4: Azimuthal correlation functions of H at $\theta_{lab} \sim 90^0$ for Ar+Cu, Ag and Au.
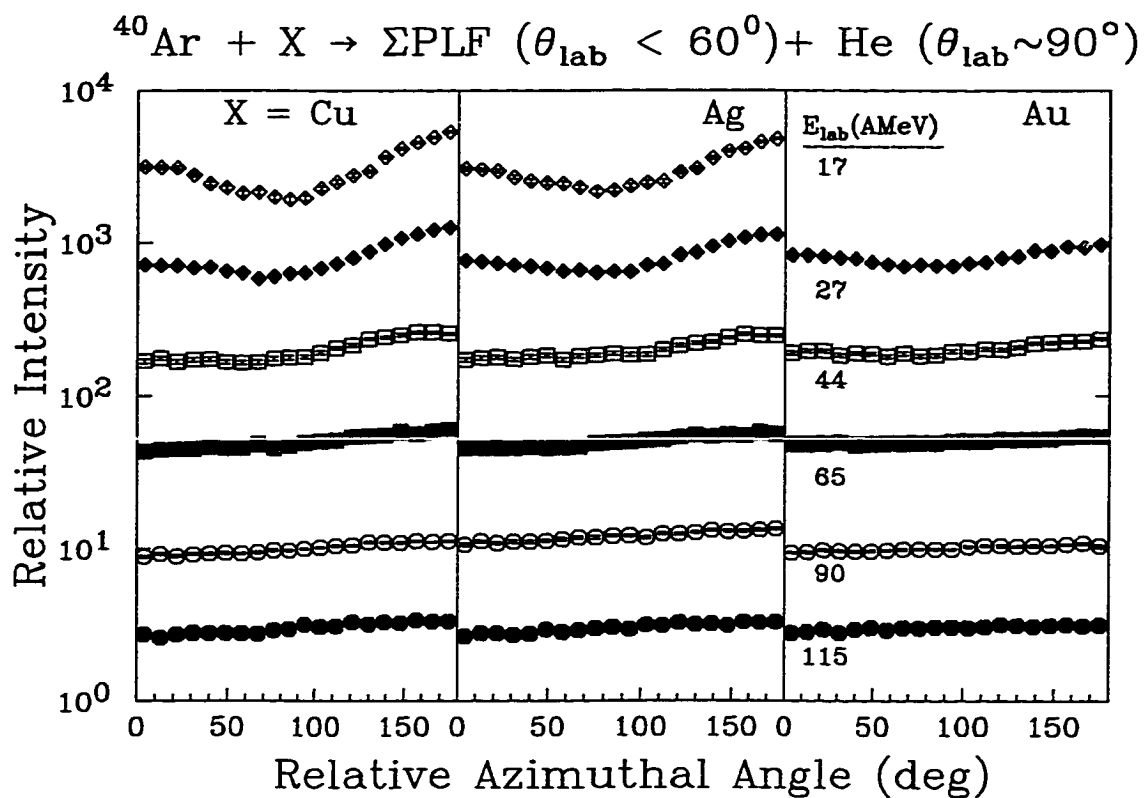
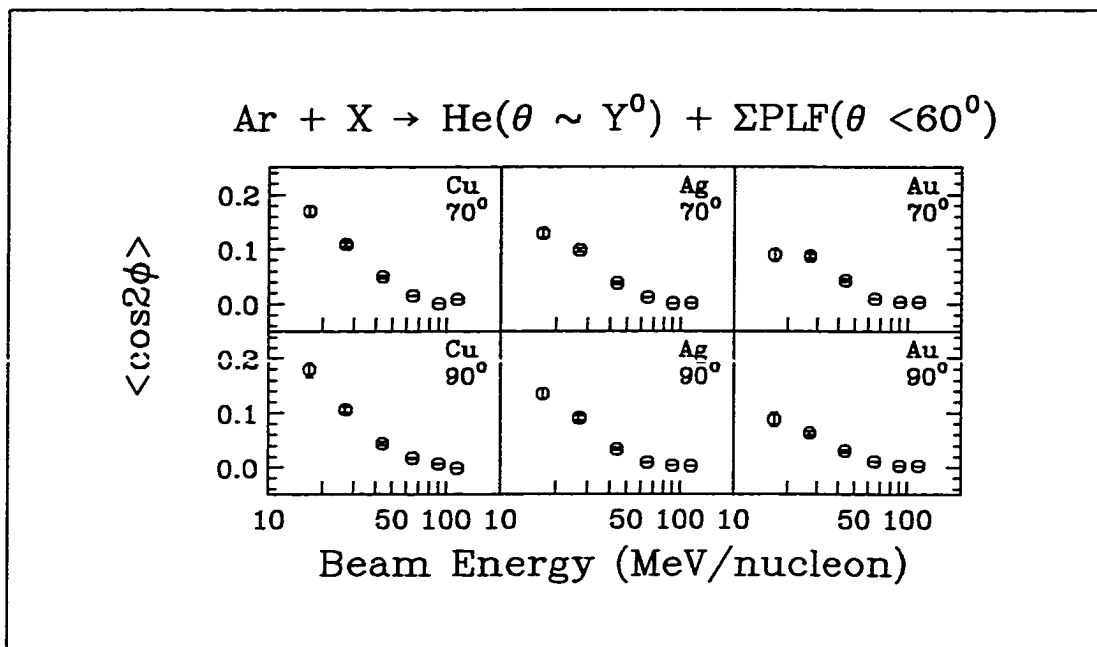Figure C.5: Azimuthal correlation functions of He at $\theta_{lab} \sim 90^0$ for Ar+Cu, Ag and Au.

^{40}Ar + X → He $(\theta_{lab}\sim90°)$ + IMF $(\theta_{lab}\sim90°)$

Figure C.6: Azimuthal correlation functions of IMF at $\theta_{lab} \sim 90°$ for Ar+Cu, Ag and Au.

Figure C.7: Average $< cos2\theta >$ of He at $\theta_{lab} \sim 70^0$ and $\theta_{lab} \sim 90^0$ for Ar+Cu, Ag and Au.

Appendix D
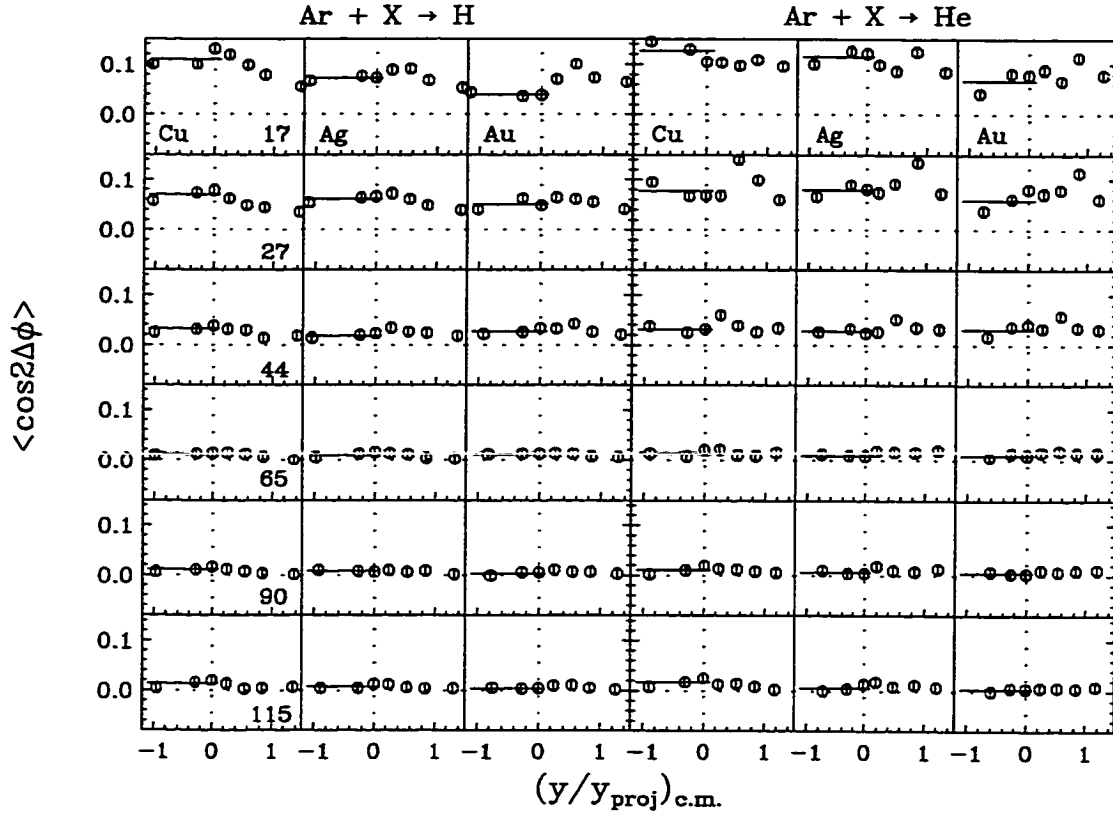
Data for $< cos2\phi >$ for Various Ejectiles Selected by Rapidity

Figure D.1: Average $< cos2\phi >$ of H and He with different rapidity cuts for Ar+Cu, Ag and Au.

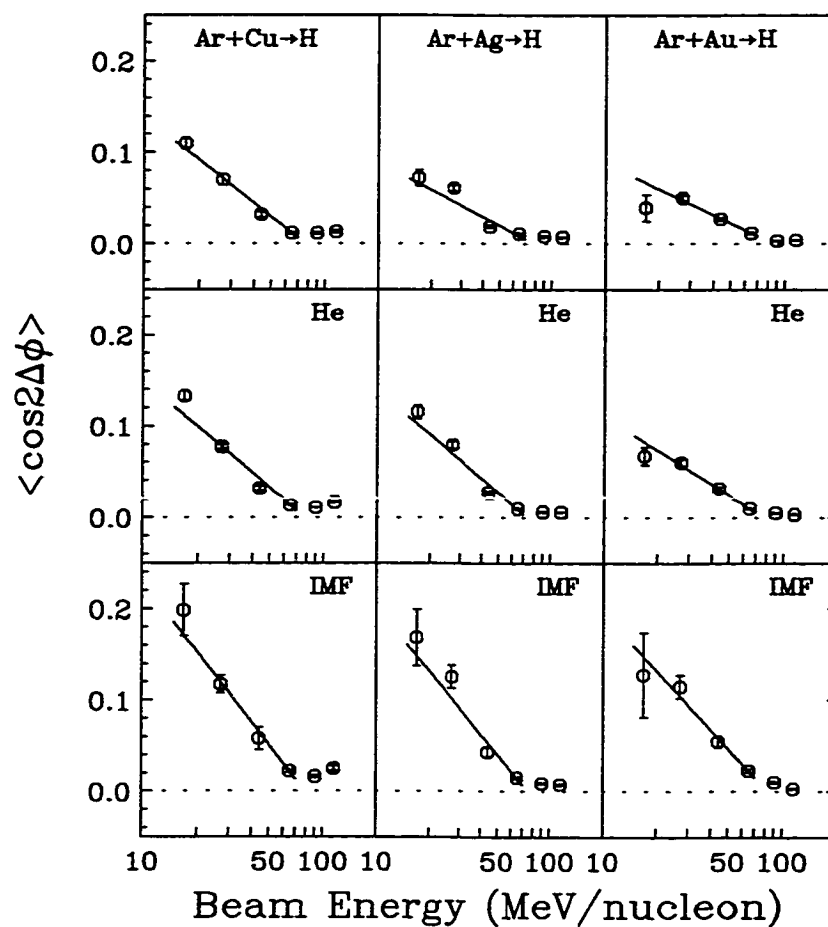Figure D.2: Evolution of average $< cos2\phi >$ with respect to incident energy for Ar+Cu, Ag and Au using rapidity cuts.